

LARGE-EDDY SIMULATION OF COMBUSTION INDUCED VORTEX BREAKDOWN IN AN
UNCONFINED TURBULENT VORTEX USING A PRESUMED-PDF COMBUSTION
MODEL

Dissertation

zur

Erlangung des akademischen Grades

Doktor-Ingenieur (Dr.-Ing.)

der Fakultät für Maschinenbau und

Schiffstechnik

der Universität Rostock

vorgelegt von Dipl.-Ing. Hannes Kröger
 geboren am 28. August 1979
 in Rostock
aus Rostock

Gutachter: Prof. Dr.-Ing. habil. E. Hassel
 Prof. Dr.-Ing. habil. N. Kornev
 Prof. Dr. rer. nat. M. Pfitzner

Gutachter:

Prof. Dr.-Ing. habil. Egon Hassel Universität Rostock
Fakultät für Maschinenbau und Schiffstechnik
Lehrstuhl für Technische Thermodynamik

Prof. Dr.-Ing. habil. Nikolai Kornev Universität Rostock
Fakultät für Maschinenbau und Schiffstechnik
Lehrstuhl für Technische Thermodynamik

Prof. Dr. rer. nat. Michael Pfitzner Universität der Bundeswehr München
Fakultät für Luft- und Raumfahrttechnik
Institut für Aerodynamik

Datum der Disputation:

27. Juli 2010

Acknowledgements

I want to acknowledge the help of a number of people, who supported me in doing the work for this thesis. My special thanks go to

- Prof. Dr. Egon Hassel for giving me the opportunity to write this thesis under his supervision,
- Prof. Dr. Nikolai Kornev for the many critical and helping comments and tips at many occasions,
- Prof. Dr. Michael Pfitzner for reviewing my thesis.
- Dr. Detlef Wendig for providing the experimental data for the CIVB research project,
- Dr. Steffen Jahnke, who collected and shared a huge knowledge on Large-Eddy Simulation and CFD in general during his time at the LTT Rostock,
- Matthias Walter who always did a great job in managing the computers and clusters in our department,
- Johann Turnow for the many useful discussions and
- Danilo Webersinke for the accurate and critical review of every presented idea.

I am especially grateful to my wife Nadine and my son Felix who always remembered me that there is much more in life than CFD and combustion.

Rostock, January 2010

Hannes Kröger

Contents

Acknowledgements	3
List of Figures	7
List of Tables	10
Nomenclature	11
1. Introduction	14
1.1. Motivation	14
1.2. Vortex Breakdown in Isothermal Flow	16
1.3. Combustion Induced Vortex Breakdown	18
1.3.1. Survey of Previous Works	18
1.3.2. State of the Art	22
1.4. Objectives and Tasks	24
1.5. Outline of this Work	25
I. Theoretical Preliminaries	26
2. Fluid Dynamics	27
2.1. Conservation Laws	27
2.1.1. Mass	27
2.1.2. Momentum	29
2.1.3. Energy	30
2.1.4. Equation of State	32
3. Chemical Reactions and Combustion	34
3.1. Flames	35

Contents

3.1.1. Premixed Flame	35
3.1.2. Non-Premixed Flames	40
3.1.3. Partially Premixed Flames	42
3.2. Simplifications of Chemical Mechanisms	43
3.2.1. One-Step Chemistry	43
3.2.2. Intrinsic Low-Dimensional Manifolds	44
3.2.3. Computation of ILDM's	45
3.2.4. Reaction-Diffusion Manifolds (REDIM)	48
3.2.5. Flamelet Generated Manifolds (FGM)	49
4. Numerical Methods for Computational Fluid Dynamics	51
4.1. Finite Volume Method	51
4.1.1. Spatial Discretization	51
4.1.2. Temporal Discretization	52
4.1.3. Treatment of the Pressure	53
4.2. Turbulent Flows	53
4.3. Large-Eddy Simulation	55
4.3.1. Spatial Filtering	55
4.3.2. LES Equations	56
4.3.3. Numerical Requirements for the Large-Eddy Simulation	57
4.3.4. Closure Models for the Large-Eddy Simulation	58
4.3.5. Combustion Models for LES	59
II. Applications	68
5. Implementation of the Presumed PDF Model into the CFD Code	69
5.1. Density Weighting of the PDF	72
5.2. Chemistry and Lookup Table Storage and Retrieval	72
5.3. Chemistry Table Generation	73
5.4. PDF Integration	74
5.5. Methods for Determination of the Scalar Variance	76
5.5.1. Transport Equation	77
5.5.2. Scale Similarity Assumption	78
5.5.3. Dynamic Procedure	79
5.5.4. Calculation from Flame Surface Density	80

5.6. Summary of Implemented Equations 81

III. Results 84

6. Assessment of the Model Implementation 85

6.1. Premixed Laminar Flat Flame 87

6.2. Turbulent Combustion Bomb 90

6.3. ORACLES 96

6.4. Backward Facing Step 102

6.5. Bunsen Flame 107

6.6. Summary of the Model Assessment 113

7. Combustion Induced Vortex Breakdown in Free Vortices 114

7.1. Object of Investigation 114

7.2. Experimental Observations 116

7.2.1. Isothermal Flow Characteristics 117

7.2.2. Flame Propagation 122

7.3. LES Simulation of Flashback Event 124

7.3.1. Grid and Boundary Conditions 125

7.3.2. Simulation of Isothermal Flow 127

7.3.3. Prediction of Flashback Limits 130

7.3.4. Detailed Analysis of Vortex Dynamics During the Flashback Event 132

8. Summary and Conclusion 143

Bibliography 144

List of Figures

1.1. Examples for vortex breakdown	16
1.2. Sketch of vortex/flame interaction during CIVB	22
3.1. Premixed flame	36
3.2. Unstretched laminar flame speeds of different fuel/air mixtures	36
3.3. Structure of a laminar premixed flame	37
3.4. Examples for partially-premixed flame configurations	43
3.5. Reactions paths of a homogeneous methane-air system	44
4.1. Possible shapes of the beta function for different values of the parameters p and q	63
5.1. Sketch of the algorithm structure of the presumed-PDF solver	71
6.1. Location of all simulated cases in the combustion diagram	86
6.2. Sketch of a premixed laminar flat flame [85]	87
6.3. Laminar premixed flame: profiles of temperature, density and velocity across flame front	88
6.4. Laminar premixed flame: Lewis number across flame front	89
6.5. Sketch of a turbulent combustion bomb	90
6.6. Turbulent combustion bomb: snapshot of flame front	92
6.7. Development of flame kernel diameter in simulations of turbulent combustion bomb with Presumed-PDF model. The six experimental runs had the same initial conditions and give an impression of the experimental repeatability.	93
6.8. Development of flame kernel diameter in simulations of turbulent combustion bomb with Presumed-PDF model at high turbulence intensity	93

List of Figures

6.9. Development of flame kernel diameter in simulations of turbulent combustion bomb with Weller $b-\Xi$ model. The six experimental runs had the same initial conditions and give an impression of the experimental repeatability.	94
6.10. Development of flame kernel diameter in simulations of turbulent combustion bomb with Artificially Thickened Flame model. The six experimental runs had the same initial conditions and give an impression of the experimental repeatability.	95
6.11. Sketch of the upper symmetry half of the ORACLES test rig	97
6.12. Mean velocity profile at inlet in ORACLES rig	98
6.13. Instantaneous flame surface in simulation of ORACLES rig	99
6.14. Position of evaluated profiles in simulation of ORACLES rig	99
6.15. Mean velocity profiles in ORACLES rig	100
6.16. Profiles of axial velocity fluctuation in ORACLES rig	101
6.17. Sketch of the backward-facing step test rig	102
6.18. Instantaneous flame surface in simulation of backward facing step	103
6.19. Comparison of instantaneous flame surface in simulation of backward facing step with Schlieren photograph	104
6.20. Normalized mean velocity profiles in backward-facing step test case . . .	105
6.21. Normalized mean temperature profiles in backward-facing step test case .	106
6.22. Sketch of the Bunsen flame setup	108
6.23. Dependency of density from normalized temperature c for a stoichiometric mixture of CH_4 /air at $T_0 = 300K$	109
6.24. Time averaged fields of axial velocity. The lower half shows the isothermal case, the upper half the reacting flow.	110
6.25. Mean velocity profiles in Bunsen flame test case	111
6.26. Mean velocity profiles in Bunsen flame test case	112
6.27. Instantaneous flame surface. The thick black line shows the time averaged flame contour from [16]	112
7.1. Sketch of the movable block swirl generator principle	115
7.2. Experimental setup	116
7.3. Autocorrelation functions in isothermal velocity field (CIVB)	121
7.4. Simultaneous PIV/LIF snapshots of propagating flame during CIVB . . .	123
7.5. Grid for simulation of isothermal and reacting flows (CIVB)	125

List of Figures

7.6. Ratio of LES filter width to laminar flame thickness vs. distance from nozzle along centerline in CIVB setup	126
7.7. Mean inflow velocity profiles for case $S = 0.39$, $\dot{V} = 12m^3/h$	127
7.8. Comparison of LES with modified boundary conditions for $S = 0.49$. Left half shows LES ($\dot{V} = 20m^3/h$), right half shows PIV.	128
7.9. Local air equivalence ratio in CIVB setup	130
7.10. Limiting curve for flashback occurrence in experimental apparatus for ignition heights $12cm$ and $18cm$ at swirl number $S = 0.39$. The air equivalence ratio is at the nozzle exit.	131
7.11. Plots of flame tip to nozzle distance vs. time	133
7.12. Axial velocity field averaged in flame tip fixed coordinate system	136
7.13. Spiraling of vorticity lines at the flame front	137
7.14. Probability density functions of the circumferential components of the three different vorticity production terms.	140
7.15. Accelerations induced along the vortex centerline by the three different vorticity production terms	141
7.16. Averaged accelerations induced along the vortex centerline by the three different vorticity production terms (only mean)	142

List of Tables

6.1. Estimated time and length scales for the different simulation cases	85
6.2. Performed simulations of the turbulent combustion bomb: Overview of simulations	91
6.3. Performed simulations of the turbulent combustion bomb: Common parameters	91
7.1. Parameters of experimental setup for CIVB	116
7.2. Contour plots of axial velocity in isothermal flow (CIVB experiment) . .	118
7.3. Contour plots of RMS of axial velocity in isothermal flow (CIVB experiment)	119
7.4. Profiles of axial velocity in isothermal flow (CIVB experiment)	120
7.5. Levels of velocity mean and RMS in CIVB setup	124
7.6. Estimated turbulent flame speed in CIVB setup	124
7.7. Contour plots of axial velocity in isothermal flow PIV vs. LES (CIVB) .	129
7.8. Overview on performed simulations	132
7.9. Flame propagation speeds during CIVB	134

Nomenclature

α	Thermal diffusivity	$kg/(m\ s)$
δ_R	Ratio of reaction zone thickness to laminar flame thickness, p. 39	
$(\dot{\cdot})$	Time derivative, equal to $\partial(\dot{\cdot})/\partial t$	
$\dot{\omega}_i$	Net production of species i , see Eq. (2.5), p. 28	$kg\ m^{-3}\ s^{-1}$
\dot{V}	Volume flux	m^3/s
λ	Thermal conductivity	$W/(mK)$
\mathbf{S}	Strain rate tensor, see Eq. (2.12), p. 30	s^{-1}
\mathbf{T}	Stress tensor, see Eq. (2.10), p. 30	N/m^2
μ	Viscosity (dynamic viscosity), see Eq. (2.11), p. 30	$Pa\ s$
∇	Nabla operator, $\nabla = (\frac{\partial}{\partial x}\ \frac{\partial}{\partial y}\ \frac{\partial}{\partial z})^T$	
ν_{ij}^+	Stoichiometric coefficient of reactant i in reaction j , see Eq. (3.1), p. 34	
ν_{ij}^-	Stoichiometric coefficient of product i in reaction j , see Eq. (3.1), p. 34	
\mathfrak{R}	Molar (universal) gas constant, see Eq. (2.23), p. 32	$J \cdot K^{-1}mol^{-1}$
ρ	Density, see Eq. (2.1), p. 28	kg/m^3
σ	Density ratio $\sigma = \rho_u/\rho_b$, p. 37	
τ_c	Characteristic time scale of premixed combustion, p. 38	s

List of Tables

τ_t	Characteristic time scale of Kolmogorov eddies, p. 38	s
τ_t	Characteristic time scale of turbulence, p. 38	s
$\vec{\omega}$	Vorticity	s^{-1}
\vec{u}	Velocity	m/s
\vec{V}_i	Diffusion velocity of species i , see Eq. (2.6), p. 29	m/s
A	Area	m^2
B	Preexponential factor, see Eq. (3.2), p. 34	
b	Temperature exponent, see Eq. (3.2), p. 34	
c_p	Heat capacity at constant pressure, p. 32	$J \cdot K^{-1}kg^{-1}$
c_v	Heat capacity at constant volume, p. 32	$J \cdot K^{-1}kg^{-1}$
D_i	Diffusion coefficient of species i into mixture, see Eq. (2.6), p. 29	m^2/s
Da	Damköhler number, p. 38	
E	Internal energy, see Eq. (2.13), p. 30	J
e	Specific internal energy, see Eq. (2.14), p. 31	J/kg
E_a	Activation energy, see Eq. (3.2), p. 34	$J/kmol$
k_f	Rate coefficient of chemical reaction, see Eq. (3.1), p. 34	
Ka	Karlovitz number, p. 38	
L_t	Integral length scale of turbulence	m
l_δ	Thickness of the reaction zone in a laminar flame, p. 39	m
M	Molecular weight, see Eq. (2.26), p. 33	$kg/kmol$

List of Tables

m	Mass	kg
n_e	Number of elements in a chemical system	
n_r	Number of reactions in a chemical system, see Eq. (3.3), p. 35	
n_s	Number of species in a mixture, see Eq. (2.9), p. 29	
Q	Heat, see Eq. (2.13), p. 30	J
q	Specific heat, see Eq. (2.14), p. 31	J/kg
Re_t	Turbulent Reynolds number, p. 39	
s_L^0, s_L	Laminar flame speed, p. 37	m/s
s_T	Turbulent flame speed	m/s
T	Temperature	K
t	Time	s
u'	Turbulent velocity fluctuation	m/s
V	Volume	m^3
W	Work, see Eq. (2.13), p. 30	J
w	Specific work, see Eq. (2.14), p. 31	J/kg
Y_i	Mass fraction of species i , see Eq. (2.4), p. 28	kg/kg

1. Introduction

1.1. Motivation

The main goal of this work is a numerical simulation of the Combustion Induced Vortex Breakdown (CIVB). This term labels the triggering or altering of vortex breakdown by the presence of a flame. This was probably first noted by McCormack [59] during his research on flame propagation in vortex rings. Over the decades, other scientists have done further research on this topic and investigated flame propagation in different vortex configurations theoretically and experimentally. These works are reviewed in section 1.3.1.

CIVB is also the mechanism behind a combustion instability that was discovered during the experimental investigation of flame flashbacks in premixed gas turbine combustion chambers at TU Munich [26, 25, 50]. It occurs in premixed burners without central bluff body that utilize vortex breakdown forced by a sudden expansion for an aerodynamic stabilization of the flame. It is different from other well-known types of flame flashback as flashback along the wall when velocity gradient are too low, upstream flame propagation through the bulk flow when the bulk velocity falls below the turbulent flame speed or acoustic instabilities. Instead, CIVB occurs, if the thermal power is increased beyond some critical value. Then, a small bubble of recirculating flow is induced ahead of the flame tip at the axis which can propagate further upstream. This recirculating bubble is due to vortex breakdown that is locally induced by the flame.

Since low-emission gas turbines employ premixed combustion and occurrence of CIVB especially prevents stable operation of these type of burners, there is growing interest to understand the mechanisms of CIVB. To bundle the research and enable easy knowledge exchange, a joint research project has been initiated by TU Munich, University of the

1. Introduction

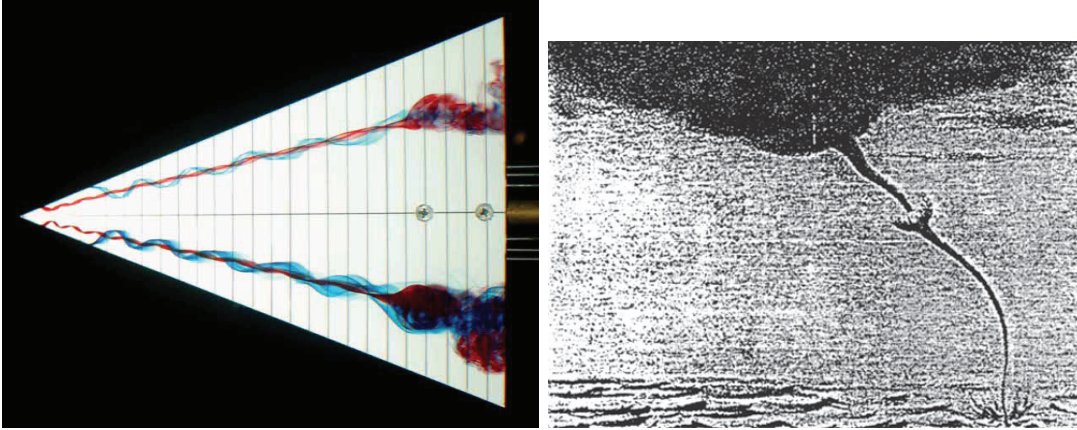
German Armed Forces in Munich, TH Karlsruhe, TU Darmstadt and Rostock University. The work describes a large part of the research at Rostock University.

The original studies on CIVB in gas turbine burners were limited to only one special vortex configuration but CIVB may occur in other forms as well. Flame flashback of this type is also found in gas turbine combustion chambers with central bodies [62] and along Precessing Vortex Cores (PVC) around bluff bodies [61]. This work deals with CIVB in unconfined vortices.

The investigation of CIVB is difficult due to the fact that it is an unsteady phenomenon which happens within milliseconds. To gain a comprehensive picture of the flow pattern, knowledge of the velocity field and the chemical state, i.e. species concentrations or temperature, is required. Measuring these quantities is very demanding for the experimental instrumentation because a high time resolution is required. In the context of this work, only chemiluminescence videos with a reasonably high time resolution were available. Simultaneous PIV and OH-LIF measurements were done as well, but not time resolved, i.e. only for a single time instance per CIVB event. The chemiluminescence videos only give an integral picture of the chemical state whereas no time-resolved information on the velocity field was available. Thus, much emphasis was put on the numerical simulation. All required informations for an analysis could be retrieved from it, given that the relevant flow patterns are well reproduced.

For the numerical simulations in the current work, the large eddy simulation (LES) technique was applied, mostly because it is expected to be generally more accurate and requires less modeling effort than unsteady Reynolds-Averaged Navier-Stokes (URANS) based techniques, which usually rely on empiricism to a greater extend.

As was already mentioned above, there is a relation of the accelerated flame propagation to the vortex breakdown phenomenon. This idea shall be presented in the following sections in more detail. At first, vortex breakdown in the isothermal flow will be introduced in the next section. Later on, the connection between vortex breakdown and flame acceleration will be depicted in section 1.3.



(a) Vortex breakdown over a delta wing [54] (b) Waterspout in the Mediterranean Sea revealing a structure akin to vortex breakdown (Drawing by Michaud, 18th century) [1]

Figure 1.1.: Examples for vortex breakdown

1.2. Vortex Breakdown in Isothermal Flow

Although vortex breakdown is well known for a long time, there is still no general theory for its description. Vortex breakdown occurs e.g. in leading edge vortices of delta wings when a certain threshold of the angle of attack is exceeded, it can be observed in nature in tornadoes or water spouts and it is technically utilized e.g. in gas turbines, as described above.

Vortex breakdown may be described as “an abrupt change in the character of a columnar vortex at some axial station. It is usually observed as a sudden widening of the vortex core together with a deceleration of the axial flow and is often followed by a region or regions of recirculation.” [56]. Generally, vortex breakdown appears if the swirl exceeds some critical intensity which is not universal rather than depends on the flow type and on the form of the vortex core.

In high Reynolds number flow $Re > 3500$, two different shapes of vortex breakdown are distinguished: the “bubble” type occurs at high swirl intensities while the “spiral” type can be observed at lower swirl intensities. The bubble type has got its name from the recirculation zone downstream of the stagnation point. Inside this recirculation zone, strong negative axial velocities can be found. The external flow passes the recirculation zone like a solid body, thus it appears like a bubble inside the vortex. During the spiral type vortex breakdown, the axial flow is decelerated as well but the vortex core

1. Introduction

winds up around the axis. Thus, the spiral type vortex breakdown possesses no axial symmetry whereas the bubble type vortex breakdown is axisymmetric. Depending on the particular flow, transitions from one type into the other may be observed.

Brown and Lopez [7] have developed an intuitive explanation for the axisymmetric vortex breakdown by utilizing the vorticity to describe the flow. The evolution of vorticity is described by a transport equation which reads in the inviscid form

$$\frac{\partial \vec{\omega}}{\partial t} + (\vec{u} \cdot \nabla) \vec{\omega} = \underbrace{-\vec{\omega} (\nabla \cdot \vec{u})}_1 + \underbrace{\frac{1}{\rho^2} \nabla \rho \times \nabla p}_2 + \underbrace{(\vec{\omega} \cdot \nabla) \vec{u}}_3 \quad (1.1)$$

The three terms on the right hand side are source terms and describe vorticity production by different physical mechanisms. The first term represents vorticity production by density changes, term 2 causes the baroclinic production, i.e. creation of vorticity due to non-parallel isobars and isochors. Finally, term 3 represents vortex stretching. If density is constant, only this vorticity production mechanism remains and Eq. (1.1) reduces to the Helmholtz equation:

$$\frac{\partial \vec{\omega}}{\partial t} + (\vec{u} \cdot \nabla) \vec{\omega} = (\vec{\omega} \cdot \nabla) \vec{u} \quad (1.2)$$

After replacement of $\vec{\omega}$ by \vec{s} , Eq. (1.2) is formally identical to the transport equation of a material line element \vec{s} which connects two material fluid particles. This illustrates vortex stretching: if a material line is stretched by the velocity field, vorticity vectors will be elongated as well, i.e. the rotational speed of the fluid will increase. Another effect of importance occurs in the case of a vortex with an inner axial flow where the stream lines diverge along the vortex axis. Because angular momentum is conserved, a fluid particle that is transported radially outward loses circumferential speed. Thus a material line is deformed into a spiral form. The same is true for the vorticity lines. The vorticity vectors are relocated and get a negative circumferential component whenever the streamlines spread radially.

The latter effect is of importance in conjunction with vortex breakdown, as was pointed out by Brown and Lopez [7]. According to Biot-Savart's law, vorticity induces a velocity in the whole domain. In the case of an axisymmetric flow, the induced axial velocity at

1. Introduction

$r = 0$ is related to the circumferential vorticity ω_φ :

$$u_{ind,z} = \frac{1}{2} \int_{-\infty}^{\infty} \int_0^{\infty} \frac{r^2 \omega_\varphi(r, z)}{[r^2 + (z - z')^2]^{\frac{3}{2}}} dr dz \quad (1.3)$$

From (1.3) it becomes clear that negative circumferential vorticity causes negative axial velocity at the vortex axis, i.e. the axial flow is decelerated. If the flow on the axis is decelerated, fluid is displaced radially outward by continuity, which in turn causes creation negative circumferential vorticity. Thus, a feedback loop is created which leads to the breakdown of the axial flow. According to Brown and Lopez [7], the vortex widening is initiated by diffusion effects. They also give a criterion for the occurrence of negative circumferential vorticity: At some initial axial station z_0 , the helix angles of velocity u_φ/u_z have to be larger than these of vorticity $u_\varphi/u_z > \omega_\varphi/\omega_z$.

1.3. Combustion Induced Vortex Breakdown

In a number of works, e.g [4, 17, 82, 25, 50], it was found that vortex breakdown can be altered or triggered by the presence of a flame. The term Combustion Induced Vortex Breakdown (CIVB) was coined for this phenomenon. Vortex breakdown severely changes the velocity field in a vortical flow. Since it is usually accompanied by the creation of stagnation point at the vortex core, the decelerated flow around the stagnation point could allow the flame to propagate upstream or the flame could be even convected upstream by the reversed flow in the recirculation zone. The latter is suggested e.g. by Konle et al. [48]. In their experimental study of CIVB in a model gas turbine burner, they usually find the flame downstream of the stagnation point when CIVB occurs.

As mentioned above, a number of authors have published investigations regarding CIVB. At this stage, a survey on the available literature shall be given first. The resulting state of the art will be summarized in the next subsection 1.3.2.

1.3.1. Survey of Previous Works

In this section, an overview of earlier experimental, numerical and theoretical studies of flame acceleration in vortex tubes is given.

Experimental Investigations

A number of the following experiments have been performed on generic setups to investigate the phenomenon of enhancement of flame propagation speed in vortices:

- Flame propagation in a combustible vortex ring, e.g. by McCormack [59], Ishizuka [43]
- Flame propagation in a rotating, confined tube, e.g. by Sakai and Ishizuka [77]
- Flame propagation in an unsteady, straight vortex, e.g. by Hasegawa [38]

All experiments reveal some form of dependence of the flame propagation velocity v_f on the maximum circumferential velocity v_θ and the ratio of unburned gas to burned gas densities σ :

$$v_f = f(v_\theta, \sigma = \frac{\rho_u}{\rho_b})$$

Most of experimental works indicates that the flame speed is linear dependent on the maximum circumferential velocity:

$$v_f \sim C v_\theta$$

Ishizuka et al. [43] found a proportionality factor C around unity $C \approx 1$ in their investigation of a stoichiometric methane/air flame.

Sakai and Ishizuka [77] did not observe a steady flame velocity in their investigation of flame propagation in a rotating tube. Anyway, they obtained a linear relationship between the flame speed and circumferential velocity when they measured the flame speed at some certain positions in the tube at different rotational speeds. Additionally, there is an influence of the Lewis number and the equivalence ratio on the flame speed found in [77]. For Lewis numbers $Le > 1$, the flame is shortened and burns weaker, for $Le < 1$, the flame gets longer and the burning is intensified.

Hasegawa et al. [39] subdivided the flame evolution into two stages. Within the first short transition stage the flame is accelerated until it gets longer than twice its diameter. In the second stage the flame speed remains approximately constant being proportional to the maximum circumferential velocity.

Theoretical Explanations of Accelerated Flame Propagation

Back pressure raising Chomiak [17] proposed the vortex breakdown mechanism for acceleration of the flame. Starting from Bernoulli's theorem he writes the following integral relation on the flame surface A :

$$\int_{(A)} (p - p_0) dA = \int_{(A)} \rho_b v_f^2 dA \quad (1.4)$$

where $(p - p_0)$ denotes a pressure difference across the flame surface. By inserting the pressure distribution of a Rankine vortex, he arrives at the following expression for the flame velocity in a vortex:

$$v_f = v_\theta \sqrt{\frac{\rho_u}{\rho_b}} \quad (1.5)$$

Baroclinic Push If density and pressure gradients are not aligned, they create vorticity. This is the so called baroclinic vorticity production mechanism. This mechanism is represented by the term 2 in the inviscid vorticity transport equation:

$$\frac{\partial \vec{\omega}}{\partial t} + (\vec{u} \cdot \nabla) \vec{\omega} = \underbrace{-\vec{\omega} (\nabla \cdot \vec{u})}_1 + \underbrace{\frac{1}{\rho^2} \nabla \rho \times \nabla p}_2 + \underbrace{(\vec{\omega} \cdot \nabla) \vec{u}}_3 \quad (1.6)$$

The model of Ashurst [4] utilizing this effect may be outlined as follows: The pressure gradient in radial direction of the vortex and the density gradient across the flame front normal to the vortex axis produce a circumferentially aligned vorticity ω_θ . In its turn, this vorticity induces a velocity, that is directed from the burned gas across the flame front towards the unburned gas and drives the flame upstream.

Ashursts calculation of this velocity starts with the vorticity transport equation with all terms neglected excepting the baroclinic production:

$$\frac{d\vec{\omega}}{dt} = \frac{1}{\rho^2} \nabla \rho \times \nabla p \quad (1.7)$$

He assumes the following distribution of the circumferential velocity:

$$\frac{v_\theta}{r} = \frac{\Gamma}{2\pi r^2} [1 - \exp(-r^2/r_M^2)] \quad (1.8)$$

1. Introduction

Here Γ is the vortex circulation and r_M is a characteristic radius of the vortex core.

The pressure gradient corresponding to the velocity (1.8) is

$$\frac{1}{\rho} \nabla p = \frac{v_\theta^2}{r} \quad (1.9)$$

While the density gradient may be approximated as

$$\frac{1}{\rho} \nabla \rho = \frac{\rho_u - \rho_b}{\delta \sqrt{\rho_u \rho_b}} = \frac{\tau}{\delta \sqrt{\tau + 1}} \quad (1.10)$$

where $\tau = \rho_u / \rho_b - 1$ is the heat release parameter and δ is the flame thickness. Substituting (1.9) and (1.10) into equation (1.7) and integrating over the vortex cross section from the axis to $3r_M$ gives:

$$\frac{d\omega_\theta}{dt} \sim \frac{4.5\tau}{\delta \sqrt{\tau + 1}} r_M v_M^2 \quad (1.11)$$

where v_M is the circumferential velocity at $r = r_M$. By expressing the temporal derivation through the spatial one and introducing the length of burned gas X_F , he arrives at the following dependency:

$$v_f \sim \frac{\tau}{\delta \sqrt{\tau + 1}} r_M v_M^2 \frac{1}{s_L(\tau + 1)} \sqrt{X_F / r_M} \quad (1.12)$$

Vortex spiraling mechanism Umemura and Tomita [82] also investigated the creation of the circumferential vorticity ω_θ due to the presence of the flame. They create a simple model of the vortex with the flame in its core. The velocity profile of the Rankine vortex is used. The conservation of angular momentum along streamlines

$$rv_\theta = \text{const}$$

and Bernoulli's theorem lead to a solution for the evolution of circumferential vorticity:

$$\omega_\theta = \begin{cases} \frac{1}{\rho_u} \left(\frac{2\Omega}{v_f} \right)^2 \frac{1}{r} \left[\frac{1}{2} \rho_u v_f r^2 - \psi \right] & : \text{ inside the core} \\ 0 & : \text{ outside the core} \end{cases} \quad (1.13)$$

where Ω is the angular velocity of the vortex and ψ is the stream tube function. Because the streamlines diverge starting from a certain point in front of the flame, the r.h.s. of equation (1.13) and therefore the circumferential vorticity are always positive within the

1. Introduction

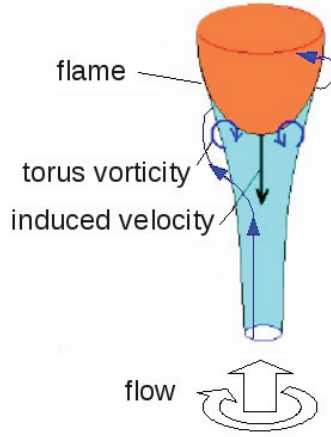


Figure 1.2.: Sketch of vortex/flame interaction during CIVB: The vorticity line (blue) is spiraled, i.e. it gets a circumferential component (torus vorticity). This torus vorticity induces a velocity on the axis (black arrow) that is directed against the initial flow. The deceleration of the flow on the axis may in turn cause a more intense spiraling of the vorticity and thus cause a feedback.

divergence area. The vorticity induces an axial velocity which drives the flame front along the vortex.

An expression for the flame propagation velocity is obtained from integrating the conservation of momentum and angular momentum along two paths and equating the results:

$$v_f = \sqrt{\frac{2\sigma + 1}{\sigma} (\Omega r_M)^2 + \sigma s_L^2} \quad (1.14)$$

where r_M is again a characteristic radius of the vortex, i.e. the core radius of the Rankine vortex and $\sigma = \rho_u/\rho_b$ is the density ratio.

1.3.2. State of the Art

While isothermal vortex breakdown may be explained on behalf of the vorticity transport equation (1.1), it is plausible, that the mechanism of vortex breakdown in the reacting flow is similar and the vorticity equation still plays a role in its explanation. In the isothermal case, only term 3 is present in (1.1) because density is constant and therefore no density gradients exist and the velocity divergence is zero. In that case, the circumferential component of vorticity can only be created by radial expansion of the stream surfaces. In contrast, combustion is associated with strong density changes. While still

1. Introduction

circumferential vorticity is considered to be the cause for the flow deceleration (see figure 1.2), the baroclinic and dilution term might play a role in its creation as well.

Different views on the interaction of flame and vortex breakdown can be found in literature. Ashurst [4] creates a theoretical model which relies solely on the baroclinic effect to create the circumferential vorticity. Also, Kiesewetter [47] finds the baroclinic production of vorticity dominating in his numerical simulations of Combustion Induced Vortex Breakdown in a gas turbine combustion chamber. Domingo and Vervisch [20] have performed a DNS of a flame interacting with a vortex. They find an enhanced flame propagation speed and they hold the baroclinic mechanism responsible for the vorticity creation in their case as well.

Opposedly, Umemura et al. [82] only considered the radial expansion of the vortex tube, which occurs because the flame acts as a volumetric source, in their model of flame propagation. In their numerical simulations, they find the pressure gradient across the flame surface too low for creation of appreciable amounts of circumferential vorticity. They point out, that the baroclinic effect is most intense if the the flame front is aligned perpendicular to the vortex axis. During the propagation, usually a parabola-like flame shape is observed. So, Umemura et al. conclude, that this effect can only be of relevance in the initial unsteady stage of flame propagation. When the flame is fully developed, the strain effect may dominate.

The review of the available literature reveals some gaps in the current understanding of CIVB: most of the investigations have been done on laminar flow configurations or those that were near transition. It is not fully clear, if the conceptions of flame induced vortex breakdown, that were sketched above, also hold in a fully turbulent vortex and which additional effects due to turbulence have to be considered.

Also, when unconfined vortices were studied, they had been generated by some unsteady process which resulted in vortex rings or linear vortex pairs which were freely traveling through space. The unsteadiness made it difficult to characterize the initial conditions of the flame propagation, i.e. the velocity field of the vortex.

Up to now, no investigations of the effect of an inner axial velocity along the vortex axis on the combustion/vortex interaction in an unconfined vortex has been performed. An axial flow was only present during the study of CIVB in gas turbine combustion chamber [50, 25], but this was a confined flow.

1.4. Objectives and Tasks

The main objective of this work is to investigate the enhancement of flame propagation speed in an unconfined vortex using numerical methods.

The vortex shall be unconfined, steady, fully turbulent and with a strong inner axial flow.

The current work primarily aims

- to determine, whether the Large-Eddy Simulation is sufficiently accurate to model CIVB. Being able to use numerical simulations to predict CIVB is especially desirable for designers of combustion devices which may potentially suffer from the formerly described combustion instability. It has been shown in previous works [47], that it is in principle possible to model CIVB using URANS methods. However, applying RANS methods includes a considerable amount of empiricism, especially in the combustion field. LES methods offer an increased predictive capability, because in the LES context, it is often possible to formulate submodels in a more universal way with less empirical coefficients that need to be tuned.
- to check whether vortex breakdown plays a role during flame acceleration in the chosen setup. This information should be given primarily by the experimental investigations of the selected setup, but the experiments can only show a certain fragment of the flow informations. In contrast, once they are validated, the simulations can present the full set of flow information which enable a detailed inspection of the physical processes.
- to detect the physical mechanisms which bring the flame to cause vortex breakdown. Is the expansion of the exhaust gases in the vortex core the major reason or is it the baroclinic torque? How does the turbulence affect the physical processes? The questions are of rather fundamental nature and if answers were found, they might be useful in future theoretical models of CIVB. As already mentioned, there already exist some theoretical approaches to CIVB but there is yet no clear consensus on which mechanism is dominating and has to be included in the models.

To achieve the aims, the following main tasks appeared relevant:

1. Introduction

- Selection of an adequate combustion model and, if necessary, implementation into the preferred CFD code.
- Gain experience with the selected combustion model by applying it to test cases which have been reliably investigated in experiments and also comparing the results to other combustion models.
- Create a numerical model (grid and boundary conditions) of the experimental apparatus and perform simulations of the isothermal flow to check validity.
- Perform simulation of the reacting flow and check validity upon experimental results.
- Analysis of the reacting flow simulation results and extraction of informations regarding vortex breakdown.

1.5. Outline of this Work

The following first part deals with the theoretical prerequisites that were necessary for performing this work. Chapter 2 defines the basic set of equations that is the basis for the subsequent simulations and analysis. In chapter 3, the basics of chemistry and combustion are reviewed and methods for simplification of chemical systems are presented. Finally, the applied numerical procedures and models are discussed in chapter 4.

The second part deals with the actual work: the specifics of the implemented combustion model is described in chapter 5. The implementation has been validated on a number of test cases, the test cases and their results are presented in chapter 6. The combustion model is finally applied to simulations of the Combustion Induced Vortex Breakdown. All simulations and analysis concerning this phenomenon are presented in chapter 7.

The work closes with a summary given in chapter 8.

Part I.

Theoretical Preliminaries

2. Fluid Dynamics

The objective of fluid dynamics is the description of motion of fluids, i.e. matter, that unboundedly deforms under the influence of shear stresses. Fluid motion is usually described by the velocity of the fluid $\vec{v} = (u \ v \ w)^T$. Of common interest are also the pressure p , the fluid density ρ and the temperature T . The latter two can be considered constant in many applications, but generally not in combustion problems. These variables are functions of space and time.

2.1. Conservation Laws

The determination of the aforementioned interesting variables is possible by accounting of conserved variables. Conserved variables are physical variables that do not change their value in a closed system temporally. A number of conserved variables is known in physics, but in the simplest case of constant density flows, only mass m and momentum $m \vec{v}$ are relevant.

The mathematical formulation of conservation laws can be done by considering a space-fixed control volume. That leads to the so-called Eulerian formulation. With the help of Gauss's Theorem the integral formulation can be transformed into a differential formulation.

In the following sections, the basic conservation laws will be presented.

2.1.1. Mass

The mass conservation can be formulated verbally as follows: The temporal change of mass in a closed space-fixed control volume is equal to the sum of

2. Fluid Dynamics

- mass that is transported over the boundaries of the domain
- and mass that is removed or added inside the control volume per unit time.

This can be translated into the following integral formulation:

$$\int_{(V)} \frac{\partial \rho}{\partial t} dV + \int_{(A)} \rho \vec{u} \cdot d\vec{A} = \int_{(V)} \dot{m} dV \quad (2.1)$$

Without any mass sources or sinks and after application of Gauss's Theorem, (2.1) can be written as:

$$\int_{(V)} \left[\frac{\partial \rho}{\partial t} + \nabla \cdot (\rho \vec{u}) \right] dV = 0 \quad (2.2)$$

Equation (2.2) is satisfied, when the integrand is equal to zero everywhere in the control volume. This leads to the differential formulation:

$$\frac{\partial \rho}{\partial t} + \nabla \cdot (\rho \vec{u}) = 0 \quad (2.3)$$

Species Mass Conservation

If the fluid mechanical problem involves chemical reactions or mixing of fluid streams, the considered fluid is a mixture of multiple species. For the mass of each species, an own conservation equation can be written. The mass of each species i is usually expressed as fraction of the total mass:

$$Y_i = \frac{m_i}{m} \quad (2.4)$$

In analogy to section 2.1.1, the species mass conservation reads:

$$\int_{(V)} \frac{\partial(\rho Y_i)}{\partial t} dV + \int_{(A)} \rho \underbrace{(\vec{u} + \vec{V}_i)}_{\vec{v}} Y_i \cdot d\vec{A} = \int_{(V)} \dot{\omega}_i dV \quad (2.5)$$

Other than the overall mass, species mass can be destroyed or produced, since species may be destroyed or formed by chemical reactions. Therefore, a source term $\dot{\omega}_i$ appears in the right hand side of (2.5).

The velocity of species transport across the control volume boundaries \vec{v} is the sum of the fluid velocity \vec{u} and a diffusion velocity \vec{V}_i . Each species i diffuses with another diffusion velocity into the mixture. The diffusion velocity depends on pressure, temperature and

2. Fluid Dynamics

concentration gradients but usually only the concentration gradient is accounted. This leads to Fick's law, which reads:

$$\vec{V}_i Y_i = -D_i \nabla Y_i \quad (2.6)$$

where D_i is the diffusion coefficient of species i into the mixture.

After inserting (2.6) into (2.5), the species mass conservation reads in differential form:

$$\frac{\partial \rho Y_i}{\partial t} + \nabla \cdot (\rho \vec{u} Y_i) = \nabla \cdot (D_i \nabla Y_i) + \dot{\omega}_i \quad (2.7)$$

If the mass of all species is summed up, the global mass conservation equation must be recovered. So, the sum of all species source terms and diffusion velocities has to vanish:

$$\sum_{i=1}^{n_s} \dot{\omega}_i = 0 \quad \sum_{i=1}^{n_s} Y_i \vec{V}_i = 0 \quad (2.8)$$

If Fick's law is applied, the latter condition reads:

$$\sum_{i=1}^{n_s} -D_i \nabla Y_i = 0 \quad (2.9)$$

and is only satisfied if all D_i are equal.

2.1.2. Momentum

Since the first derivative of momentum with respect to time is a force, accounting momentum is related to balancing forces. A verbal formulation is as follows:

The temporal change of momentum in a closed, space-fixed control volume is equal to the sum of

- outer forces
- the flux of momentum through the boundaries of the control volume
- and momentum that vanishes or is produced inside the control volume per unit time.

2. Fluid Dynamics

This can be translated into the following integral formulation:

$$\int_{(V)} \frac{\partial(\rho \vec{u})}{\partial t} dV + \int_{(A)} (\rho \vec{u}) \vec{u} \cdot d\vec{A} = \sum \vec{f} = \int_{(A)} \mathbf{T} \cdot d\vec{A} + \int_{(V)} \rho \vec{f}_v dV \quad (2.10)$$

The two terms on the left hand side of equation (2.10) are the temporal change of momentum inside of the control volume and the momentum that is transported across the boundaries. The sum of forces on the right hand side consists of forces acting on the surface of the control volume and forces acting inside the volume. In analogy to mass sources and sinks in (2.1) they can be thought of as momentum sources and sinks.

The surface forces are expressed as an integral of stresses over the control volumes surface. For Newtonian fluids, the stress tensor \mathbf{T} can be written as a function of the velocity alone:

$$\mathbf{T} = - \left(p + \frac{2}{3} \mu \nabla \cdot \vec{u} \right) \mathbf{I} + 2\mu \mathbf{S} \quad (2.11)$$

with the strain rate tensor

$$\mathbf{S} = \frac{1}{2} \left[\nabla \vec{u} + (\nabla \vec{u})^T \right] \quad (2.12)$$

2.1.3. Energy

The energy conservation is described by the first law of thermodynamics. It states, that the change of internal energy ΔE in a closed system is equal to the sum of work W performed on the system and heat Q that flows into the system:

$$\Delta E = W + Q \quad (2.13)$$

When (2.13) is derived with respect to time and expressed with specific variables, it may be written as:

$$\int_{(V)} \frac{d(\rho e)}{dt} dV = \dot{W} + \dot{Q} \quad (2.14)$$

2. Fluid Dynamics

For an open system, e.g. a control volume in a fluid, convective transport of energy across the boundaries of the control volume has to be taken into account:

$$\int_{(V)} \frac{\partial(\rho e)}{\partial t} dV + \int_{(A)} (\rho e) \vec{u} \cdot d\vec{A} = \dot{W} + \dot{Q} \quad (2.15)$$

The total work may be divided into work done by external forces acting on the control volumes surface and into work done by external forces acting inside the volume (e.g. gravity)

$$\dot{W} = \underbrace{\int_{(A)} \vec{u} \cdot \vec{f}_A dA}_{\dot{W}_A} + \underbrace{\int_{(V)} \rho \vec{u} \cdot \vec{f}_V dV}_{\dot{W}_V} \quad (2.16)$$

Also the heat source may be divided into a heat flux across the boundaries and volumetric heat sources (e.g. caused by radiation)

$$\dot{Q} = \underbrace{\int_{(A)} \dot{q}_A dA}_{\dot{Q}_A} + \underbrace{\int_{(V)} \rho \dot{q}_V dV}_{\dot{Q}_V} \quad (2.17)$$

The surface work is done by the stress tensor (2.11)

$$\vec{f}_A = \mathbf{T} \vec{n} \quad (2.18)$$

and thus \dot{W}_A can be written as

$$\dot{W}_A = \int_{(A)} \vec{u} \cdot \mathbf{T} d\vec{A} \quad (2.19)$$

The heat flux across the boundaries is due to heat diffusion. Heat diffusion is usually described by Fourier's law:

$$\vec{q}_f = -\lambda \nabla T \quad (2.20)$$

and the diffusive flux across the boundary is

$$\dot{q}_A = -\lambda \nabla T \cdot \vec{n} \quad (2.21)$$

After inserting (2.19) and (2.21) into (2.15) and application of Gauss theorem, the energy

2. Fluid Dynamics

conservation law finally reads

$$\int_{(V)} \frac{\partial(\rho e)}{\partial t} dV + \int_{(A)} (\rho e) \vec{u} \cdot d\vec{A} = - \int_{(V)} \nabla \cdot (\lambda \nabla T) dV + \int_{(V)} \nabla \cdot (\mathbf{T}^T \vec{u}) dV + \int_{(V)} \rho \vec{u} \cdot \vec{f}_V dV + \int_{(V)} \rho \dot{q}_V dV \quad (2.22)$$

By inserting the definition of enthalpy $h = e + \frac{p}{\rho}$ into (2.22), an enthalpy conservation equation can be derived.

Usually, some terms in this equation may be neglected. If reacting flows and combustion problems are treated, viscous heating plays no role compared to the heat release due to chemical reaction. Also radiation is not important as long as the gas is optically thin and no soot is involved.

2.1.4. Equation of State

The connection between the different state variables is given by equations of state. These equations depend on the fluid under consideration. Very often and also throughout this work, all species and the mixture are assumed to be perfect gases. Also, ideal mixing is presumed.

For a perfect gas, there is a relation between pressure, temperature and density, known as the ideal gas law:

$$p = \rho \frac{\Re}{M} T \quad (2.23)$$

For a perfect gas, the internal energy as well as the enthalpy are functions of the temperature alone:

$$de = c_v dT \quad (2.24)$$

$$dh = c_p dT \quad (2.25)$$

These relations may be integrated from an appropriate reference point ($T_0 = 273.15K$) to yield an algebraic expression. Therefore, coefficients for polynomial fits of $c_p(T)$ are

2. Fluid Dynamics

provided, e.g. by [14]:

$$c_p(T) = \frac{\mathfrak{R}}{M} [a_4 T^4 + a_3 T^3 + a_2 T^2 + a_1 T + a_0] \quad (2.26)$$

Eq. (2.25) then can be integrated after substitution of (2.26). This yields an polynomial expression for the enthalpy as a function of the temperature:

$$h(T) = h_0 + \frac{\mathfrak{R}}{M} \left[\frac{a_4}{5} T^5 + \frac{a_3}{4} T^4 + \frac{a_2}{3} T^3 + \frac{a_1}{2} T^2 + a_0 T \right] \quad (2.27)$$

3. Chemical Reactions and Combustion

Chemical reactions lead to conversion of one species into another. Species mass is thus no conserved quantity. The production or destruction of species is represented by the source term $\dot{\omega}_i$ in equation (2.5). Species consist of elements (atoms), which are not affected by chemical reactions. Element mass is therefore a conserved quantity.

The conversion of species happens in elementary chemical reactions. In typical combustion processes, a large number of different elementary reactions take place and during these, a lot of intermediate species appear and disappear¹. A reaction may be generally expressed as

$$\sum_{i=1}^{n_s} \nu_{ij}^+ [X_i] \xrightarrow{k_{fj}} \sum_{i=1}^{n_s} \nu_{ij}^- [X_i] \quad (3.1)$$

where ν_{ij}^+ is the stoichiometric coefficient of specie i in reaction j on the reactants side and ν_{ij}^- the coefficient of specie i in reaction j on the product side.

The reaction rate is given by the rate coefficient k_{fj} . It is temperature dependent and usually computed by an Arrhenius approach

$$k_{fj} = B_j T^{b_j} \exp\left(-\frac{E_{aj}}{\mathfrak{R}T}\right) \quad (3.2)$$

The preexponential factor² B_j , the temperature exponent b_j and the activation energy E_{aj} are specific for each reaction j .

The net production rate of each species is the sum of the production rates due to all reactions. It depends on the rate coefficient as well as on the concentration of the

¹As an example: The GRI-MECH mechanism is often used for combustion of natural gas. The current version 3.0 [24] contains 325 reactions and 53 species.

²The unit of B_j depend on the reaction order, see Eq. (3.3)

provided reactants:

$$\frac{\rho}{M_i} \dot{\omega}_i = \frac{dc_i}{dt} = \sum_{j=1}^{n_r} -k_{fj} (\nu_{ij}^- - \nu_{ij}^+) \prod_{i=1}^{n_s} c_i^{\nu_{ij}^+} \quad (3.3)$$

3.1. Flames

This work focusses on combustion of gaseous fuels which involves chemical reactions between the fuel gas and the oxidizer (which is often air). Mixtures of air with common fuel gases as Methane, (vaporized) Octane or Hydrogen are essentially unreactive at room temperature and atmospheric pressure. Only beyond certain values of pressure and temperature, the mixture would become reactive and chemical reactions would occur throughout the whole volume. That is called explosion and the certain pressure and temperature values are given by the explosion limits. Explosions are hard to control and not commonly utilized in technical devices.

Instead, the explosion limits are reached only locally within a very narrow zone which propagates through the mixture and is called flame. Radiation is usually emitted by the hot gases in the reaction zone. Depending on the chemicals involved, the radiation contains a fraction in the visible part of the electromagnetic spectrum which causes the reaction zone to be visible by the human eye.

In technical applications, two types of flames are distinguished: the premixed flame, where fuel and oxidizer are mixed before combustion and the non-premixed flame, where mixing and combustion occur simultaneously. The intermediate case, where premixed and non-premixed regions appear, is called partially-premixed combustion.

3.1.1. Premixed Flame

When fuel and oxidizer are well mixed and the mixture ratio keeps within certain flammability limits, the mixture is able to form self-sustaining, propagating reactive waves after ignition. There are two modes of combustion wave propagation. In the first, the wave propagates at supersonic speed as a shock wave and the temperature rise across the shock

3. Chemical Reactions and Combustion

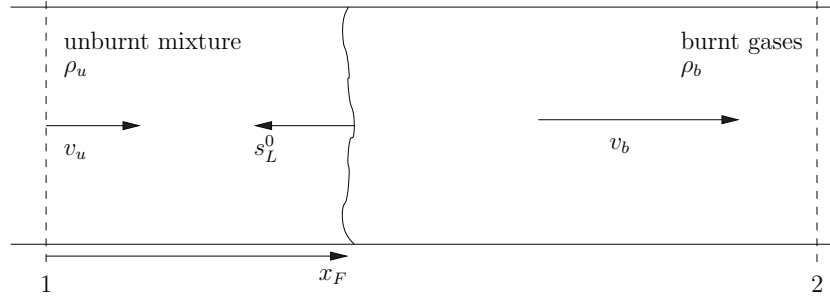


Figure 3.1.: Premixed flame

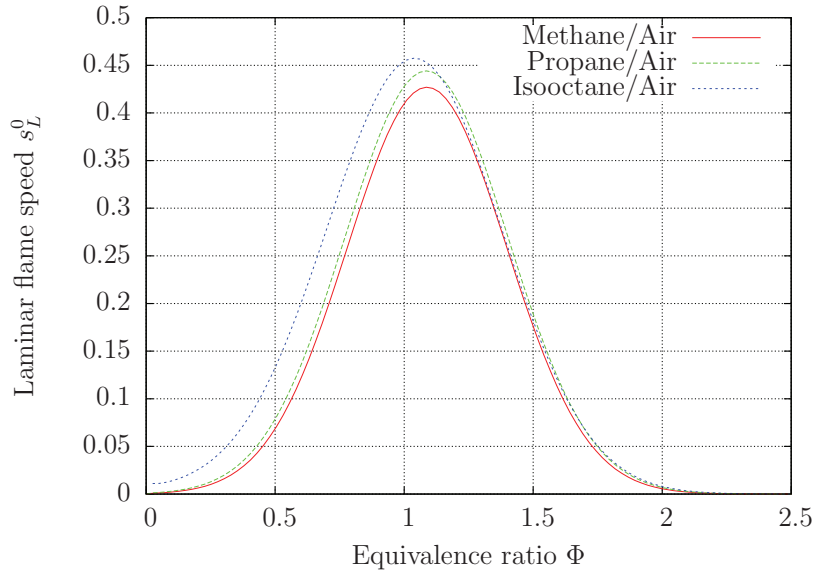


Figure 3.2.: Unstretched laminar flame speeds of different fuel/air mixtures

exceeds the explosion limits of the mixture. This mode is referred to as detonation and is not of interest subsequently. The second mode is commonly met in combustion devices and is called deflagration. The deflagration wave is sustained by diffusion of species and energy from the reaction zone into the fresh gases ahead. Diffusive processes are rather slow and therefore the speed of the deflagration wave is in the order of $20 \dots 100 \text{ cm/s}$ for common fuel/air combinations.

Laminar Premixed Flames

The simplest form of a deflagration wave is the unstretched laminar flat flame. The laminar flame propagates with a flame speed s_L^0 , which is defined as the propagation

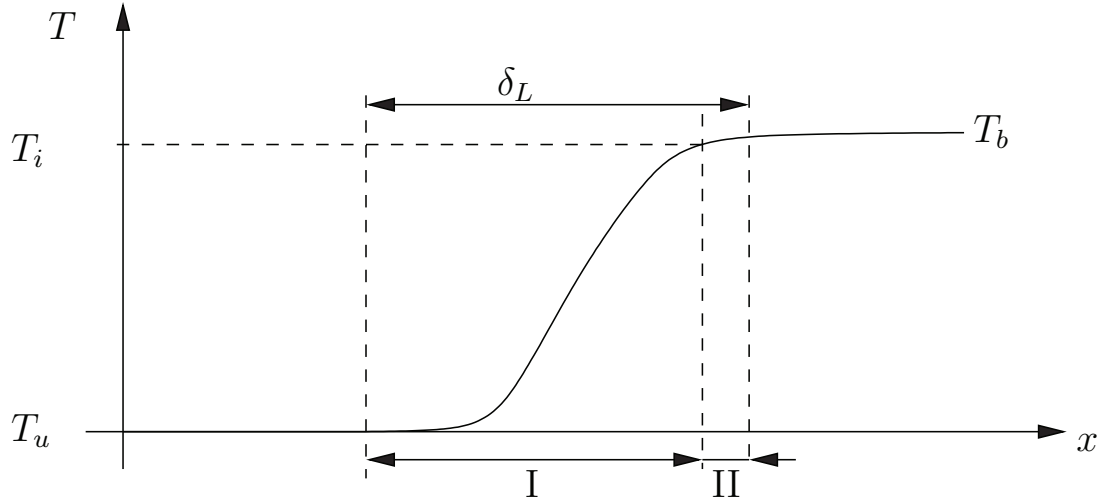


Figure 3.3.: Structure of a laminar premixed flame. I: preheat zone, II: reaction zone.

velocity of the flame front normal to itself and relative to the flow speed of the unburnt mixture. This is illustrated in figure 3.1. In the steady case, i.e. $x_F = \text{const}$, the fresh gases arrive with a velocity $v_u = s_L^0$. Since the density changes from ρ_u to ρ_b typically by a factor $\sigma = \frac{\rho_u}{\rho_b} \sim 5 \dots 10$, the velocity increases across the flame front and the burnt gases leave the control volume with a velocity $v_b = \sigma v_u$.

The laminar flame speed s_L^0 depends primarily on the equivalence ratio Φ and the temperature of the unburnt mixture T_u and may be computed numerically using detailed chemical mechanisms as an eigenvalue of the governing equation system.

The principal structure of a premixed laminar flame is sketched in figure 3.3. The chemical reactions take place in the narrow reaction zone denoted by II. From this high-temperature zone, radicals and energy diffuse against the convective flow into the fresh gases and cause a temperature rise in the preheat zone I (see e.g. [34]). The term “flame thickness” refers to the thickness of the preheat zones and the reaction zone together where temperature and species concentrations change and which has to be resolved in a numerical computation. From scaling laws, it may be approximated as

$$\delta_L = \frac{\lambda_u}{\rho_u c_p s_L} = \frac{\alpha_u}{s_L} \quad (3.4)$$

(see e.g. [70]). Eq. (3.4) usually gives too small estimates. If the temperature profile is

3. Chemical Reactions and Combustion

known, a more practical formula for the calculation of the flame thickness is

$$\delta_L^0 = \frac{T_b - T_u}{\max |\partial T / \partial x|} \quad (3.5)$$

The flame thickness is for hydrocarbon flames rather small and in the order of $\delta_L \approx 0.1mm$.

Turbulent Premixed Flames

In most combustion devices of technical importance, the flow is strongly turbulent. Flames in such devices are of course affected by the turbulent eddies. The type of interaction between a premixed flame and the turbulent eddies is commonly visualized in a combustion diagram. This diagram is based on comparing time and length scales. Basic time scales are the time scale of premixed combustion τ_c , turbulent mixing time scale τ_t and a Kolmogorov timescale τ_η :

$$\tau_c = \frac{\delta_L}{s_L} \quad \tau_t = \frac{L_t}{u'} \quad \tau_\eta = \frac{u'_\eta}{\eta_k} = \sqrt{\frac{\nu}{\epsilon}} \quad (3.6)$$

The dimensionless Damköhler number is the ratio of the mixing time scale to the combustion time scale:

$$Da = \frac{\tau_t}{\tau_c} = \frac{L_t s_L}{\delta_L u'} \quad (3.7)$$

The Karlovitz number is the ratio of the combustion time scale to the Kolmogorov time scale:

$$Ka = \frac{\tau_c}{\tau_k} = \sqrt{\frac{\epsilon}{\nu}} \frac{\delta_L}{s_L} \quad (3.8)$$

Additionally, a turbulent Reynolds number can be defined as

$$Re_t = \frac{u' L_t}{\nu} \quad (3.9)$$

3. Chemical Reactions and Combustion

If a unit Prandtl number $Pr = \nu/\alpha = 1$ is assumed, the approximation (3.4) can be rewritten as $\delta_L = \alpha/s_L = \nu/s_L$ and Eq. (3.9) becomes

$$Re_t = \frac{u' L_t}{s_L \delta_L} \quad (3.10)$$

With the help of the above defined time scales and dimensionless numbers, the boundaries of a number of combustion regimes can be drawn in a (u'/s_L) - (L_t/δ_L) -diagram as it is plotted in figure 6.1 [66]. The following regimes are distinguished:

- **Laminar flames** The region below the $Re_t = 1$ line in the lower left corner of the combustion diagram is the region of laminar flames.
- $Ka < 1$ In this region, the turbulent time scales are larger than the chemical time scales and the length scales of the smallest turbulent eddies is still larger than the flame thickness. The flame front therefore remains thin and its inner structure is essentially that of a laminar flame. The interaction between flame and turbulence is purely kinematic. This “flamelet regime” may be subdivided into
 - **Wrinkled flamelets** This is the area below the $u'/s_L = 1$ line which means that the turbulent fluctuations are smaller than the laminar flame speed $u' < s_L$ and only slight wrinkling of the flame front is observed.
 - **Corrugated flamelets** The turbulent fluctuations become larger than the laminar flame speed and a wrinkling of the flame front with formation of pockets of fresh and burnt gas is possible.
- $Ka > 1$ This condition implies that the smallest turbulent eddies are now small enough to penetrate into the laminar flame front layer. The condition $Ka = 1$ is also known as the Klimov-Williams criterion. To quantify the level of interaction of the turbulent eddies with the flamelet layers, a second Karlovitz number Ka_δ may be defined which relates the reaction zone thickness $l_\delta = \delta_R \delta_L$ to the size of the Kolmogorov eddies η^3 :

$$Ka_\delta = \frac{l_\delta^2}{\eta^2} = \delta_R^2 Ka \quad (3.11)$$

The line $Ka_\delta = 1$ now separates the two further regimes

³The ratio of reaction zone thickness to total flame thickness is e.g. $\delta_R \approx 0.1$ for a stoichiometric methane/air flame at atmospheric pressure.

3. Chemical Reactions and Combustion

- **Thin reaction zones** Here, the condition $Ka_\delta < 1$ holds and the turbulent eddies do enter the preheat zone but not the reaction zone. The flame front structure is no longer laminar since turbulence may enhance or weaken the transport of species or energy in the preheat zone but the chemical reactions are not influenced by turbulence. The flame front is substantially wrinkled.
- **Broken reaction zones** Since $Ka_\delta > 1$, the turbulent eddies are now penetrating the reaction zone. This may lead to a local loss of heat and radicals and suppression of the chemical reactions. Thus, local extinction may occur.

Most combustion problems of technical relevance are located in the corrugated flamelets or thin reaction zones regimes.

3.1.2. Non-Premixed Flames

In non-premixed or diffusion flames the reactants are not premixed but do mix and react simultaneously. Two boundary states occur: the pure oxidizer and the pure fuel. In the mixing zone of these two states, the chemical reactions occur. The reaction zone is inside a limited range around the stoichiometric mixture which occurs somewhere between the fuel and oxidizer stream, because at some distance from each side of the stoichiometric surface, the mixture is either too lean or too rich for reaction.

A non-premixed flame can only be steady if a strain occurs, i.e. the reaction zone needs to be continuously fed by fuel and oxidizer. Otherwise, the reaction rate decreases in time because the educts are depleted. Unlike the premixed flame, a non-premixed flame does not have a characteristic propagation speed or thickness because these properties are controlled by the mixing process and therefore the flow properties.

For industrial combustion application, non-premixed flames have the advantage of simpler design and safer operation since the flame cannot propagate or flash back. A disadvantage is an increased amount of soot and emissions.

In non-premixed flames the reaction rate is controlled by the mixing process instead of the chemistry which can be regarded as infinitely fast. It is therefore possible to split the solution into the solution of a mixing problem and then to superimpose a flame structure. The mixing is commonly described by a mixture fraction Z which represents elemental composition. Since elemental composition is unaffected by chemical reactions,

3. Chemical Reactions and Combustion

determination of the mixture fraction requires solution of a passive scalar transport equation without source terms:

$$\frac{\partial \rho Z}{\partial t} + \nabla \cdot (\rho \vec{u} Z) = \nabla \cdot (\rho D_Z \nabla Z) \quad (3.12)$$

It is common to normalize the mixture fraction such that $Z = 0$ in the oxidizer stream and $Z = 1$ in the pure fuel stream.

The flame structure now describes the properties of the reacting mixture (density, temperature etc.) as a function of Z . The coupling of the flame structure and the mixing problem (3.12) happens through the density field $\rho(Z)$.

After making some certain assumptions (see e.g. [70]), an equation for the flame structure can be derived by transforming the species mass balance into Z -space, i.e. from the global (x_1, x_2, x_3, t) coordinate system into a (Z, y_1, y_2, t) system where y_1 and y_2 are spatial coordinates tangential to a Z isosurface:

$$\rho \frac{\partial Y_i}{\partial t} = \dot{\omega}_i + \rho D \|\nabla Z\|^2 \frac{\partial^2 Y_i}{\partial Z^2} = \dot{\omega}_i + \frac{1}{2} \rho \chi_Z \frac{\partial^2 Y_i}{\partial Z^2} \quad (3.13)$$

The quantity $D \|\nabla Z\|^2 = \chi_Z$ is the so-called scalar dissipation.

The solutions of (3.13) yield the composition $Y_i(Z, \chi_Z, t)$ and thereof $\rho(Z, \chi_Z, t)$. A commonly used assumption is to regard the flamelet as steady, even though the flow is not steady. In this case (3.13) reduces to

$$\dot{\omega}_i = -\frac{1}{2} \rho \chi_Z \frac{\partial^2 Y_i}{\partial Z^2} \quad (3.14)$$

and the solutions $Y_i(Z, \chi_Z)$ and $\rho(Z, \chi_Z)$ do depend on Z and χ_Z only.

Turbulence has a major impact on mixing but on the flame structure as well. Anyhow, it is mostly assumed that the flamelet structure prevails and the decomposition into a mixing problem and the independent flame structure remains valid. Since numerical simulations yield mean or filtered values of Z , it becomes difficult to compute χ_Z in eq. (3.13). The modeling of χ_Z is one central problem in turbulent non-premixed combustion. The turbulent non-premixed combustion models are often based on presuming PDF shapes for Z and χ_Z . Then, the averaged or filtered quantities can be closed by

integrating over the PDF's:

$$\bar{\rho} = \int_0^{\infty} \int_0^1 \rho(Z, \chi_Z) P_Z(Z) P_{\chi}(\chi_Z) dZ d\chi_Z \quad (3.15)$$

In the above expression, the quantities Z and χ_Z are treated as statistical independent because the joint probability density of both quantities is the product of two one-dimensional PDF functions $P_Z(Z)$ and $P_{\chi}(\chi_Z)$. Although this simplification is made very often, it is seldomly justified. But it is used anyway because it is very difficult to presume PDF shapes for multidimensional joint PDFs.

3.1.3. Partially Premixed Flames

The partially-premixed regime is a hybrid regime of both the premixed and non-premixed regime. The canonical sample problem for this combustion mode is a lifted jet diffusion flame (see figure 3.4(a)): When the nozzle exit velocity of the fuel stream exceeds some critical value, the flame would be extinguished immediately downstream the nozzle because of the high stretch there and thus stabilizes some distance downstream. At this “lift-off height”, the fuel and oxidizer stream are already partially mixed and the equivalence ratio is stratified.

Combustion in such a stratified mixture generates a structure which is called a triple flame. This structure is a key element in partially-premixed combustion. It is illustrated in figure 3.4(b): The triple flame has a flame front like a premixed flame which propagates into the unburnt mixture. The flame speed is a function of the equivalence ratio, the maximum flame speed occurs near the stoichiometric equivalence ratio. The flame front is therefore curved. On the burnt gas side of the lean flame front, there is still oxidizer left over while behind the rich flame front, fuel remains. These components form a second reaction zone after the premixed fronts: a diffusion flame appears between the rich and the lean branch. All three branches (the rich and the lean premixed front and the diffusion flame) merge in a common point, the so-called triple point.

This flame structure illustrates the features of partially-premixed combustion: There are flame fronts that propagate into a flammable but inhomogeneous mixture like in the premixed regime and are controlled by the chemical kinetics. But furthermore, there are regions where the combustion is controlled by mixing processes.

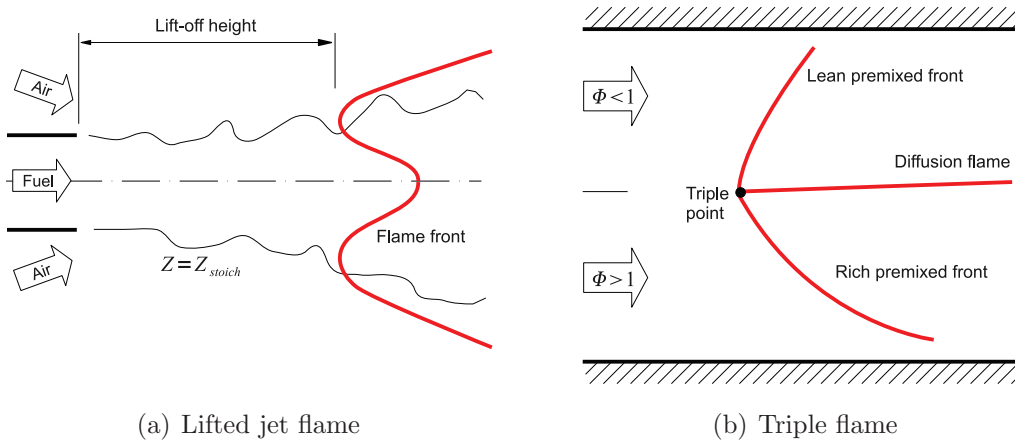


Figure 3.4.: Examples for partially-premixed flame configurations

Modeling of this kind of combustion thus needs to take the inhomogeneity of mixture into account, i.e. the mixture fraction is needed. And additionally, a chemical progress variable is required to describe the reaction rate controlled premixed part.

3.2. Simplifications of Chemical Mechanisms

As already mentioned, chemical mechanisms usually contain a large number of species and reactions. To compute a reacting flow using such a mechanism, an equally large number of transport equations has to be solved. Many of the species are merely intermediate species and of no real interest for the user. Furthermore, the involved radicals have a short lifetime and very high net productions rates which depend strongly nonlinear on the concentrations of other species and temperature. This leads to very stiff equations and modeling problems that grow with the size of the mechanism. It is therefore highly desirable to somehow reduce the dimensionality of the chemical reaction system. Different methods have been developed in the past.

3.2.1. One-Step Chemistry

The most simplifying approach is to describe the entire reaction system by only one single reaction. Of course no intermediate species can be described then and the number of

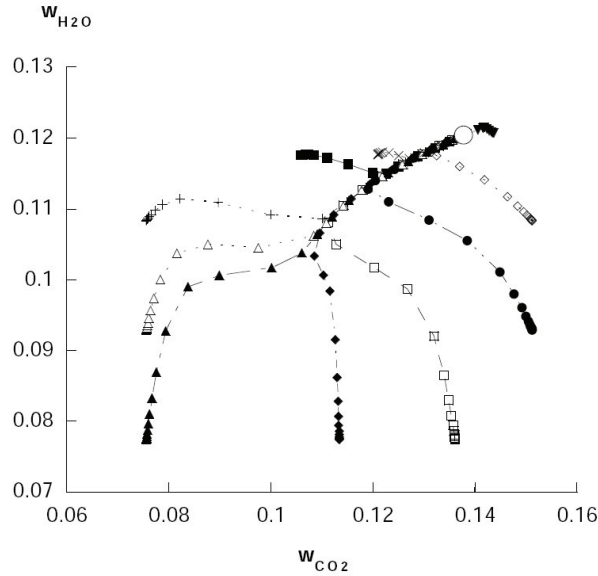


Figure 3.5.: Reactions paths of a homogeneous methane-air system, projected onto the Y_{CO_2} - Y_{H_2O} -Plane [78].

species is reduced to the major educts and products. The brutto reaction is not really taking place but nevertheless fitted rate constants are available in the literature.

If a homogeneous combustion system is described by a one-step reaction, a single combustion progress variable is sufficient to describe the chemistry.

3.2.2. Intrinsic Low-Dimensional Manifolds

The general idea behind ILDM is probably best explained using figure 3.5 which is taken from [78]. It displays the reaction paths of a homogeneous methane-air system in the chemical state space. This space is spanned by the mass fractions of all species Y_i , the pressure p and enthalpy h . At a certain time, the state of the system is represented by a point in this multidimensional state space. Chemical reactions change the species composition of the system and during the reaction process, so the system state moves along a trajectory through the state space. The trajectory connects the initial state with the final state, i.e. the equilibrium state.

Since it is not possible to display a multidimensional trajectory here, only projections of trajectories onto a certain plane in state space are displayed in figure 3.5. Lines

3. Chemical Reactions and Combustion

with different symbols denote paths from different initial compositions. Since all initial compositions were chosen to have the same elementary composition, they all end up in the same equilibrium point (denoted with an empty circle).

The remarkable feature of the system behavior is, that all trajectories converge together towards an attracting manifold, long before the system state reaches the equilibrium. The velocity of the system along the trajectory is not apparent from 3.5, but it may be noted here, that the movement along the common manifold is very slow, compared to movement towards this manifold. The common manifold is henceforth referenced to as Intrinsic Low-Dimensional Manifold (ILDM) of the chemical system.

This observation leads to the following idea concerning the modeling: System states off the manifold quickly relax towards the manifold. This happens within time scales that cannot be resolved. The system state then moves slowly along the common manifold. This has to be resolved. It is therefore sufficient to presume that the system state is always on the manifold. This is reasonable because of the fast relaxation towards the manifold. Since the manifold has a lower dimension than the entire state space, a smaller number of parameters is sufficient to represent the system state.

Instead of solving equations for each species mass, equations for the manifold parameters are solved. These parameters are usually properly chosen mass fractions or linear combinations of mass fractions.

3.2.3. Computation of ILDM's

The concept of ILDM was first developed by Maas and Pope [58]. The computation of the ILDM is based on a eigenvalue analysis of the simplified set of governing equations for the chemical system which can be derived after rearranging (2.7) to

$$\frac{\partial \rho Y_i}{\partial t} = \underbrace{\dot{\omega}_i}_I + \underbrace{\nabla \cdot (D_i \nabla Y_i)}_{II} - \underbrace{\nabla \cdot (\rho \vec{u} Y_i)}_{III} \quad (3.16)$$

Eq. (3.16) contains the chemical source terms I and also convective (II) and diffusive (III) transport of species. The latter two terms are neglected and if enthalpy and pressure

3. Chemical Reactions and Combustion

are constant, the evolution of the system is governed by

$$\frac{\partial \vec{\psi}}{\partial t} = \frac{\dot{\omega}}{\rho} = \vec{F}(\vec{\psi}) \quad (3.17)$$

where $\vec{\psi} = (Y_1, \dots, Y_n)^T$. At first, the system is linearized around a state $\vec{\psi}_0$:

$$\frac{\partial \vec{\psi}}{\partial t} = \vec{F}(\vec{\psi}_0) + \left. \frac{\partial \vec{F}}{\partial \vec{\psi}} \right|_{\vec{\psi}_0} (\vec{\psi} - \vec{\psi}_0) + \text{h.o.t.} \quad (3.18)$$

where $\mathbf{F}_\psi = \partial \vec{F} / \partial \vec{\psi}$ is the Jacobian of \vec{F} .

The Jacobian can be decomposed such that

$$\mathbf{F}_\psi = \mathbf{U} \mathbf{J} \mathbf{U}^{-1} \quad (3.19)$$

where the matrix \mathbf{U} contains the eigenvectors of \mathbf{F}_ψ in its columns whereas the rows of \mathbf{U}^{-1} contain the left eigenvectors of \mathbf{F}_ψ . If all eigenvalues are real, then \mathbf{J} is a diagonal matrix which contains the eigenvalues λ_i of \mathbf{F}_ψ on its diagonal: $J_{ii} = \lambda_i$.

Using this decomposition, the linearized system (3.18) can be expressed as

$$\frac{\partial \vec{\phi}}{\partial t} = \mathbf{U}^{-1} \vec{F}(\vec{\psi}_0) + \mathbf{U}^{-1} \left. \frac{\partial \vec{F}}{\partial \vec{\psi}} \right|_{\vec{\psi}_0} \mathbf{U} \vec{\phi} = \mathbf{U}^{-1} \vec{F}(\vec{\psi}_0) + \mathbf{J} \vec{\phi} \quad (3.20)$$

where $\vec{\phi}$ is the time derivative of the system transformed into the eigensystem: $\mathbf{U} \vec{\phi} = (\vec{\psi} - \vec{\psi}_0)$.

If ϕ is regarded as a perturbation from the linearization point $\vec{\psi}_0$, it can be shown, that the system answer develops in time according to

$$\|\phi_i\| = \exp(\lambda_i t) \|\phi_i(t=0)\| \quad (3.21)$$

Therefore, the eigenvalues describe the dynamics of the corresponding process:

- $\lambda < 0$: The perturbation decays in time. The larger negative λ is, the faster is the decay.
- $\lambda = 0$: The perturbation remains constant.

3. Chemical Reactions and Combustion

- $\lambda > 0$: The perturbation increases with time.

Provided that the eigenvalues in \mathbf{J} are ordered such that the largest eigenvalue appears as J_{11} and the smallest (largest negative) one as J_{nn} and the eigenvectors in \mathbf{U} and \mathbf{U}^{-1} are ordered accordingly, the transformed system (3.20) can be split into two systems, the first describing the motion of the slow processes and the second describing the fast processes:

$$\frac{\partial \vec{\phi}_s}{\partial t} = \mathbf{U}_s^{-1} \vec{F}(\vec{\psi}_0) + \mathbf{J}_s \vec{\phi} \quad (3.22)$$

$$\frac{\partial \vec{\phi}_f}{\partial t} = \mathbf{U}_f^{-1} \vec{F}(\vec{\psi}_0) + \mathbf{J}_f \vec{\phi} \quad (3.23)$$

where \mathbf{U}_s^{-1} and \mathbf{U}_f^{-1} are submatrices of \mathbf{U}^{-1} :

$$\mathbf{U}_s^{-1} = \begin{pmatrix} \vec{e}_1^L \\ \vec{e}_2^L \\ \vdots \\ \vec{e}_{n_s}^L \end{pmatrix} \quad \mathbf{U}_f^{-1} = \begin{pmatrix} \vec{e}_{n_s+1}^L \\ \vec{e}_{n_s+2}^L \\ \vdots \\ \vec{e}_n^L \end{pmatrix} \quad (3.24)$$

and \mathbf{J}_s^{-1} and \mathbf{J}_f^{-1} are submatrices of \mathbf{J} with sizes of $n_s \times n_s$ and $(n - n_s) \times (n - n_s)$ respectively:

$$\mathbf{J} = \begin{pmatrix} \mathbf{J}_s & \mathbf{0} \\ \mathbf{0} & \mathbf{J}_f \end{pmatrix} \quad (3.25)$$

The size of the slow subsystem n_s may be chosen arbitrarily although it has to be larger than the number of elements n_e in the system, because the elementary composition is not affected by chemical reactions and cannot be reduced.

For system states on the low-dimensional manifold, all fast processes shall be relaxed, i.e. the time derivative of the fast processes should vanish if $\vec{\psi}_0$ is on a manifold and they should be nonzero if the system state departs from the manifold ($\vec{\phi} \neq 0$). This leads to the following condition:

$$\mathbf{U}_f^{-1} \vec{F}(\vec{\psi}_0) = \vec{0} \quad (3.26)$$

If this condition is satisfied, the system state $\vec{\psi}_0$ is on a $n_s - n_e$ dimensional attracting manifold in the system state space.

3. Chemical Reactions and Combustion

For the numerical evaluation, it is more appropriate to use a Schur decomposition rather than eigenvalues (see e.g [78] for an extensive description). There are different possible algorithms for the solution of (3.26), see e.g. [57], [74] or [60].

Although this computation via eigenvalue analysis is elegant, it is limited by the fact that diffusion is not taken into account. It can be shown that the manifold is invariant with respect to convection but diffusion gets dominating over chemical reactions the more the system state departs from equilibrium and approaches the unburnt state.

3.2.4. Reaction-Diffusion Manifolds (REDIM)

An extension of the ILDM method to include diffusion has been recently developed by Bykov and Maas [9, 10]. The basic equation is (3.16):

$$\frac{\partial \vec{\psi}}{\partial t} = \underbrace{\frac{\dot{\omega}_i}{\rho}}_I + \underbrace{\frac{1}{\rho} \nabla \cdot (D \nabla \vec{\psi})}_{II} - \underbrace{\nabla \cdot (\vec{u} \vec{\psi})}_{III} = \vec{G}(\psi) \quad (3.27)$$

Unlike Eq. (3.17), this equation contains not only temporal derivatives of the state variables but also spatial ones.

It is now assumed, that the solution of the system depends on the coordinates θ which parameterize the low-dimensional manifold: $\vec{\psi}(t, \vec{x}) = \vec{\psi}(\vec{\theta}(t, \vec{x}))$. After application of the chain rule, Eq. (3.27) can be rewritten:

$$G_i = \frac{\dot{\omega}_i}{\rho} + \frac{1}{\rho} D \frac{\partial^2 \psi_i}{\partial x_k \partial x_k} - u_k \frac{\partial \psi_i}{\partial x_k} \quad (3.28)$$

$$= \frac{\dot{\omega}_i}{\rho} + \frac{1}{\rho} D \frac{\partial \psi_i}{\partial \theta_j} \frac{\partial^2 \theta_j}{\partial x_k \partial x_k} - u_k \frac{\partial \psi_i}{\partial \theta_j} \frac{\partial \theta_j}{\partial x_k} \quad (3.29)$$

Bykov and Maas suggest to find the REDIM from the system's evolution equation (3.29) by solving a PDE in the low-dimensional parameter space. This method has already been applied for computation of ILDM's before [60]. The PDE is solved for the manifold $\vec{\Psi}(\theta)$ by advancing in pseudo time t^* until a steady state:

$$\frac{\partial \vec{\Psi}}{\partial t^*} = (\mathbf{I} - \Psi_\theta \Psi_\theta^+) \cdot \vec{G} \quad (3.30)$$

3. Chemical Reactions and Combustion

with $\Psi_\theta = \partial\Psi_i/\partial\theta_j$ and Ψ_θ^+ being the Moore-Penrose pseudo-inverse of Ψ_θ : $\Psi_\theta^+ = (\Psi_\theta^T \Psi_\theta)^{-1} \Psi_\theta^T$.

After inserting (3.29) into (3.30), the convective term cancels out:

$$\frac{\partial \vec{\Psi}}{\partial t^*} = (\mathbf{I} - \Psi_\theta \Psi_\theta^+) \cdot \left(\frac{\vec{\omega}}{\rho} - \frac{1}{\rho} \Psi_{\theta\theta} : (\nabla\theta \nabla\theta) \right) \quad (3.31)$$

This PDE has to be solved to get the manifold but it still contains the spatial gradient of the manifold parameters. It can be further modified to reduce to required information to only the magnitude of the gradient (see [10] for details):

$$\frac{\partial \vec{\Psi}}{\partial t^*} = (\mathbf{I} - \Psi_\theta \Psi_\theta^+) \cdot \left(\frac{\vec{\omega}}{\rho} - \frac{1}{\rho} D \|\Psi_\theta^T \nabla \vec{\Psi}\|^2 \frac{1}{m_s} \text{tr} \mathbf{A} \right) \quad (3.32)$$

where the tensor \mathbf{A} depends not on spatial gradients:

$$\mathbf{A} = (\Psi_\theta^T \Psi_\theta)^{-1} \Psi_{\theta\theta} (\Psi_\theta^T \Psi_\theta)^{-1} \quad (3.33)$$

and m_s is the dimensionality of the desired REDIM parameter space. Eq. (3.32) is a stiff m_s -dimensional partial differential equation and sophisticated numerics is involved in its solution. It can be solved for the REDIM if an estimate of the spatial gradient of the state vector is available. It could be extracted from a detailed flame simulation, for example.

3.2.5. Flamelet Generated Manifolds (FGM)

This method has been developed by van Oijen et al. [83, 84] and is very similar to the FPI method by Gicquel et al. [32]. The principal idea is that the thermochemical states in a laminar flamelet lie on a one-dimensional attracting manifold in state space.

Thus, after computation of a laminar flamelet, a suitable parameterization has to be chosen, usually a linear combination of selected species mass fractions and the states from the flamelet can be readily tabulated. When heat losses or a variable mixture fraction have to be considered, multiple flamelets with different initial temperatures or compositions have to be computed. The number of flamelets depends on the desired tabulation resolution.

3. Chemical Reactions and Combustion

The advantage of this manifold computation method over the formerly introduced ones is that diffusion is included in a natural way and furthermore it is relatively easy to compute the chemistry table because reliable codes for flamelet computation exist and can be used. The disadvantage with respect to REDIM is that an extension to multiple chemical progress variables is rather cumbersome.

4. Numerical Methods for Computational Fluid Dynamics

The fundamental equations, that were presented in the preceding chapters, fully describe a reacting flow problem. But they are nonlinear, partial differential equations. Closed analytical solutions only exist for a few simple cases. For the solution of common engineering problems, only approximate numerical procedures come into consideration.

The basis for numerical solutions of PDE's is the decomposition of the solution domain into a number of subdomains (usually called elements or cells) which are so small, that simplifying assumptions are valid within them. The introduction of ansatz functions for the solution quantity inside the elements leads to the Finite Element Method (FEM). The identification of the cells with the control volumes of the conservation laws of section 2.1 and regarding the quantity as constant within the control volume leads to the Finite Volume Method (FVM).

For the numerical solution of flow problems, the Finite Volume Method is usually applied. In the following chapters, only the FVM is considered.

4.1. Finite Volume Method

4.1.1. Spatial Discretization

Spatial discretization in the FVM means decomposition of the solution domain into smaller control volumes (cells), i.e. the generation of a computational grid. The shape of these control volumes is arbitrary. However, for each of the faces of the control volume, face-averaged fluxes have to be calculated from the discretized quantity. Therefore,

interpolation of the quantity and its derivatives is necessary. This interpolation is not equally simple for each type of grid and so some preferences arise.

The simplest case are cartesian structured meshes. The control volumes are hexahedra and their faces coincide with the coordinate planes. Interpolation is done along the coordinate lines.

The introduction of curvilinear coordinates in structured meshes enables the treatment of more complex geometries. But the application remains limited to domains, that can be mapped onto hexahedra. Furthermore, a local refinement of the grid resolution is not always simple. For engineering applications, a structured mesh is not always sufficient. An improvement is the usage of block-structured meshes, i.e. an assembly of multiple structured meshes (blocks) to form the computational domain.

In a numerical simulation with a block-structured mesh, the generation of the mesh is usually the most time-consuming part of the work. In particular, it is difficult to automate. But well proven algorithms exist for the automatic decomposition of a domain into tetrahedra. This results in a unstructured mesh. The faces of the control volumes no longer coincide with coordinate planes and the interpolation becomes more difficult. On the other hand, arbitrary complicated volumes may be meshed easily. The interpolation and mesh quality can be improved by not using the tetrahedral meshes directly but their geometric dual. This results in so called polyhedral meshes. The numerical accuracy of this kind of meshes can be rated between tetrahedral and hexahedral meshes. See e.g. [46] for a comparison.

4.1.2. Temporal Discretization

After applying the spatial discretization, the partial PDE's in space and time have become ordinary differential equations in time.

For integrating these ODE's in time, different methods are applicable. They can be divided into explicit and implicit methods. In explicit methods, the time derivatives from the old time step are integrated. All quantities at the old time steps are known and the time derivatives can therefore be explicitly computed. The explicit methods do not require the solution of a algebraic equation system. However, explicit methods are only conditionally stable. The maximum admissible time step is dictated by the Courant-Friedrichs-Levy criterion.

In implicit methods, the time derivatives at the new time step are integrated. All quantities at the new time step are unknown and a system of nonlinear equations arises that has to be solved. Implicit methods are stable for much larger time steps than explicit methods and the time step size may be chosen according to accuracy needs.

4.1.3. Treatment of the Pressure

A problem with the pressure arises only when the flow is incompressible, i.e. the density is independent from the pressure. In compressible flows, the pressure can be computed from the equation of state (see section 2.1.4). It is then dependent from the density ρ and the temperature T and therefore eliminated from the equation system. The conservation laws of momentum, mass and energy together form an equation system with the unknowns \vec{v} , ρ and T .

In incompressible flows, the density is a constant and uncoupled from pressure. But even when density changes due to chemical reactions or phase changes occur, the flow is incompressible if only the density is not dependent on pressure. In the Navier-Stokes Equations there exists no equation for the pressure. For explicit time integration methods the problem arises, that no time derivative for the pressure can be calculated. For implicit methods, a badly conditioned equation system results.

A common cure is the application of a pressure correction method. The basic idea is best illustrated at the constant density case: First, the momentum equations are integrated using a guess for the pressure. The resulting velocities will not fulfill the continuity equation. The continuity equation becomes a constraint for the velocity field in this case. It can be combined with the momentum equation to a so called pressure correction equation. The solution of this equation is the pressure field. Using this pressure field, the formerly computed velocities can be corrected such that they fulfill the continuity constraint.

4.2. Turbulent Flows

The term “turbulence” labels a chaotic, stochastic and strongly unsteady motion of fluid particles in a turbulent flow. An organized, laminar flow becomes turbulent, if a

4. Numerical Methods for Computational Fluid Dynamics

certain Reynolds number is exceeded that depends on the particular flow configuration. The organized flow pattern then becomes unstable and a transition into a turbulent flow appears.

An important attribute of a turbulent flow is the intensified momentum and mass transfer transverse to the dominating flow direction which is caused by the chaotic fluid motion. This turbulent diffusion can be orders of magnitude larger than the molecular diffusion.

The turbulent motion is described by the Navier-Stokes Equation. In a numerical simulation, only flow structures above a certain size can occur because of the spatial discretization. To resolve the turbulence, all time and length scales have to be resolved. Between the largest flow structures of size L and the smallest occurring structures of approximately size η , the ratio is $L/\eta \approx Re_{u'}^{3/4}$. $Re_{u'}$ is the Reynolds number that is formed with the characteristic fluctuation velocity u' : $Re_{u'} = \frac{u'L}{\nu}$. In a channel flow for example, it can be estimated by $Re_{u'} \approx Re^{0.9}$ where Re is the Reynolds number formed with the channel height and the velocity at the channel centerline. The Reynolds numbers of flows with practical relevance are typically very large ($Re > 10^6$). This requires on the one hand a fine spatial resolution of the flow domain. On the other hand, turbulent flows are unsteady and the simulation has to be carried out instationarily with a sufficiently small time step. For flow problems of relevance for engineering, enormous requirements for computation time and storage capacity arise.

A numerical simulation, that satisfies this resolution requirements is very resource demanding but for simple flow problems quite possible. It is called Direct Numerical Simulation (DNS) and finds its application in fundamental research, virtually as a “numerical experiment”. These simulations depict great details of the turbulence, that can be hardly measured in real experiments.

In simulation of engineering type flow problems, often only averaged quantities are of real interest. So, the idea is obvious to solve only for mean quantities. According to Osborne Reynolds, a turbulent quantity ϕ can be decomposed into a time average and a fluctuation part:

$$\phi = \langle \phi \rangle + \phi' \quad (4.1)$$

where the time average $\langle \phi \rangle$ is defined as:

$$\langle \phi \rangle = \lim_{T \rightarrow \infty} \frac{1}{T} \int_0^T \phi(t) dt \quad (4.2)$$

When the Navier-Stokes Equations are averaged according to Eq. (4.2), the Reynolds-averaged Navier-Stokes Equations arise (RANS, Reynolds Averaged Navier Stokes). The nonlinearity of the convective term in the momentum equation and the calculation rules for the averaging operator lead to a new term in the RANS equations. It has the dimension of stress and is therefore called Reynolds stress tensor. Physically, it represents the influence of the turbulent motions on the resolved, averaged fluid motion. Since the turbulent motions are not a result of the RANS equations, this term has to be modelled.

The Reynolds stresses are influenced by the turbulent motions of all length scales. Especially the large scale structures are anisotropic and hard to model. The applied models are therefore of empirical character. They contain constants, that have to be fitted to the flow configuration under consideration.

Another technique for the turbulence treatment is the Large-Eddy Simulation (LES). The idea is to simulate a part of the turbulence, i.e. the large scale structures (large eddies) and model the small structures, that cannot be resolved on the computational grid. The small structures can be assumed to be isotropic and homogeneous. This enables a simple modelling but only applies to the small structures. The separation of the small structures is effectively achieved by the limited resolution of the computational grid. Formally, the LES equations are derived by applying a spatial filter. The result of the filtering operation is a stress term, analogous to term in the RANS equations. Its components are called SGS stresses (subgrid scale). Again, this term represents the influence of the unresolved turbulent motion onto the resolved one.

4.3. Large-Eddy Simulation

4.3.1. Spatial Filtering

Filtering of a quantity ϕ is defined by the convolution integral

$$\bar{\phi}(x) = \int_{-\infty}^{+\infty} G(x - x') \phi(x') dx' \quad (4.3)$$

The quantity may be decomposed into a filtered part and a SGS fluctuation part

$$\phi(x) = \bar{\phi}(x) + \phi'(x) \quad (4.4)$$

The filter kernel G is a compactly supported function. A characteristic length Δ is connected to the filter. Roughly, structures smaller than Δ are filtered out while larger structures pass the filter. A filter commonly used to represent the filtering effect of the finite volume method is the box filter G_B .

$$G_B(x) = \begin{cases} 1/\Delta & \text{if } x < \Delta \\ 0 & \text{otherwise} \end{cases} \quad (4.5)$$

In the description of variable density flows, filtered terms of the form $\overline{\rho\phi}$ occur. To avoid the occurrence of unclosed terms when splitting these unknown products, the density weighted Favre filtering is used instead. It defined by

$$\tilde{\phi} = \frac{\overline{\rho\phi}}{\bar{\rho}} \quad (4.6)$$

With this definition, the unclosed products can be rewritten as

$$\overline{\rho\phi} = \bar{\rho}\tilde{\phi} \quad (4.7)$$

The solution process now yields density weighted filtered quantities $\tilde{\phi}$ instead of only spatially filtered values. This should be kept in mind, e.g. when comparing results to experimental data.

4.3.2. LES Equations

Momentum Equation

The LES momentum equation is derived by filtering the conservation law of momentum from section 2.1.2. Since the focus in the following is on reactive flows with variable density, the Favre filter is applied.

$$\frac{\partial(\bar{\rho}\tilde{u})}{\partial t} + \nabla \cdot (\bar{\rho}\tilde{u}\tilde{u}) = \nabla \cdot [\mu(\nabla\tilde{u} + (\nabla\tilde{u})^T)] - \frac{2}{3}\nabla [\mu\nabla \cdot \tilde{u}] - \nabla\bar{p} + \bar{\rho}\tilde{g} - \nabla \cdot (\bar{\rho}\tau^{SGS}) \quad (4.8)$$

The unclosed stress term $\tau^{SGS} = \widetilde{\vec{u}\vec{u}} - \vec{u}\vec{u}$ appears in these equations due to the spatial filtering and requires a closure model.

Continuity Equation

The LES continuity equation is derived by filtering (2.3). No unclosed terms arise by this filtering operation.

$$\frac{\partial \bar{\rho}}{\partial t} + \nabla \cdot (\bar{\rho} \vec{u}) = 0 \quad (4.9)$$

Species Mass Equation

After applying the LES filter to (2.7), they read:

$$\frac{\partial(\bar{\rho}\tilde{Y}_i)}{\partial t} + \nabla \cdot (\bar{\rho}\tilde{Y}_i\vec{u}) = \nabla \cdot (\bar{\rho}D_i\nabla\tilde{Y}_i) + \bar{\omega}_i - \nabla \cdot (\bar{\rho}\vec{F}_i^{SGS}) \quad (4.10)$$

Again, due to the filtering of the nonlinear convection term, an unclosed flux term $\vec{F}_i^{SGS} = \widetilde{Y_i\vec{u}} - \tilde{Y}_i\vec{u}$ appears for which a closure model is required. Additionally, the source term appears spatially filtered in (4.10). Modelling of the filter operation on this source term is the big challenge in combustion simulation and is subsequently discussed in section 4.3.5.

4.3.3. Numerical Requirements for the Large-Eddy Simulation

The aim of Large-Eddy Simulation is to resolve as much of the turbulent structures as possible on a numerical grid. This can only be achieved if numerical diffusion is reduced to a minimum and energy conservation is assured. Of special importance is the choice of the discretization scheme of the convective term in the momentum and scalar equations. Upwind discretization is much too diffusive and second-order accurate central differencing is commonly used.

For the transport equations of strictly bounded scalars, TVD-schemes have been developed. They are a blend of the upwind and central difference scheme depending on the scalar gradient. The accuracy is somewhere between these two schemes, while boundedness can be ensured.

For the temporal discretization, implicit and explicit time integration may be used. While explicit time integration results in stability limit for the time step, the size of implicit time steps may be chosen accordingly to the desired accuracy. In the framework of LES, the finite time step introduces a temporal filter like the grid does in space. The time step may thus not be chosen significantly larger than the time step for explicit methods. Therefore, explicit time integration is common for LES.

4.3.4. Closure Models for the Large-Eddy Simulation

Turbulent Stresses

A classification of the models for subgrid scale stresses into structural and functional is possible ([76]). The goal of structural modelling is to predict the components of the SGS stress tensor as accurate as possible whereas functional modelling tries to mimic the right effect of the SGS stresses but not necessarily the SGS stress tensor itself.

The effect is primarily to dissipate energy from the resolved scales. Because of that, an obvious functional approach is to introduce a so called turbulent viscosity. The anisotropic part of the SGS stress tensor is then modelled according to the viscous term of the Navier-Stokes Equations.

$$\tau^{SGS,a} = \tau^{SGS} - \frac{1}{3}\text{tr}(\tau^{SGS})\bar{\mathbf{S}} = -2\nu_t\bar{\mathbf{S}} = -\nu_t[\nabla\vec{u} + (\nabla\vec{u})^T] \quad (4.11)$$

The turbulent viscosity causes an energy drain from the resolved scales, as it would be expected from a flow with a Kolmogorov type spectrum. The turbulent viscosity can be orders magnitudes larger than the molecular viscosity, its magnitude is dependent on the flow problem, however.

The introduction of a turbulent viscosity makes the practical implementation of a turbulence model quite easy, it can be simply added to the molecular viscosity. In incompressible flows, the isotropic part of the SGS stress tensor is added to the pressure and does not need to be modelled. No further terms need to be discretized.

Turbulent Fluxes

A functional modelling of the unclosed SGS flux analog to the eddy viscosity approach is the eddy diffusivity approach. Again, the SGS term is modelled analog to the molecular term which is usually sufficiently described by Fick's law. The SGS model then reads:

$$\vec{F}_i^{SGS} = -D_i \nabla \tilde{Y}_i \quad (4.12)$$

The D_i are the turbulent diffusion coefficients. They can be computed by a separate diffusion model but they are often simply related to the turbulent viscosity by a so-called turbulent Schmidt number Sc_t :

$$D_i = \frac{\nu}{Sc_t} \quad (4.13)$$

The turbulent Schmidt number is chosen empirically.

4.3.5. Combustion Models for LES

As already mentioned in section 4.3.2, due to the LES filtering, a closure problem arises in the species mass transport equations. Apart from the turbulent fluxes, the filtered chemical source term has to be known in these equations. Closure of this source term is the task of combustion models. Since this work deals with premixed combustion, in the following, the focus is on models for this regime.

Probability Density Function Models

The source term is usually characterized by a strong nonlinear dependence on temperature and species concentrations, see equation (3.3). That makes it impossible to calculate the source term by simply inserting the filtering quantities, the error would be to large.

Equation (3.3) could be computed exactly, if the PDF of all quantities, that (3.3) depends

on, would be available. The source term in (4.10) then could be written as:

$$\begin{aligned} \bar{\dot{\omega}}_i = & \int_0^\infty \int_0^\infty \dots \int_0^\infty \int_0^\infty \frac{M_i}{\rho} \sum_{j=1}^{n_r} -k_{fj}(T)(\nu_{ij}^- - \nu_{ij}^+) \prod_{i=1}^{n_s} c_i^{\nu_{ij}^+} \\ & \times P(c_1, c_2, \dots, c_n, T) dc_1 dc_2 \dots dc_n dT \quad (4.14) \end{aligned}$$

where $P(c_1, c_2, \dots, c_n, T)$ is the joint probability density function of all concentrations and the temperature. It remains now to determine this joint PDF. Two general approaches are possible, which will be subsequently discussed:

- Transported PDF methods
- Presumed-PDF methods

It should be noted that in LES context, the PDF of SGS quantities is also commonly referred to as “filtered density function” or FDF.

Transported PDF Methods One method to determine the joint PDF is to derive a balance equation, see e.g. [71]. There are different ways to derive the balance equation. One possible approach is to start from the definition of the PDF as an average over Delta functions

$$\bar{\rho} \tilde{P}(\vec{\psi}) = \rho(\vec{\psi}) \overline{\prod_{i=1}^{n_s} \delta(Y_i - \psi_i)} \quad (4.15)$$

The derivation is out of scope here, but the result is

$$\frac{\partial(\bar{\rho} \tilde{P})}{\partial t} + \nabla \cdot (\bar{\rho} \tilde{u} \tilde{P}) + \frac{\partial}{\partial \psi_i} (\dot{\omega}_i \tilde{P}) = \underbrace{\frac{\partial}{\partial \psi_i} \left[-\nabla \cdot (D_i \nabla Y_i) | \vec{\psi} \tilde{P} \right]}_I - \underbrace{\nabla \cdot \left[\bar{\rho} \tilde{u}'' | \vec{\psi} \tilde{P} \right]}_{II} \quad (4.16)$$

The terms on the left hand side represent the rate of change of \tilde{P} in time and due to convection and chemical reaction and are in closed form. Especially the effect of chemical reactions appears closed which is the most attractive feature of the transported-PDF method. The terms on the right hand side of (4.16) contain expectations that are unknown and need to be modelled. The term I describes the molecular diffusion. The other term II describes the turbulent convective transport. The latter term is often

modelled by a gradient-diffusion approach:

$$\overline{\rho \vec{u}'' | \vec{\psi}} \tilde{P} = -D_T \nabla \tilde{P} \quad (4.17)$$

while stochastic mixing models account for the diffusion term.

It is worth to note that term II can be closed by extending the joint scalar PDF to a joint velocity-scalar PDF. But, more terms appear in the PDF equation that need to be modelled as well.

The diffusion term is unclosed, because the PDF describes one-point statistics only and contains no information on length scales. To overcome this, further extensions have been proposed, e.g. solution of a joint PDF of velocity, viscous dissipation and scalars [72] or solution of the joint statistics of velocity, velocity gradients, scalars and scalar gradients [22].

The numerical solution of 4.16 is expensive because of the high dimensionality of the PDF equation. For Finite-Volume or Finite-Element based solution techniques, the memory requirement increases exponentially with dimensionality. Almost all implementations therefore apply Monte-Carlo methods for the solution of the PDF equation. The memory requirements then only depend linearly on the dimensionality.

In Monte-Carlo simulations a number of stochastic particles are tracked which may be regarded of as realizations of the PDF. The histogram of the particles properties in a cell then recovers the PDF. It is easy imaginable that the number of particles has to be large (e.g. a multiple of 10 per cell) to enable a proper statistics. This may still be attractive for two-dimensional RANS calculations but gets very expensive for e.g. LES which always has to be performed on three-dimensional domains.

Presumed PDF Methods The expensive solution of the PDF balance equation can be avoided by assuming a specific shape for the PDF. Thus, the structure of the PDF is given by some empirical function which still contains a small number of freely selectable parameters. These parameters are then determined from the moments of the stochastic variables for which transport equations have to be solved. Although the influence of chemical reactions on the PDF shape cannot be accounted for on a physical basis as it is the case with a PDF balance equation, the method is attractive because of its much lower computational effort.

4. Numerical Methods for Computational Fluid Dynamics

While it is relatively simple to find shape functions for one-dimensional PDF's, it becomes very difficult to presume multi-dimensional joint-PDF's. A common practice is therefore to assume a statistical independence between the parameters of the PDF and to apply one-dimensional functions for each of them:

$$P(Y_1, Y_2, \dots, Y_{n_s}) = P(Y_1) \cdot P(Y_2) \cdot \dots \cdot P(Y_{n_s}) \quad (4.18)$$

The influence of the PDF shape on the results was found to be small when the circumstances are favorable, i.e. the reaction rates are high. In contrast, the results become strongly dependent on the PDF shape e.g. for nitric oxide formation which is very sensitive to the temperature.

Different mathematical functions are used to presume the PDF shape in combustion theory. A common choice to approximate the PDF of stochastic variables, when the underlying mechanism is largely unknown is the Gaussian distribution. That is because due to the central limit theorem, the sum of a large number of independent stochastic variables converges towards a normal distribution. It is also known from measurements, that mixing of passive scalars is well described by the normal distribution [30]. Because the scalars, that need to be described in combustion theory are bounded and the domain of the Gaussian distribution is infinite, it cannot be used directly. To describe bounded scalars, the Gaussian distribution is clipped at the boundaries and Dirac deltas are added to ensure the normalization constraints. The PDF for a scalar bound between 0 and 1 is then given by

$$P_G(x) = \frac{1}{\sigma\sqrt{2\pi}} \exp\left[-\frac{(x-\mu)^2}{2\sigma^2}\right] [H(x) - H(x-1)] + A\delta(x) + B\delta(x-1) \quad (4.19)$$

The coefficient A and B represent the clipped part of the normal distribution:

$$A = \int_{-\infty}^0 \frac{1}{\sigma\sqrt{2\pi}} \exp\left[-\frac{(x-\mu)^2}{2\sigma^2}\right] dx \quad (4.20)$$

$$B = \int_1^{\infty} \frac{1}{\sigma\sqrt{2\pi}} \exp\left[-\frac{(x-\mu)^2}{2\sigma^2}\right] dx \quad (4.21)$$

The mean value of this distribution is μ . While for the Gaussian distribution the variance is algebraically related to σ this is not the case for the clipped Gaussian distribution.

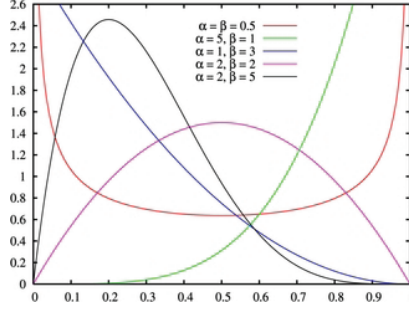


Figure 4.1.: Possible shapes of the beta function for different values of the parameters p and q

Here, the variance is nonlinearly related to σ and has to be evaluated numerically.

Another very commonly used function is the beta function. It is defined as

$$P_{\beta}(x) = \frac{\Gamma(p+q)}{\Gamma(p)\Gamma(q)} x^{p-1}(1-x)^{q-1} \quad (4.22)$$

where $\Gamma(x)$ is the Gamma function and p and q are some free parameters of the distribution, that are related to the first and second moment of the PDF:

$$\bar{x} = \int_0^1 xP(x) dx = \frac{p}{p+q} \quad \overline{x^2} = \int_0^1 x^2P(x) dx = \frac{p(1+p)}{(p+q)(1+p+q)} \quad (4.23)$$

The domain of the beta function is $x \in [0, 1]$. The beta PDF is attractive because it is able to reproduce the bimodal limit for the maximum variance where it turns into two delta-peaks at $x = 0$ and $x = 1$. When the variance becomes zero, the beta function turns into a single Dirac delta at the mean value. For low variance, the beta PDF turns into a Gaussian PDF. All moments up to the fourth moment of both PDF then may be equal [33]. See figure 4.1 for plots of different possible beta function shapes.

Artificially Thickened Flame Model

Since usual computational meshes are not able to resolve the flame structure properly, one possible approach is to artificially thicken the flame and make it resolvable, while keeping the flame speed constant. This can be achieved by modifying the diffusivity.

From fundamental theories, it follows for a one step reaction:

$$s_L^0 \propto \sqrt{D\dot{\omega}} \quad \delta_L^0 \propto \frac{D}{s_L^0} \quad (4.24)$$

with the laminar flame speed s_L^0 and the laminar flame thickness δ_L^0 , D is the diffusion coefficient. From the above, it is obvious, that the thickening by a factor F can be achieved by increasing the diffusivity by F to $\bar{D} = FD$ and dividing the reaction source term by F to $\bar{\omega} = \dot{\omega}/F$. Thus, the modified expressions become:

$$\bar{s}_L^0 \propto \sqrt{FD\frac{\dot{\omega}}{F}} = s_L^0 \quad \bar{\delta}_L^0 \propto \frac{FD}{\bar{s}_L^0} = \frac{FD}{s_L^0} = F\delta_L^0 \quad (4.25)$$

Unfortunately, although the laminar flame speed keeps constant, the interaction between turbulent vortices and the flame cannot be captured by the thickened flame approach. The effect of turbulent vortices is to wrinkle the flame and enhance the laminar flame speed to a higher turbulent flame speed. This interaction is of course altered, when the flame thickness changes.

To correct the influence of turbulence on the flame, a so called efficiency function E is introduced. The diffusivity \bar{D} and source term $\bar{\omega}$ are both multiplied by E .

Models Based on Geometrical Flame Descriptions

If the flame thickness is thin compared to the size of the turbulent vortices, the reactive layer is unaffected by turbulence and the interaction between turbulence and chemistry is purely kinematic, i.e. the flame is a thin surface that is wrinkled by the turbulent eddies but its structure across the thickness is the same as for the laminar flame sheet. It is possible to derive combustion models that describe the relevant geometric properties of the flame front. Because they are limited to the flamelet regime, they are called flamelet models.

G-Equation A method that is able to describe the temporal evolution of surfaces with arbitrary complexity in space is the level-set method. It is not specific to combustion modeling and is also used e.g. in computer graphics or for free surface flows. The base of this method is a scalar field. The surface under consideration is defined as an isosurface of this field. The level-set method has been applied to combustion modeling e.g. by

Peters [66]. In the context of combustion modeling, the scalar field is usually denoted by G . That is why the method is referred to as G-equation method. Apart from its isosurface, the scalar field has no physical meaning. To guarantee uniqueness, the scalar field is usually normalized to a signed distance function

$$\|\nabla G\| = 1 \quad (4.26)$$

The evolution of the level set is governed by a convection equation:

$$\frac{\partial G}{\partial t} + \vec{u} \cdot \nabla G = s_F \|\nabla G\| \quad (4.27)$$

where s_F is the propagation velocity of the flame front into the fresh gas.

Combustion modeling with the level set method is not based on solving the species mass fraction equations (2.7). Instead, the flame is treated as a geometric entity, i.e. a surface which is convected by the flow and self-propagating normal to itself with its flame speed. For computing the flame speed, correlation equations are used. Thus, no closure of the chemical source term is required since its effect is included in the flame speed.

For LES of turbulent combustion, the above equation needs to be filtered. Different modeling approaches for this task can be found in the literature. The one of Pitsch et al. [68] is similar to the RANS version of Peters:

$$\bar{\rho} \frac{\partial \tilde{G}}{\partial t} + \bar{\rho} \tilde{\vec{u}} \cdot \nabla G = \bar{\rho} (\tilde{s}_T - D_{GT} \tilde{\kappa}) \|\nabla \tilde{G}\| \quad (4.28)$$

Additional models for the turbulent flame speed s_T and the so-called “scalar turbulent diffusivity” are also required.

Although the G-equation approach is an elegant description of the flame front geometry, the solution of (4.28) is numerically expensive and difficult to implement because the G field is discontinuous due to (4.26). Special discretization schemes are required and a frequent reinitialization of the scalar field.

Another difficulty is the coupling of the artificial quantity G with the mass and energy equations such that their conservation properties are preserved.

Flame Surface Density This class of combustion models is formulated for the special case of one-step chemistry, i.e. the chemical system is controlled by only one single irreversible reaction. By choosing a suitable normalization of the involved species mass fractions, the equation (4.10) can be replaced by a single transport equation of a progress variable c for which holds $c = 0$ in the unburnt region and $c = 1$ in the fully burnt gas:

$$\frac{\partial \bar{\rho} \tilde{c}}{\partial t} + \nabla \cdot (\bar{\rho} \tilde{c} \tilde{u}) = \overline{\nabla \cdot (\rho D \nabla c)} + \bar{\omega} - \vec{F}_c^{SGS} \quad (4.29)$$

The source term together with the diffusion term can be expressed as:

$$\overline{\nabla \cdot (\rho D \nabla c)} + \bar{\omega} = \overline{\rho w \|\nabla c\|} \quad (4.30)$$

This can be related to geometric properties of the flame front. It is therefore useful to define a flame surface averaging $\overline{(\dots)}_s$ of some quantity ϕ :

$$\overline{(\phi)}_s = \overline{\phi \delta(c - c^*) \|\nabla c\|} / \Sigma \quad (4.31)$$

with the so-called flame surface density Σ :

$$\Sigma = \overline{\delta(c - c^*) \|\nabla c\|} \quad (4.32)$$

The meaning of this quantity is the flame surface area per unit volume. It increases with more intense wrinkling of the flame surface.

With the above defined averaging operation, the source can be written as

$$\overline{\rho w \|\nabla c\|} = \int_0^1 \overline{(\rho w)}_s \Sigma \, dc^* \quad (4.33)$$

If the flame is thin, the isosurfaces for all values of c^* can be considered parallel. The latter equation then becomes:

$$\int_0^1 \overline{(\rho w)}_s \Sigma \, dc^* \approx \overline{(\rho w)}_s \Sigma \approx \rho_u s_L \Sigma \quad (4.34)$$

To close (4.29), it remains to determine Σ . Different modeling approaches exist for this purpose. Among numerous different algebraic models can be chosen, see e.g. [13] for an

extensive overview. It also possible to derive a transport equation for the flame surface density. This has been done e.g. by Hawkes et al. [40]. This equation contains different contributions which are not closed and have to be modeled.

Flame Surface Wrinkling An alternative to the flame surface density is the flame surface wrinkling factor Ξ . It can be interpreted as the ratio of the turbulent flame surface to the flame surface projected in the propagation direction. It is also related to the flame surface density:

$$\Xi = \frac{\Sigma}{\|\nabla \bar{c}\|} \quad (4.35)$$

Thus the same algebraic models as for the flame surface density can be used. Weller et al. [87, 88] have derived a transport equation for the flame surface wrinkling. This equation is generally more complex and modeling the unclosed terms is more difficult than for the flame surface density equation.

Part II.

Applications

5. Implementation of the Presumed PDF Model into the CFD Code

The presumed-PDF method together with chemistry tables generated from flamelet generated manifolds have been implemented into the open source PDE package OpenFOAM® [65, 64, 86]. A description of the key features of this implementation is given in the current chapter.

The basis for the presumed-PDF/ILDM model is the combustion progress variable Y that defines the local position on the low-dimensional manifold. The progress variable is a selected mass fraction in all subsequent calculations. The LES transport equation for the filtered combustion progress variable is identical to the species mass fraction equation (4.10):

$$\frac{\partial(\bar{\rho}\tilde{Y})}{\partial t} + \nabla \cdot (\bar{\rho}\tilde{Y}\tilde{\mathbf{u}}) = \nabla \cdot (\bar{\rho}D\nabla\tilde{Y}) + \bar{\omega} - \nabla \cdot (\bar{\rho}\vec{F}_Y^{SGS}) \quad (5.1)$$

The unresolved turbulent fluxes \vec{F}_Y^{SGS} are modelled by a gradient diffusion ansatz (4.12). Although counter gradient diffusion occurs especially in premixed combustion this is not incorporated here. That is mainly because no proper models are available for counter gradient diffusion. Its modelling would require a turbulent flux model of higher order, i.e. solution of three transport equations for the vector quantity \vec{F}_Y^{SGS} . This would introduce new closure models and sources of errors. Despite this, the error in neglecting counter gradient diffusion in \vec{F}_Y^{SGS} is bounded by the fact that it is at least partially resolved in LES through the resolved turbulent motion, even when gradient diffusion SGS models are used [70].

Further transport equations are solved if the chemistry table contains the mixture fraction or the enthalpy as coordinates. The mixture fraction is a passive scalar and the

5. Implementation of the Presumed PDF Model into the CFD Code

equation therefore does not contain a source term:

$$\frac{\partial(\bar{\rho}\tilde{Z})}{\partial t} + \nabla \cdot (\bar{\rho}\tilde{Z}\tilde{u}) = \nabla \cdot (\bar{\rho}D\nabla\tilde{Z}) - \nabla \cdot (\bar{\rho}\vec{F}_Z^{SGS}) \quad (5.2)$$

The unresolved turbulent fluxes \vec{F}_Z^{SGS} are again modelled by the gradient diffusion ansatz (4.12).

In a variable enthalpy problem, the following enthalpy equation is solved:

$$\frac{\partial(\bar{\rho}\tilde{h})}{\partial t} + \nabla \cdot (\bar{\rho}\tilde{h}\tilde{u}) = \nabla \cdot (\bar{\rho}\alpha\nabla\tilde{h}) - \nabla \cdot (\bar{\rho}\vec{F}_h^{SGS}) \quad (5.3)$$

with $\vec{F}_h^{SGS} = -\alpha_t\nabla\tilde{h}$. Frictional heating has been neglected and pressure is considered constant.

The filtered mixture properties, i.e. $\bar{\rho}$, $\bar{\omega}$ etc., are determined by the presumed PDF's. This will be demonstrated for the reaction rate and is analogous for all other quantities. The filtered quantity is determined after integration over the PDF's:

$$\bar{\omega} = \int \int \omega(Y, Z) P_Y(\tilde{Y}, \tilde{Y}^2, Y) P_Z(\tilde{Z}, \tilde{Z}^2, Z) dY dZ = \bar{\omega}(\tilde{Y}, \tilde{Y}^2, \tilde{Z}, \tilde{Z}^2) \quad (5.4)$$

The filtered quantity depends on the mean progress variable \tilde{Y} and the mean mixture fraction \tilde{Z} as well as on their second moments¹. These can be solved for by a number of different alternatives. Some options are reviewed in section 5.5. The PDF integration could be done for every cell and time instant during the solver run but this turned out to be too time consuming. It was faster to perform the PDF integration before the solver run and store the integrated quantities in a lookup table.

In summary, all steps of the presumed-PDF solver are sketched in figure 5.1. In the remainder of the current chapter, most of the steps will be discussed in more detail. Before the actual solver run, a lookup table of the thermochemical quantities will be created. The storage and retrieval technique is described in section 5.2. It involves the numerical integration of ILDM tables over PDF functions. The creation of the chemistry tables is described in section 5.3. More details on the numerical integration is given in section 5.4.

¹In a homogeneous premixed system, the PDF P_Z is dropped and $\bar{\omega}$ depends on Y only: $\bar{\omega}(\tilde{Y}, \tilde{Y}^2)$

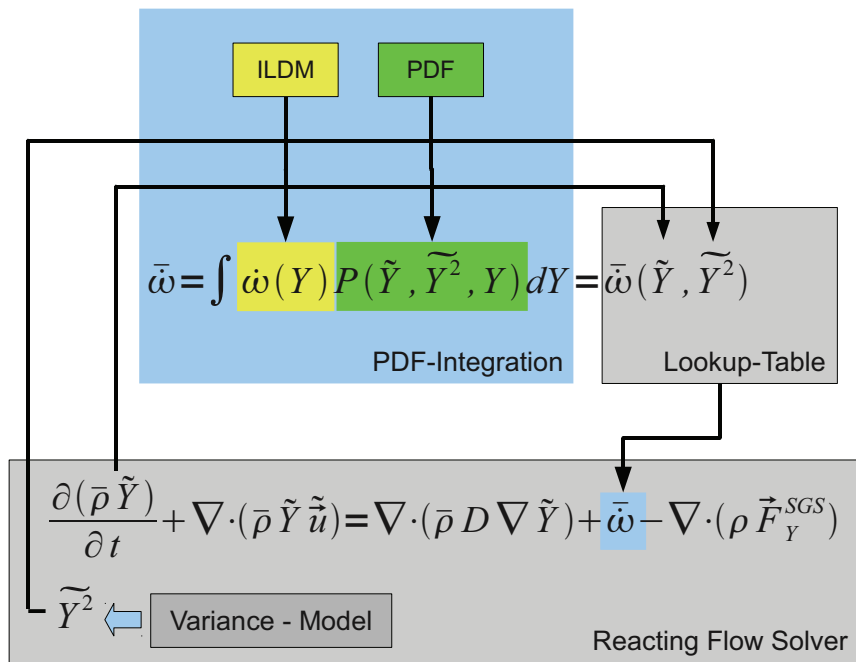


Figure 5.1.: Sketch of the algorithm structure of the presumed-PDF solver

5.1. Density Weighting of the PDF

It is possible to either presume the density-weighted PDF $\tilde{P}(x)$ or the un-weighted PDF $P(x)$ with the precedingly described mathematical functions. The mean of some depending thermophysical property $\phi(x)$ is then defined by

$$\bar{\phi} = \int \phi(x)P(x) dx = \bar{\rho} \int \frac{\phi(x)}{\rho} \tilde{P}(x) dx \quad (5.5)$$

$$\tilde{\phi} = \frac{1}{\bar{\rho}} \int \rho \phi(x)P(x) dx = \int \phi(x) \tilde{P}(x) dx \quad (5.6)$$

As described in section 4.3.1, in numerical simulations of variable-density flows, usually the Favre filtered values $\tilde{\phi}$ are required. Also, the shape of the PDF is determined by the first and second moment of the defining quantity:

$$\bar{x} = \int xP(x) dx = \bar{\rho} \int \frac{x}{\rho} \tilde{P}(x) dx \quad (5.7)$$

$$\overline{x^2} = \int x^2P(x) dx = \bar{\rho} \int \frac{x^2}{\rho} \tilde{P}(x) dx \quad (5.8)$$

$$\tilde{x} = \frac{1}{\bar{\rho}} \int \rho xP(x) dx = \int x \tilde{P}(x) dx \quad (5.9)$$

$$\tilde{x^2} = \frac{1}{\bar{\rho}} \int \rho x^2P(x) dx = \int x^2 \tilde{P}(x) dx \quad (5.10)$$

Again, in variable-density simulations, the methods from section 5.5 yield Favre-filtered second moments $\tilde{x^2}$. According to [92], there is no essential difference between the usage of density-weighted or un-weighted PDF, provided that the coefficients of the PDF function are determined in a consistent manner using relations (5.9) and (5.10). In the current work, the density-weighted PDF $\tilde{P}(x)$ is presumed, because of its easier implementation and lower computational overhead during PDF integration.

5.2. Chemistry and Lookup Table Storage and Retrieval

For the chemistry table and the pre-integrated lookup table, storage of multidimensional lookup tables is required. The most important requirements for the implementation are

low memory consumption, accurate and quick lookup. While memory of a computer can be extended, time cannot be bought. Therefore, the emphasis is on the last point.

A number of techniques for table storage have been proposed, e.g. in-situ adaptive tabulation [73]. Polynomial fits are also found in a number of works [81, 11]. Even neural networks have been used [18]. Thereby, especially tabulation methods that enable a local refinement of the tabulation resolution require searching operations when performing a table lookup, which is expensive. In the current implementation, a structured table with no possibility for local refinements was used. The tabulation resolution was constant for each dimension. That allowed for direct computation of the table cell indices instead of searching for them.

During a table lookup, the indices of tabulated points around the lookup point are identified first. After that, a multidimensional linear interpolation is performed to interpolate the values at the wanted point. Although e.g. spline interpolation methods have higher order interpolation errors, the current method is very easy to implement for arbitrary high dimensional tables and the lower interpolation order can be compensated by using a higher table resolution.

5.3. Chemistry Table Generation

The chemistry table is generated by the Flamelet Generated Manifolds (FGM) method (see section 3.2.5), because of its easy implementation. The flamelets have been computed using CANTERA [35] and stored in a database. As progress variable, the mass fraction of a selected species, in all subsequent calculations the mass fraction of CO_2 , was used.

For a homogeneously premixed, adiabatic flow, a single flamelet computation is sufficient to generate the data for the chemistry table. When partially premixed computations were performed, the mixture fraction had to be added as an additional coordinate to the chemistry table. Then, a specified number of flamelets with different mixture fractions had to be computed. Similarly, when heat losses had to be accounted for, the enthalpy was used as an additional coordinate. Then, a number of flamelets with different initial temperatures were computed.

For states with too lean mixtures, where the flamelet calculation does not converge any more, thermochemical properties had to be included in the table as well. These states were computed by interpolating between the leanest successfully computed flamelet and pure air.

Similar problems occur, when the enthalpy is varied. Changing the initial temperature in the flamelet calculation works well for high enthalpies for which the initial temperature in the flamelet calculation is roughly above the room temperature. For lower enthalpies, the initial temperature drops quickly below room temperature, which restrains the flamelet computation from converging. When the exhaust gases are extremely cooled, e.g. down to room temperature, flamelet calculations with even negative initial temperatures would be required. To circumvent this problem, a different initial mixture is used in the flamelet computations, when initial temperature would drop below some limit, e.g. $T_0 < 280K$. A part of the educts is then converted into products in a way that the mixture fraction remains unchanged. This raises the enthalpy of the mixture at a constant temperature.

5.4. PDF Integration

Integration of PDF functions requires some care, because PDF functions naturally develop peaks at certain values of the variance. Only few publications are available on this topic. The integration algorithm of Burgeth [8] requires to approximate the function to integrate into a polynomial. Also, Lentini [52] proposes an integration method for the beta PDF that is computationally very efficient but requires to cast the integrand into a special form to make use of some relationships between the beta and gamma function. This cast is only possible for the density as function of the mixture fraction in non-premixed combustion but not for other quantities like species mass fractions [55].

Since tabulated quantities should be integrated in the current work, no such limitations could be accepted. Also integration of products of PDF's was required as well as possible interchanging of the PDF functions. Therefore, analytical simplifications were difficult to apply and numerical integration was desired.

To treat the singularities, a combination of numerical integration and analytical simplifications was used. Each PDF was represented as a sum of a smooth function and a

5. Implementation of the Presumed PDF Model into the CFD Code

number of Dirac deltas

$$P(x) = p(x) + \sum_{i=0}^{N_P} \alpha_{P_i} \delta(x - x_{\delta_i}) \quad (5.11)$$

When products of PDF's are integrated, the integral may be split into a number of smooth integrals:

$$\begin{aligned} \int_0^1 \int_0^1 f(x, y) P(x) G(y) dx dy &= \int_0^1 \int_0^1 f(x, y) p(x) g(y) dx dy \\ &+ \sum_{j=0}^{N_G} \alpha_{G_j} \int_0^1 f(x, y_{\delta_j}) dx + \sum_{i=0}^{N_P} \alpha_{P_i} \int_0^1 f(x_{\delta_i}, y) dy \\ &+ \sum_{j=0}^{N_G} \sum_{i=0}^{N_P} \alpha_{P_i} \alpha_{G_j} f(x_{\delta_i}, x_{\delta_j}) \end{aligned} \quad (5.12)$$

where $G(y)$ is another PDF in the form of (5.11). This splitting of the integrals is also analogically possible for higher dimensional integrals. The integration of the smooth integrals has been carried out numerically using the GNU Scientific Library [27] for one-dimensional integrals and the CUBA library [37] for multi-dimensional integrals.

To create the representation (5.11) for a beta-PDF, the methodology from [55, 3] has been used. To avoid the singularities at the domain boundary of the beta-PDF, they rewrite the PDF integral as

$$\begin{aligned} \int_0^1 f(x) P_\beta(x) dx &= \\ &\int_0^\varepsilon f(x) P_\beta(x) dx + \int_\varepsilon^{1-\varepsilon} f(x) P_\beta(x) dx + \int_{1-\varepsilon}^1 f(x) P_\beta(x) dx \\ &\approx f(0) \frac{\varepsilon^p}{p} \frac{\Gamma(p+q)}{\Gamma(p)\Gamma(q)} + \int_\varepsilon^{1-\varepsilon} f(x) P_\beta(x) dx + f(1) \frac{\varepsilon^q}{q} \frac{\Gamma(p+q)}{\Gamma(p)\Gamma(q)} \end{aligned} \quad (5.13)$$

where p and q are the shape parameters of the beta-PDF in (4.22). The approximation is that $f(x) \approx f(0)$ within $x \in (0, \varepsilon)$ and $f(x) \approx f(1)$ within $x \in (1 - \varepsilon, 1)$. To integrate

that into the framework described above, the PDF is rewritten as

$$P_{\beta}^*(x) = \frac{\varepsilon^p \Gamma(p+q)}{p \Gamma(p)\Gamma(q)} \delta(x) + P_{\beta}(x)H(x-\varepsilon)H(x-1+\varepsilon) + \frac{\varepsilon^q \Gamma(p+q)}{q \Gamma(p)\Gamma(q)} \delta(x-1) \quad (5.14)$$

5.5. Methods for Determination of the Scalar Variance

Naturally, the scalar variance would be defined as the fluctuation of the scalar quantity ϕ around the filtered value

$$\phi_v = \overline{\phi'^2} = \overline{(\phi - \bar{\phi})^2} \quad (5.15)$$

However, practical computations have shown, that it is more appropriate to define the scalar variance as

$$\phi_v = \overline{\phi^2} - \bar{\phi}^2 \quad (5.16)$$

This includes the assumption, that $\bar{\bar{\phi}} = \bar{\phi}$, which is strictly not true for common LES filters. But it can be shown, that (5.16) is obtained if the variance is defined in terms of a filtered probability density function [45]. The filtered probability density function or large-eddy PDF was first introduced by Pope [71] without being so named, a more recent discussion is given by Gao and O'Brien [29]. The definition of the FPDF takes into account the LES filter kernel and the fine-grain spatial distribution of the quantity $\phi(\vec{x})$:

$$\bar{P}(\phi', \vec{x}) = \int_{-\infty}^{\infty} G(\vec{x}, \vec{x}') \delta(\phi' - \phi(\vec{x}')) d\vec{x}' \quad (5.17)$$

The mean value of the FPDF is thus the filtered quantity:

$$\overline{\phi(\vec{x})} = \int \phi' \bar{P}(\phi', \vec{x}) d\phi' = \int \phi(\vec{x}') G(\vec{x}, \vec{x}') d\vec{x}' \quad (5.18)$$

And the variance may be expressed as:

$$\int [\phi' - \bar{\phi}(\vec{x})]^2 \bar{P}(\phi', \vec{x}) d\phi' = \iint [\phi' - \bar{\phi}(\vec{x})]^2 G(\vec{x}, \vec{x}') \delta(\phi' - \phi(\vec{x}')) d\vec{x}' d\phi' \quad (5.19)$$

$$= \int [\phi(\vec{x}') - \bar{\phi}(\vec{x})]^2 G(\vec{x}, \vec{x}') d\vec{x}' \quad (5.20)$$

$$= \int [\phi^2(\vec{x}') + \bar{\phi}^2(\vec{x}) - 2\phi(\vec{x}')\bar{\phi}(\vec{x})] G(\vec{x}, \vec{x}') d\vec{x}' \quad (5.21)$$

$$= \overline{[\phi^2(\vec{x}) + \bar{\phi}^2(\vec{x}) - 2\bar{\phi}(\vec{x})\bar{\phi}(\vec{x})]} \quad (5.22)$$

$$= \overline{\phi^2(\vec{x})} - \overline{\phi(\vec{x})}^2 \quad (5.23)$$

$$(5.24)$$

Furthermore, (5.15) can not be related to a one point PDF, because it contains spatial correlations of ϕ . The latter definition (5.16) is commonly used in the LES context.

Several methods exist to determine the scalar variance. In the current case, it has to be taken into account, that the scalar is not passive but reacting.

All the methods described below have been implemented in the CFD code. For all of the subsequently presented computations, the variance was computed using the transport equation approach.

5.5.1. Transport Equation

A scalar quantity transport equation in the general form reads:

$$\frac{\partial \rho \phi}{\partial t} + \nabla \cdot (\rho \vec{u} \phi) = \nabla \cdot (\rho D_\phi \nabla \phi) + \dot{\omega}_\phi \quad (5.25)$$

After filtering, the unclosed SGS fluxes F^{SGS} appear:

$$\frac{\partial \bar{\rho} \tilde{\phi}}{\partial t} + \nabla \cdot (\bar{\rho} \tilde{\vec{u}} \tilde{\phi}) = \nabla \cdot (\bar{\rho} D_\phi \nabla \tilde{\phi}) + \bar{\omega}_\phi - \nabla \cdot F_\phi^{SGS} \quad (5.26)$$

From (5.25) a transport equation for $\tilde{\phi}^2$ can be obtained

$$\frac{\partial \bar{\rho} \tilde{\phi}^2}{\partial t} + \nabla \cdot (\bar{\rho} \tilde{\vec{u}} \tilde{\phi}^2) = \nabla \cdot (\bar{\rho} D_\phi \nabla \tilde{\phi}^2) - 2\bar{\rho} \tilde{\chi}_\phi + 2\bar{\rho} \widetilde{\dot{\omega}_\phi \phi} - \nabla \cdot F_{\phi^2}^{SGS} \quad (5.27)$$

5. Implementation of the Presumed PDF Model into the CFD Code

where $\bar{\rho}\tilde{\chi}_\phi$ is the scalar dissipation rate. It can be decomposed into a resolved and an unresolved SGS part χ_ϕ^{SGS} :

$$\bar{\rho}\tilde{\chi}_\phi = \overline{\rho D_\phi |\nabla\phi|^2} = \bar{\rho}D_\phi |\nabla\tilde{\phi}|^2 + \chi_\phi^{SGS} \quad (5.28)$$

Furthermore, an equation for $(\tilde{\phi})^2$ is needed. It can be derived from (5.26) and reads

$$\begin{aligned} \frac{\partial \bar{\rho} (\tilde{\phi})^2}{\partial t} + \nabla \cdot \left[\bar{\rho} \tilde{u} (\tilde{\phi})^2 \right] &= \nabla \cdot \left[\bar{\rho} D_\phi \nabla (\tilde{\phi})^2 \right] - \nabla \cdot \left(2\tilde{\phi} F_\phi^{SGS} \right) \\ &\quad + 2F_\phi^{SGS} \cdot \nabla \tilde{\phi} - 2\bar{\rho} D_\phi |\nabla \tilde{\phi}|^2 + 2\bar{\rho} \tilde{\omega}_\phi \tilde{\phi} \end{aligned} \quad (5.29)$$

A transport equation for ϕ_v can then be derived by subtracting (5.29) from (5.27):

$$\begin{aligned} \frac{\partial \bar{\rho} \tilde{\phi}_v}{\partial t} + \nabla \cdot \left(\bar{\rho} \tilde{u} \tilde{\phi}_v \right) &= \nabla \cdot \left(\bar{\rho} D \nabla \tilde{\phi}_v \right) - \nabla \cdot F_{\phi_v}^{SGS} - 2F_\phi^{SGS} \cdot \nabla \tilde{\phi} \\ &\quad - 2\chi_\phi^{SGS} + 2\bar{\rho} \left(\widetilde{\omega_\phi \phi} - \tilde{\omega}_\phi \tilde{\phi} \right) \end{aligned} \quad (5.30)$$

Domingo et al. [21] propose not to solve (5.30) directly, but to solve for the deviation from the maximum variance $\sigma = \tilde{\phi}(1 - \tilde{\phi}) - \phi_v$. They argue, that the resulting transport equation does not contain the production source term $-2F_\phi^{SGS} \cdot \nabla \tilde{\phi}$ which is probably inaccurately depicted by the numerical simulation because its modelling involves the gradient of the progress variable which gets steep in premixed combustion.

From a numerical point of view, this is equivalent to solve the transport equation (5.27) for $\tilde{\phi}^2$, because it is linearly related to σ :

$$\sigma = \tilde{\phi}(1 - \tilde{\phi}) - \phi_v = \tilde{\phi} - (\tilde{\phi})^2 - \left[\tilde{\phi}^2 - (\tilde{\phi})^2 \right] = \tilde{\phi} - \tilde{\phi}^2 \quad (5.31)$$

5.5.2. Scale Similarity Assumption

For computing the scalar variance for the mixture fraction in non premixed combustion, Cook and Riley [19] have applied a scale similarity approach. In this approach, the SGS scalar variance is assumed to be proportional to the resolved variance at some test filter level $\hat{\Delta}$

$$\bar{\phi}_v = \bar{\phi}^2 - \bar{\phi}^2 \approx C \left(\widehat{\phi^2} - \hat{\phi}^2 \right) \quad (5.32)$$

where C is some model constant, that has to be chosen appropriately.

This approach has proven successful for determining the variance of a conserved scalar, its success is questionable for reacting scalars, because chemical reactions are dominated by small scales and extrapolation from larger scales is expected to be inaccurate [67]. Domingo et al. [21] have done a-priori tests on this approach and found notable deviation from the DNS data even for carefully adjusted values of C .

5.5.3. Dynamic Procedure

Jaberi et al. proposed a dynamic procedure to compute the chemical source term directly [44]. The source term is a complex nonlinear function of some thermodynamic variable (ϕ is used here) $\dot{\omega} = f(\phi)$. Formally the same numerical procedure can be used to compute the scalar variance of ϕ by putting as the functional expression of f simply the square of its argument: $f(\phi) := \phi^2$. This function is certainly less complex, although still nonlinear.

Jaberi et al. model the filtered function as

$$\bar{f} = \overline{f(\phi)} = f(\bar{\phi}) + \lambda \quad (5.33)$$

where λ is some SGS contribution which is modeled by a scale similarity approach

$$\lambda \approx K \left[\overline{f(\bar{\phi})} - f(\bar{\bar{\phi}}) \right] \quad (5.34)$$

where the constant K is determined by a dynamic procedure based on the Germano Identity [31].

If the function is identified with the second moment of the thermodynamic variable $f(\phi) = \phi^2$, a scale similarity approach is recovered:

$$\overline{f(\phi)} = \overline{\phi^2} = \bar{\phi}^2 + K \left[\overline{\phi^2} - \bar{\phi}^2 \right] \quad (5.35)$$

The dynamic procedure relies on fulfilment of the Germano Identity

$$G = \Lambda - \lambda = \widehat{f(\bar{\phi})} - f(\hat{\phi}) \quad (5.36)$$

where Λ is the residual term at a test filter level

$$\widehat{f(\phi)} = f(\hat{\phi}) + \Lambda \quad (5.37)$$

The equation for computing K then becomes

$$K = \frac{\widehat{(\bar{\phi})}^2 - (\hat{\phi})^2}{(\bar{\phi})^2 - (\hat{\phi})^2} \quad (5.38)$$

5.5.4. Calculation from Flame Surface Density

The flame surface density is defined as the flame area per unit volume

$$\Sigma = \lim_{\delta V \rightarrow 0} \frac{1}{\delta V} \int_{\delta V} dA \quad (5.39)$$

If the combustion progress is described by a single scalar c which is $c = 0$ in the fresh gas and $c = 1$ in the fully burnt gas region, a relation between the combustion progress c and the flame surface density Σ is given by

$$\Sigma(c^*) = \overline{|\nabla c|}_{c=c^*} P(c^*) \quad (5.40)$$

where $\overline{|\nabla c|}_{c=c^*}$ is the conditional mean of the gradient of c at $c = c^*$. Eq. (5.40) gives the density of the isosurface of $c = c^*$. If the flame is in the flamelet regime, i.e. the flame is thin and all isosurfaces of c can be regarded as parallel, a generalized flame surface density may be defined [6]:

$$\bar{\Sigma} = \int_0^1 \overline{|\nabla c|}_{c=c^*} P(c^*) dc^* = \overline{|\nabla c|} \quad (5.41)$$

If the scalar gradient $|\nabla c|(c)$ and the flame surface density were known, then (5.41) could be used to retrieve the scalar variance in the framework of a presumed-PDF method. If the PDF is presumed, then the shape of the PDF $P(c^*)$ is fully determined by the mean

and variance of c :

$$\bar{\Sigma} = \int_0^1 \overline{|\nabla c|}_{c=c^*} P(c^*, \tilde{c}, \tilde{c}_v) dc^* = \overline{|\nabla c|} \quad (5.42)$$

Furthermore, the scalar gradient $|\nabla c|(c)$ can be taken from a flamelet calculation. For the application of presumed-PDF methods, it is common practice to perform the integration over the PDF before the actual flow computation for all possible values of \tilde{c} and \tilde{c}_v . This could be done for (5.42) as well. The mean progress variable \tilde{c} is known from the transport equation and if the value of Σ is known as well, then the variance can be found by searching in the lookup table.

For the calculation of the flame surface density, a large number of algebraic models has been proposed in the past, see e.g. [13] for an overview. Alternatively, transport equations have been derived and could be used [80].

5.6. Summary of Implemented Equations

Although all of the above mentioned methods for the computation of the scalar variance of the controlling variables have been implemented in the CFD code, only the transport equation method has been used for all subsequent calculations. In this section, a brief outline of the resulting algorithm shall be given. The case of one chemical progress variable and variable mixture fraction is described. For cases, where the mixture fraction is a constant, the corresponding transport equations will be omitted and the dimensionality of the lookup tables reduced. Finally, the scalar equations, that had to be solved with the reduced system, are:

$$\frac{\partial(\bar{\rho}\tilde{Y})}{\partial t} + \nabla \cdot (\bar{\rho}\tilde{Y}\tilde{u}) = \nabla \cdot \left[\bar{\rho} \left(D + \frac{\mu_t}{Sc_t} \right) \nabla \tilde{Y} \right] + \bar{\omega} \quad (5.43)$$

$$\frac{\partial(\bar{\rho}\tilde{Z})}{\partial t} + \nabla \cdot (\bar{\rho}\tilde{Z}\tilde{u}) = \nabla \cdot \left[\bar{\rho} \left(D + \frac{\mu_t}{Sc_t} \right) \nabla \tilde{Z} \right] \quad (5.44)$$

where Y is the progress variable $Y = Y_{CO_2}$ and Sc_t is the turbulent Schmidt number which is chosen to be $Sc_t = 1$. The properties of the mixture then can be retrieved from

5. Implementation of the Presumed PDF Model into the CFD Code

the chemistry table:

$$\rho = \rho(Y, Z) \quad (5.45)$$

$$\lambda = \lambda(Y, Z) \quad (5.46)$$

$$c_p = c_p(Y, Z) \quad (5.47)$$

$$T = T(Y, Z) \quad (5.48)$$

$$\omega = \omega(Y, Z) \quad (5.49)$$

It now remains to close the chemical source term in (5.43). As mentioned before, this was done by application of a presumed-PDF for the defining variables. The PDF is presumed to be an adequate mathematical function, e.g. the beta-distribution, that contains free parameters. These parameters are determined from the moments of the stochastic quantities, i.e. the mean and variance. Furthermore, a joint PDF is needed for Y and Z . This is approximated by assuming statistical independence of the two variables and neglecting correlations between them. The sought filtered source term $\bar{\omega}$ then becomes a function of the filtered progress variable \tilde{Y} and mixture fraction \tilde{Z} and their variances $Y_v = \widetilde{Y^2} - \tilde{Y}^2$, $Z_v = \widetilde{Z^2} - \tilde{Z}^2$:

$$\bar{\omega}(\tilde{Y}, Y_v, \tilde{Z}, Z_v) = \int_0^1 \int_0^1 \omega(Y, Z) P_Y(Y, \tilde{Y}, Y_v) P_Z(Z, \tilde{Z}, Z_v) dY dZ \quad (5.50)$$

This integration is carried out as a preprocessing step before the actual simulation. A four-dimensional lookup table is created, such that for every realizable value of $\tilde{Y}, Y_v, \tilde{Z}, Z_v$ the properties of the thermophysical state can be interpolated:

$$\bar{\rho} = \bar{\rho}(\tilde{Y}, Y_v, \tilde{Z}, Z_v) \quad (5.51)$$

$$\tilde{\lambda} = \tilde{\lambda}(\tilde{Y}, Y_v, \tilde{Z}, Z_v) \quad (5.52)$$

$$\tilde{c}_p = \tilde{c}_p(\tilde{Y}, Y_v, \tilde{Z}, Z_v) \quad (5.53)$$

$$\tilde{T} = \tilde{T}(\tilde{Y}, Y_v, \tilde{Z}, Z_v) \quad (5.54)$$

$$\bar{\omega} = \bar{\omega}(\tilde{Y}, Y_v, \tilde{Z}, Z_v) \quad (5.55)$$

5. Implementation of the Presumed PDF Model into the CFD Code

To compute the variance of the controlling variables, transport equations for their second moments $\widetilde{Y^2}$, $\widetilde{Z^2}$ are solved:

$$\frac{\partial(\bar{\rho}\widetilde{Y^2})}{\partial t} + \nabla \cdot (\bar{\rho}\widetilde{uY^2}) = \nabla \cdot \left[\bar{\rho} \left(D + \frac{\mu_t}{Sc_t} \right) \nabla \widetilde{Y^2} \right] - 2\bar{\rho}\widetilde{\chi}_Y + 2\bar{\rho}\omega\widetilde{Y} \quad (5.56)$$

$$\frac{\partial(\bar{\rho}\widetilde{Z^2})}{\partial t} + \nabla \cdot (\bar{\rho}\widetilde{uZ^2}) = \nabla \cdot \left[\bar{\rho} \left(D + \frac{\mu_t}{Sc_t} \right) \nabla \widetilde{Z^2} \right] - 2\bar{\rho}\widetilde{\chi}_Z \quad (5.57)$$

The source term in (5.56) is preintegrated as well and included in the lookup table. The scalar dissipation rate $\widetilde{\chi}_\phi$ of $\phi = (Y, Z)$ is modeled by a linear relaxation hypothesis:

$$\bar{\rho}\widetilde{\chi}_\phi = \overline{\rho D |\nabla \phi|^2} = \bar{\rho} D |\nabla \tilde{\phi}|^2 + C_D \frac{\mu_t}{Sc_t} \frac{\tilde{\phi}^2 - \tilde{\phi}\tilde{\phi}}{\Delta^2} \quad (5.58)$$

Part III.

Results

6. Assessment of the Model Implementation

To verify the implementation of the presumed-PDF model, a number of test cases have been simulated. The results were compared to measurements and to results of other models that were available in OpenFOAM [®]. When different models were compared, the same grid and boundary conditions were used for all models.

All simulated cases from this and the next chapter have been plotted into a combustion diagram in figure 6.1. The underlying estimated time and length scales are summarized in table 6.1. All cases are in the thin reaction zones regime although The ORACLES case is already at the boundary to the broken reaction zones. The CIVB combustion is in the corrugated flamelets regime because the velocity fluctuations are rather small compared to the laminar burning velocity.

Quantity	Value
Flame speed	$s_L = 0.5m/s$
Integral length	$L = 20mm$
Flame thickness	$\delta_L = 0.33mm$
Velocity RMS	$u' = 2.36m/s$

(a) Combustion bomb (Sect. 6.2)

Quantity	Value
Flame thickness	$\delta_L = 0.64mm$
Flame speed	$s_L = 0.187m/s$
Integral length	$L \approx 10\%h = 2.5mm$
Velocity RMS	$u' \approx 0.5u_0 = 6.6m/s$

(c) Backward facing step (Sect. 6.4)

Quantity	Value
Karlovitz number	$Ka \approx 1.5$
Flame thickness	$\delta_L = 0.43mm$
Flame speed	$s_L = 0.33m/s$
Integral length	$L \approx 20\%h = 6mm$

(b) ORACLES (Sect. 6.3)

Quantity	Value
Integral length	$L = 2.4mm$
Chemical time	$\tau_c = 0.44ms$
Turbulent time	$\tau_t = 0.65ms$
Flame thickness	$\delta_L^0 = 0.175mm$
Flame speed	$s_L^0 = 40cm/s$

(d) Bunsen flame (Sect. 6.5)

Table 6.1.: Estimated time and length scales for the different simulation cases

6. Assessment of the Model Implementation

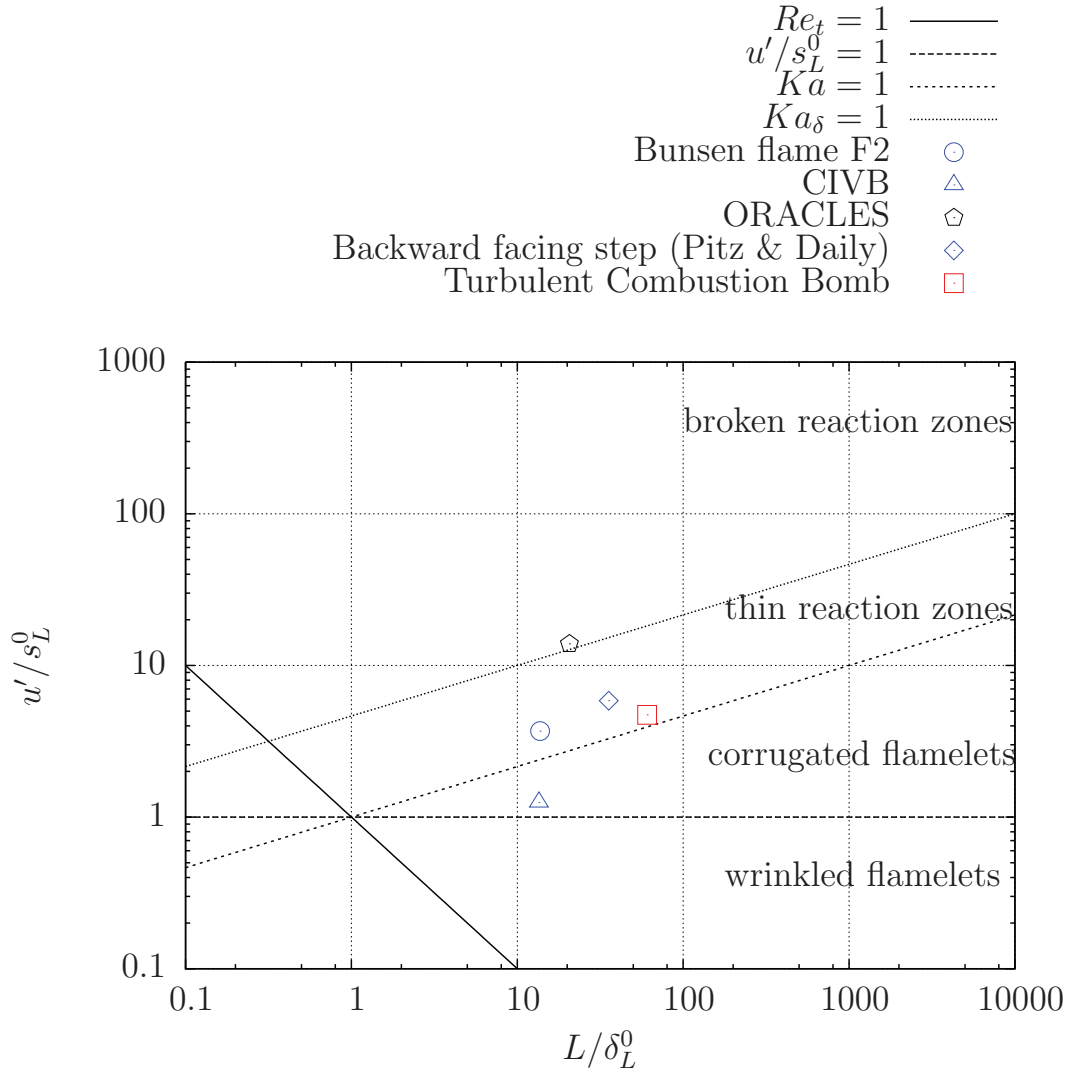


Figure 6.1.: Location of all simulated cases in the combustion diagram

6.1. Premixed Laminar Flat Flame

The laminar flat flame should be perfectly reproduced in a FGM based simulation, so it is good test case to check the validity of the implementation. The setup is sketched in figure 6.2. The chemical system was a stoichiometric propane/air mixture and the chemistry table was computed from the San Diego detailed chemistry mechanism [91].

The simulation was performed using the same code as for all subsequent simulations. Because the flow is laminar, the turbulence model was disabled and the variance of the progress variable was fixed to be zero. The simulation was then carried out in an one-dimensional computational domain. This was achieved by creating a three-dimensional grid with one cell thickness in y - and z -direction and special boundary conditions at these lateral boundaries. A fixed pressure boundary condition was used at the outlet. At the inlet, the mass flux was adjusted to be equal to mass flux at the outlet to fix the flame location.

The resulting profiles of temperature, density and axial velocity are shown in figure 6.3. They are in good agreement with the profiles obtained from simulations with the San Diego detailed chemistry mechanism using the software CANTERA [35]. However, there is a certain deviation between the detailed chemistry and the FGM computation. This can be attributed to the simplified treatment of the diffusion coefficient in the CFD code. While diffusion coefficients are computed in CANTERA, the diffusion coefficient in the CFD code is evaluated from the thermal conductivity at a constant Lewis number. Figure 6.4 shows the Lewis number variations across the flame front, extracted from the detailed chemistry computations. Although $Le = 1.4$ seems to be a good approximation, there are some deviations in the reaction zone which might cause the slight difference in the results in figure 6.3. Despite this, the laminar flat flame is well reproduced.

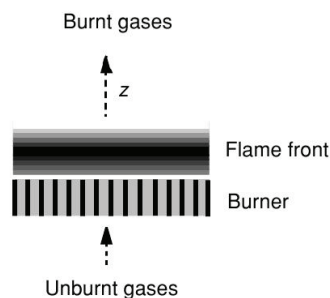


Figure 6.2.: Sketch of a premixed laminar flat flame [85]

6. Assessment of the Model Implementation

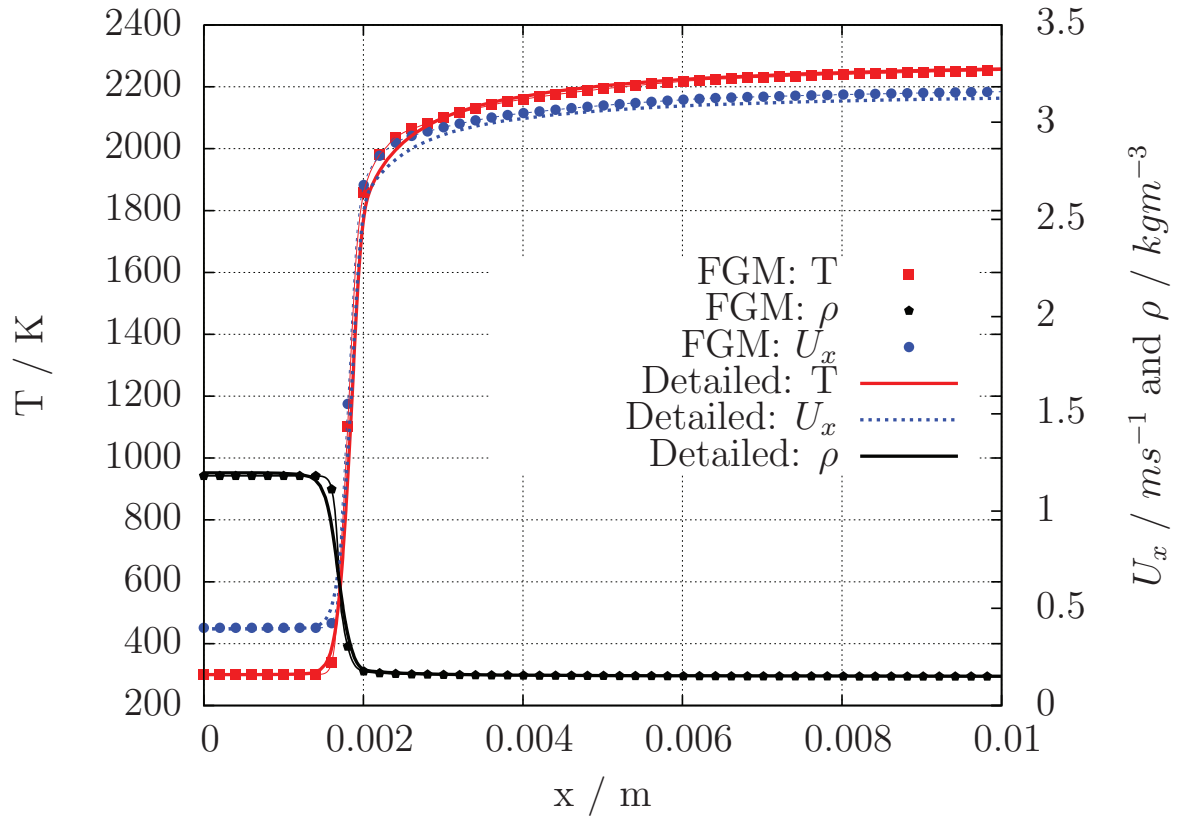


Figure 6.3.: Laminar premixed flame: profiles of temperature, density and velocity across flame front

6. Assessment of the Model Implementation

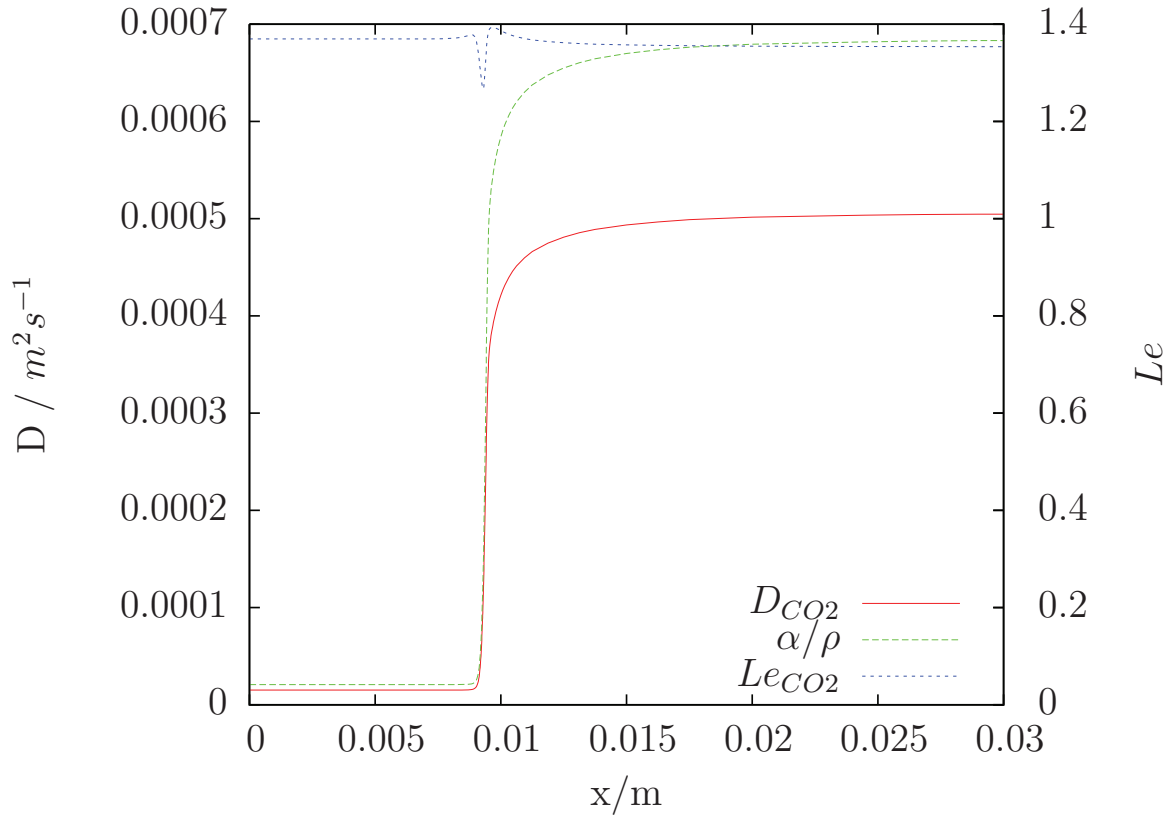


Figure 6.4.: Laminar premixed flame: Lewis number across flame front

6.2. Turbulent Combustion Bomb

This case was chosen to check the ability of the models to correctly reproduce the turbulent flame speed in the premixed regime. A sketch of the experimental setup of such a combustion bomb is shown in figure 6.5. The bomb initially contains a well defined, homogeneous mixture of fuel and air, in the present case a stoichiometric mixture of propane and air. The turbulence is generated by stirring the charge with a fan. Finally, the mixture is ignited in the center by an electrical spark. After ignition, the flame front spreads spherically through the volume, thereby interacts with the turbulence and gets wrinkled.

The results in this chapter are compared to experimental data from Nwagwe et al. [63]. In that work, the temporal evolution of the flame kernel radius was measured. The flame radius is extracted by processing images of high speed schlieren films. To define the initial conditions, Ref. [63] gives velocity RMS and integral length scale, which were obtained from LDV measurements.

Numerical Setup In the following simulations, the domain was chosen to be a box, much smaller than the entire volume of the combustion bomb in [63] and the simulations were only carried up to a point where a small fraction of the charge was burned. This was done to avoid a significant pressure rise and removed the necessity to take compressibility into account.

Grids at different refinement levels were used. A coarse one with a resolution of 31^3 cells, finer ones with 64^3 and 128^3 cells and a very fine grid with 256^3 cells. From a laminar

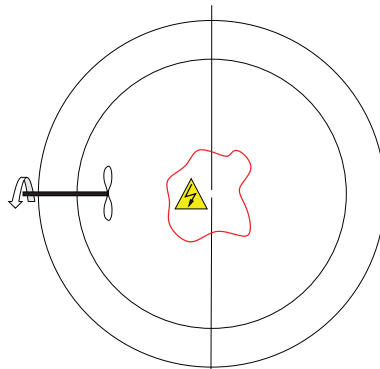


Figure 6.5.: Sketch of a turbulent combustion bomb

6. Assessment of the Model Implementation

Label	Combustion model	Remarks	Grid	Δ/δ_L^0	$\sqrt{\langle u'^2 \rangle}/ms^{-1}$
Plow	presumed-PDF		31^3	19.4	2.36
Phigh1	presumed-PDF		64^3	9.4	2.36
Phigh2	presumed-PDF		128^3	4.7	2.36
Phigh3	presumed-PDF		256^3	2.35	2.36
IPhigh1	presumed-PDF		64^3	9.4	4.72
IPhigh2	presumed-PDF		128^3	4.7	4.72
Wlow1	Weller model	algebraic Ξ , unstrained s_L	31^3	19.4	2.36
Wlow2	Weller model	algebraic Ξ , equilibrium s_L	31^3	19.4	2.36
Wlow3	Weller model	transport Ξ , unstrained s_L	31^3	19.4	2.36
Whigh	Weller model	algebraic Ξ , unstrained s_L	64^3	9.4	2.36
TFlow1	Thickened Flame	$F = 20$	31^3	19.4	2.36
TFlow2	Thickened Flame	$F = 40$	31^3	19.4	2.36
TFhigh1	Thickened Flame	$F = 20$	64^3	9.4	2.36
TFhigh2	Thickened Flame	$F = 40$	64^3	9.4	2.36

Table 6.2.: Performed simulations of the turbulent combustion bomb: Overview of simulations

Parameter	Value
Mixture	Propane/Air
Equivalence ratio	$\Phi = 1$
Initial temperature	$T_{initial} = 300K$
Initial pressure	$p_{initial} = 1bar$
Velocity RMS	$u' = 2.36m/s$
Integral length scale	$L = 20mm$
Domain cube length	$h = 0.2m$

Table 6.3.: Performed simulations of the turbulent combustion bomb: Common parameters

flame calculation with the complete chemical mechanism GRI3.0 [24], a flame thickness of $\delta_L^0 = 0.33mm$ was computed for the present case. The ratios of cell edge length to laminar flame thickness are given in table 6.2, the are $\Delta/\delta_L^0 = 19.4, 9.4, 4.7$ and 2.35 , respectively.

The initial turbulence was generated by the method of turbulent spots [49]. The computational domain was filled up with vortons, that induced divergence free turbulent fluctuations. The inner distribution of these spots was chosen according to homogeneous turbulence with an energy spectrum $E(k) \propto k^{-5/3}$. It was possible to directly prescribe the integral length scale, since it is connected to the spot size. The RMS was imposed by properly scaling the turbulent fluctuations.

6. Assessment of the Model Implementation

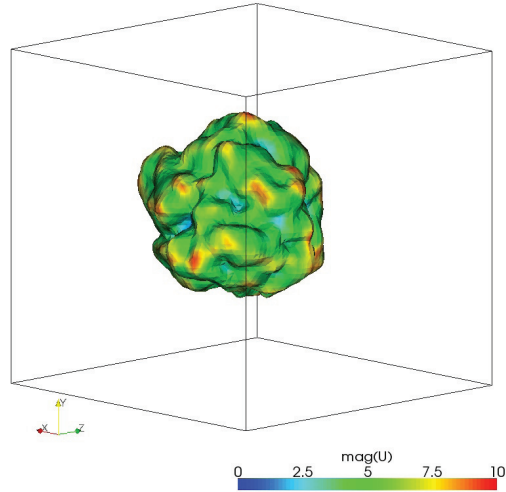


Figure 6.6.: Turbulent combustion bomb: snapshot of flame front (isosurface of $T = 1000K$), colored by magnitude of velocity (presumed-PDF model computation, 64^3 grid)

No attempt has been made to model the ignition process in detail. Artificial source terms were inserted into the progress variable equation to initiate the combustion. The strength, duration and time profile of the source term was chosen by trial and error. The main problem here was to ensure that the combustion process sustained after removing the source term and to avoid numerical instabilities that occurred when the source term was too strong or the ignition region too large. Despite this, there was no noticeable effect of the source term parameters on the final result.

Simulations Among all examined cases in [63], only two were selected for validation: these that utilized propane as fuel at atmospheric initial pressure. Two different turbulence intensities have been investigated. The parameters are summarized in table 6.2.

Results and Discussion The result of the simulations are plots of the flame kernel diameter versus time shown in figures 6.7, 6.8, 6.9 and 6.10. A snapshot of the flame front is shown in figure 6.6. It can be easily recognized, how the turbulence has wrinkled the flame front.

It has been decided to compare the results directly to the plots of flame radius vs. time from Ref. [63] rather than performing a regression analysis and report flame speeds

6. Assessment of the Model Implementation

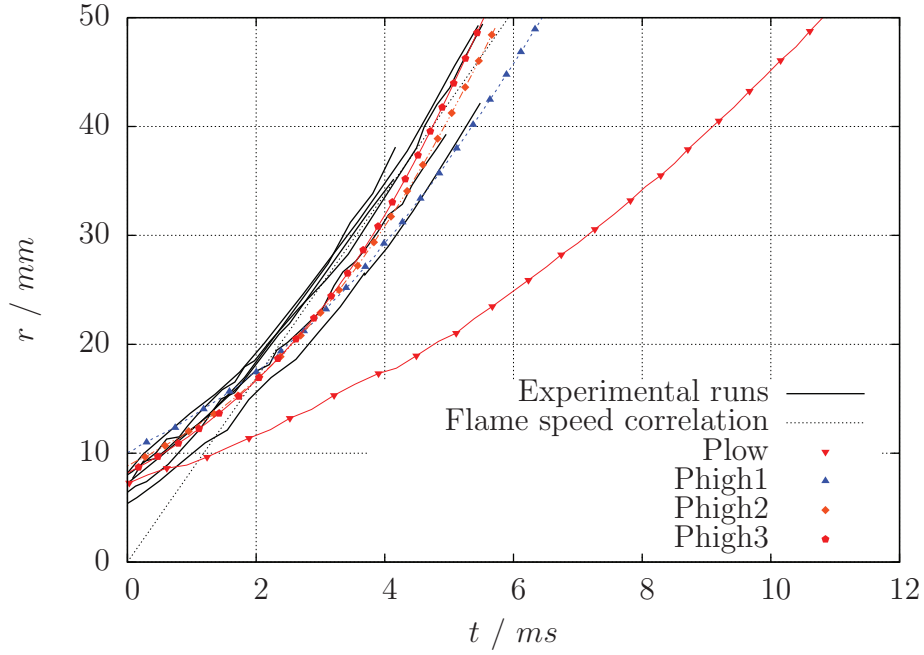


Figure 6.7.: Development of flame kernel diameter in simulations of turbulent combustion bomb with Presumed-PDF model. The six experimental runs had the same initial conditions and give an impression of the experimental repeatability.

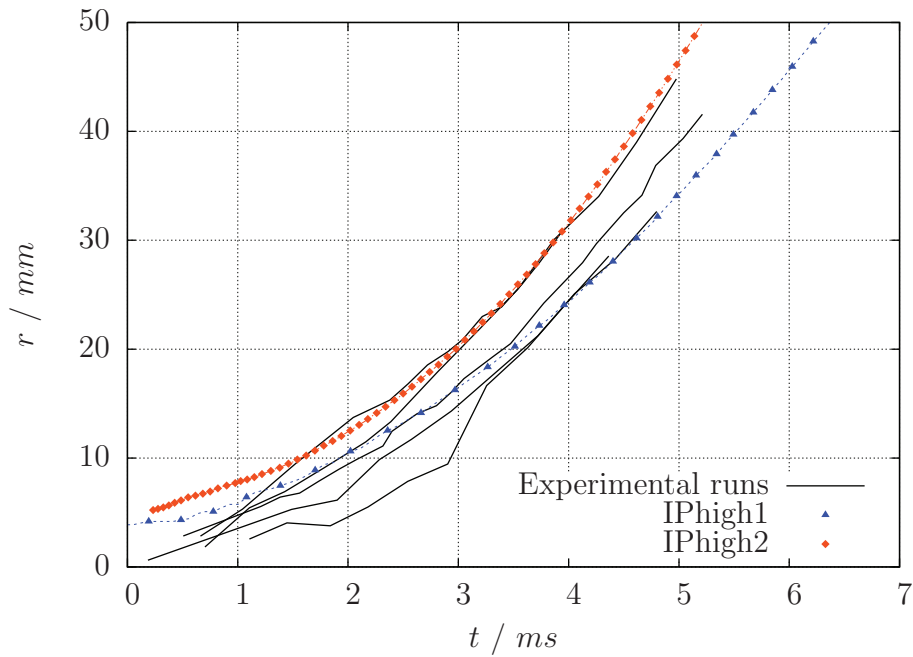


Figure 6.8.: Development of flame kernel diameter in simulations of turbulent combustion bomb with Presumed-PDF model at high turbulence intensity

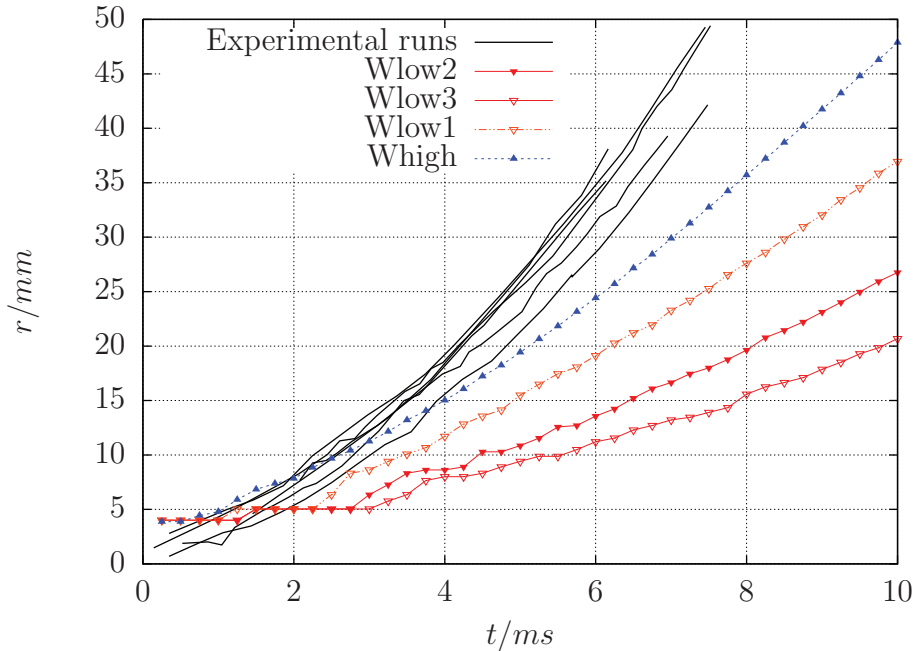


Figure 6.9.: Development of flame kernel diameter in simulations of turbulent combustion bomb with Weller $b-\Xi$ model. The six experimental runs had the same initial conditions and give an impression of the experimental repeatability.

because the former is the primary result of the experiment as well as of the simulations. Furthermore, the experiments as well as the simulations cover the initial transient phase between ignition and constant speed flame propagation which is recognizable in these plots.

The simulation results have been evaluated by summing up the volume of all grid cells with a temperature $T > 1000K$. This volume was equated with that of a sphere and the mean flame radius was the radius of that sphere.

For the case with low turbulence intensity, the experimental flame speeds are well reproduced by the presumed-PDF model, provided that the grid resolution is fine enough. The simulations also show the increase of the burning rate in the early stage of the flame propagation and its convergence to a steady state later on. There are deviations between the curves at ignition because all LES flames start at a diameter of approximately $5mm$, This corresponds to the edge length of a grid cell on the coarsest grid and was the minimum flame radius that could appear since the size of the ignition zone was kept constant throughout all simulations. The grid with the coarsest resolution $\Delta/\delta_L^0 = 19.4$ does not give satisfactory results. But for more increased resolutions, a

6. Assessment of the Model Implementation

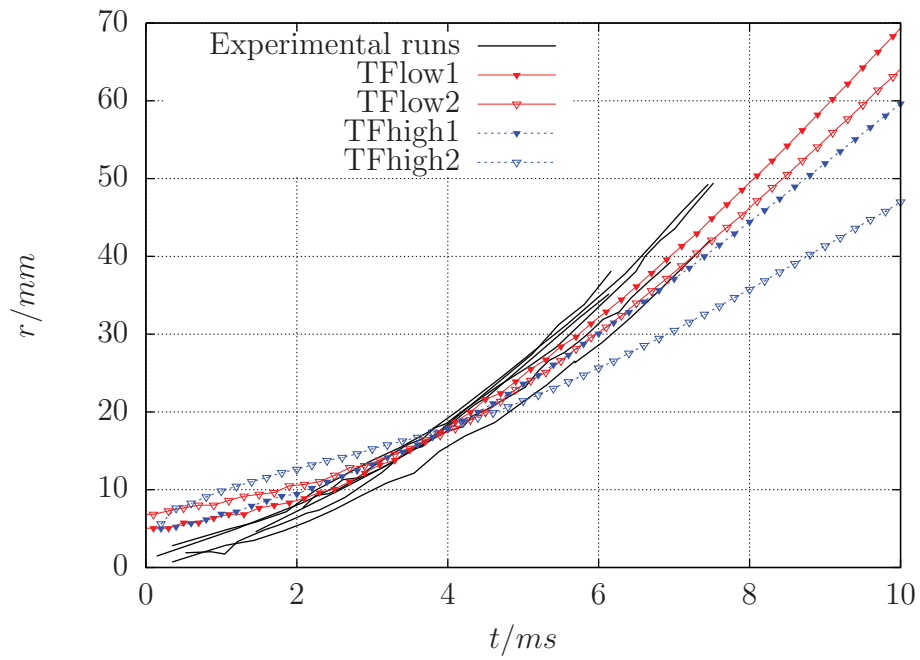


Figure 6.10.: Development of flame kernel diameter in simulations of turbulent combustion bomb with Artificially Thickened Flame model. The six experimental runs had the same initial conditions and give an impression of the experimental repeatability.

6. Assessment of the Model Implementation

convergence towards the measurement can be recognized, as it has to occur for every reasonable numerical model.

To assess the ability of the presumed-PDF combustion model to reproduce the interaction of the flame with turbulence, simulations at a higher turbulence intensity have been performed as well. The experimental data for this case shows more scatter, especially in the early stage of flame development. Nevertheless, all experimental runs end up with the same steady propagation speed, which agrees very well with that of the numerical simulations. The effect of higher turbulence intensity, i.e. an acceleration of the flame, is thus correctly reproduced.

It is also interesting to see, what results could be achieved by other combustion models on the same grid with the same boundary conditions. Therefore, simulations using the artificially thickened flame model have been carried out, as well as simulations with Weller's flame surface wrinkling model.

The artificially thickened flame model shows a good agreement to the measured flame kernel development. For the coarse grid, there is also only little dependence of the result on the thickening factor F . A strong thickening on a fine grid had bad influence on the result quality on the current case.

No good results could be obtained with the flame surface wrinkling model. The results were very sensitive to the model options and a convergence to the measurements with increasing grid resolution can be conjectured. These results are somewhat contrary to these published by Nwagwe et al. [63], where the authors could observe very good results already with 32^3 grid cells. This could be a sign of errors in the model implementation in the OpenFOAM standard package but could not be clarified within the current work.

6.3. ORACLES

The acronym ORACLES stands for One Rig for Accurate Comparison with LES. The rig consists of a combustion chamber with a symmetric expansion, which is fed by two channels [5]. All cross sections are rectangular and the setup is in principle two-dimensional. One half of the symmetric setup is sketched in figure 6.11. The feeding channels have a length of 3 meters and combustion chamber is 2 meters long, measured from the expansion step. Due to the length of the feeding channels, the inflow is a

6. Assessment of the Model Implementation

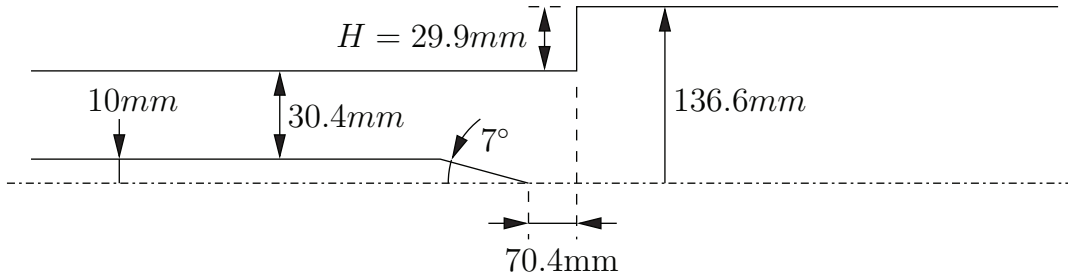


Figure 6.11.: Sketch of the upper symmetry half of the ORACLES test rig

fully developed plane channel flow. The walls of the combustion chamber are thermally insulated.

The rig can be driven in different modes, i.e. different mass flow rates in both channels and also different equivalence ratios in both channels. Thus, the combustion may be premixed or partially premixed. In the current work, a symmetric mode with an equivalence ratio of $\Phi = 0.75$ and a bulk velocity $U_{bulk} = 11\text{ m/s}$ in both channels was selected. The combustion is isobar at atmospheric pressure.

This setup has some important features, which must be taken care of in the numerical simulation. In the isothermal case, the flow downstream of the expansion is not symmetric because the area expansion ratio $A_r = (H_{ch} + 2H)/H_{ch}$ is above the threshold $A_r > 1.5$ [2]. In the combustng case, the asymmetry disappears. This feature should be reproduced by the simulation.

Furthermore, in the reacting flow, a symmetric flapping of the flame can be observed, i.e. a pulsation of the mass flow rate with an amplitude of $\sim 20\%$ and a frequency of $48.5 \pm 2.5\text{ Hz}$. That leads to the occurrence of characteristic large-scale structures in the flow field. The wavelength of this instability is $\sim 2\text{ m}$ which indicates an origin far upstream in the feeding channel [23].

Numerical Setup The computational domain started at $2.3H$ upstream of the expansion step at the tip of the splitter plate. The combustion chamber was only modelled up to one quarter of its full length ($16.7H$) and an outlet boundary condition was applied there. The grid extended $2.6H$ in the transverse direction and cyclic boundary conditions were applied to the front and back planes.

6. Assessment of the Model Implementation

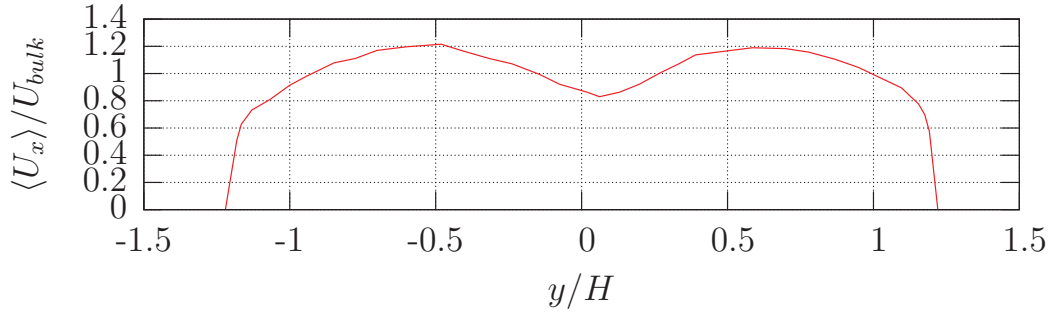


Figure 6.12.: Mean velocity profile at inlet in ORACLES rig

The experimentally observed velocity pulsation should naturally occur in the numerical model if the feeding channels with its full length were included in the computational domain. To avoid this computational overhead and even so include the effect of this pulsations the simulation, the following velocity was prescribed at the inlet:

$$u(y, t) = U_0(y) [1 + A \sin(2\pi ft)] + u'(y, t) \quad (6.1)$$

The mean velocity profile $U_0(y)$ is shown in figure 6.12 and was extracted from measurements as reported in [23]. The amplitude was set to $A = 0.25$ and the frequency to $f = 50Hz$ as was suggested as well in [23]. The turbulent fluctuations have been generated by the method of turbulent spots [49]. A spectrum of homogeneous turbulence has been prescribed. The length scale was set to 20% of the feeding channel height. With the current implementation, only homogeneous turbulent fluctuations could be created, although the method in general could be used for inhomogeneous turbulence as well. The velocity RMS was uniformly set to 20% of the bulk velocity.

The computational domain was meshed by a grid with approximately 1 million cells. The grid was refined in the region of the shear layers behind the expansion and the splitter plate and towards the walls. The LES filter width was between $1mm$ in the fine regions and $2mm$ in the coarser ones.

Results and Discussion While the isothermal flow simulation showed the expected asymmetry, in simulations of the combusting case, the flow was symmetric. Also, the symmetric flapping of the flame front occurred. Some time instants of the flame surface are shown in figure 6.13 and 6.14. The flapping causes the bulges on the flame surface which travel downstream.

6. Assessment of the Model Implementation

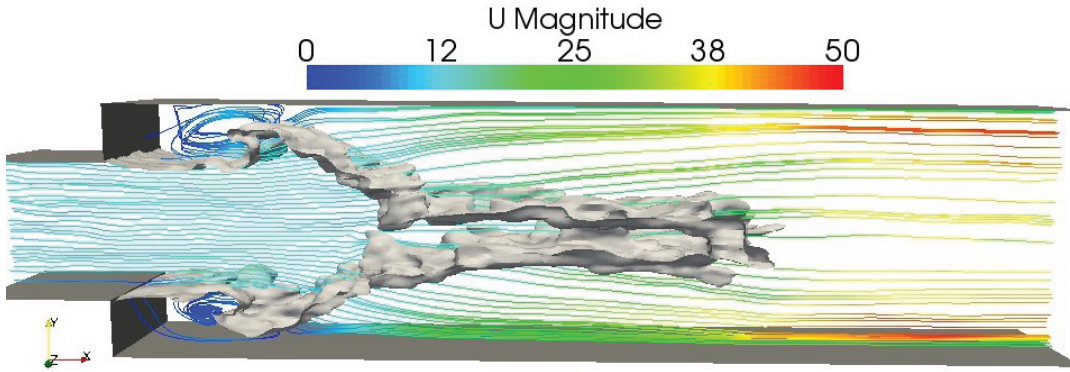


Figure 6.13.: Instantaneous flame surface in simulation of ORACLES rig

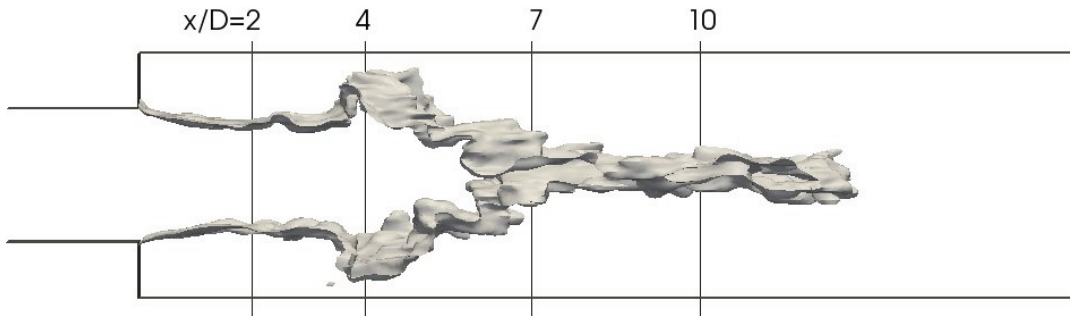


Figure 6.14.: Position of evaluated profiles in simulation of ORACLES rig

Mean velocity and RMS profiles were evaluated at four different axial positions, see figure 6.14. The profiles were averaged in time and over the homogeneous z -direction. A comparison with measurements from literature are shown in figure 6.15 and 6.16. For comparison, also results of RANS simulations from the literature are included in some of the figures.

The mean velocity agrees well with the measurements. The velocity RMS shows a reasonable agreement near the inlet and at the on the farthest downstream location. In the intermediate range, the velocity RMS in the wall region is considerably overpredicted while it is still in good agreement near the symmetry axis. This may indicate a poor convergence of the time averaging in the wall region. This region is characterized by large structures of the symmetric flame flapping (see e.g. figure 6.14). Maybe an even longer time interval is needed to reach convergence of time averaging when such low-frequency structures appear. However, compared to the RANS simulations, the results of the presumed-PDF model represent the measurements better.

6. Assessment of the Model Implementation

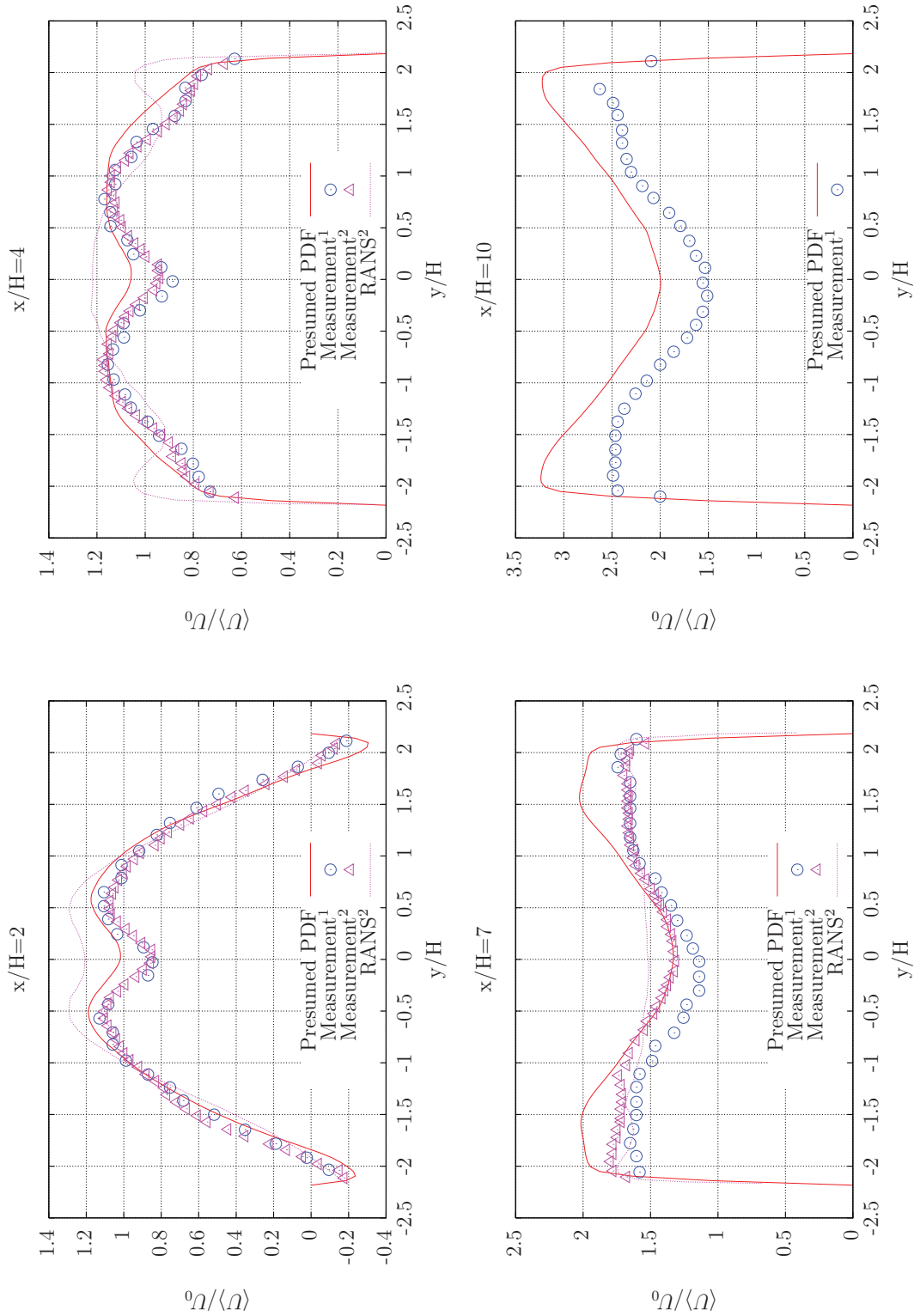


Figure 6.15.: Mean velocity profiles in ORACLES rig, computed with presumed PDF model and compared with data from literature (1: [23], 2: [51])

6. Assessment of the Model Implementation

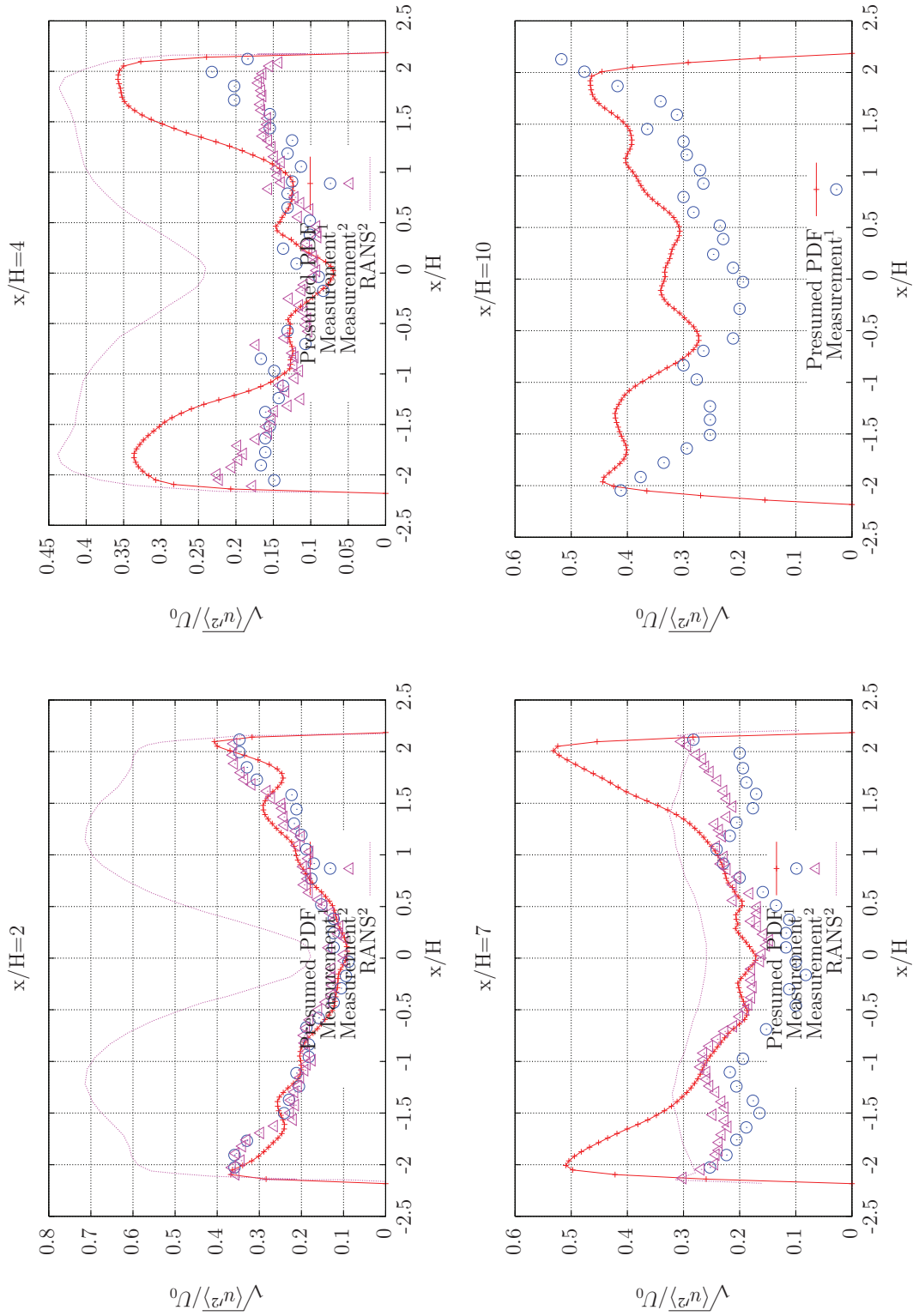


Figure 6.16.: Profiles of axial velocity fluctuation in ORACLES rig, computed with presumed PDF model and compared with data from literature (¹: [23])

6.4. Backward Facing Step

This test case again utilizes a lean homogeneous combustion mixture of propane and air. The combustion takes place in a confined chamber with cooled walls. This requires to account for heat losses and thus a variable enthalpy in the chemistry table. The flame is stabilized behind a backward-facing step. The characteristics of this case are described e.g. in [28], velocity measurements have been published in [69] and temperature measurements are taken from [88]. The setup is sketched in figure 6.17.

The mixture has an equivalence ratio of $\Phi = 0.57$. The mean velocity at the inlet of the combustion chamber above the step is $U_0 = 13.3m/s$. Together with the step height of $H = 25.4mm$, a Reynolds number $Re = U_0H/\nu$ of $Re = 22100$ results. The combustion chamber is isobaric at $p_0 = 1bar$.

Numerical Setup Only the part surrounded by the dashed line in figure 6.17 is included in the numerical model. The test case is two-dimensional plane. For LES, the z-direction needs to be resolved as well and the grid thus extends $3H$ into the z-direction. Cyclic boundary conditions have been applied to the front and back plane. The computational domain is resolved with 500 000 hexahedral cells. The grid is stretched to refine the shear layer and the wall region. The LES filter width then lies between $\Delta = 0.75mm$ in the best resolved area (immediately behind the step) and $\Delta = 2.1mm$ in the coarsest area (at the entrance of the convergent exit).

At the walls, the temperature has been prescribed to $T_w = 300K$. At the inlet, a constant mean velocity with superimposed turbulent fluctuations has been prescribed. The fluctuations were white noise with an amplitude of 4% of the mean for the streamwise velocity component and 2% for the transversal components. Although more elaborated

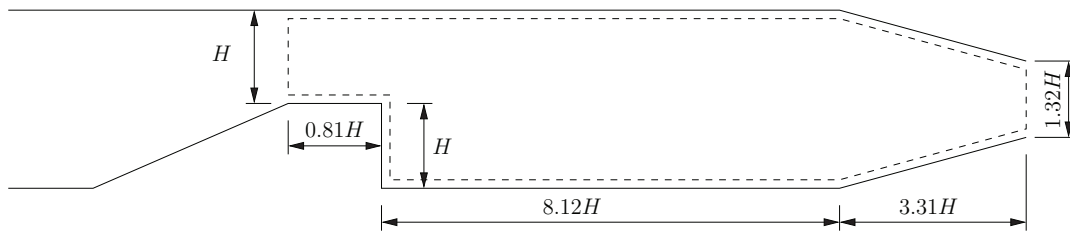


Figure 6.17.: Sketch of the backward-facing step test rig

6. Assessment of the Model Implementation

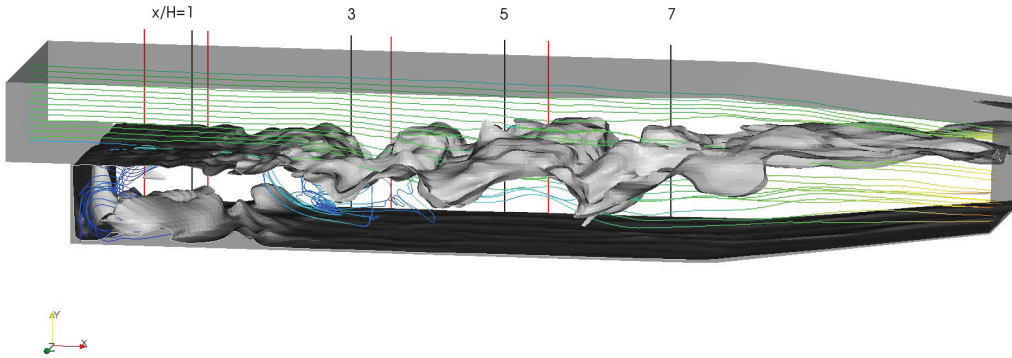


Figure 6.18.: Instantaneous flame surface in simulation of backward facing step (presumed-PDF model). The red lines show the location of the profiles of the mean temperature at $x/H = 0.4, 1.2, 3.5$ and 5.4 respectively. The black lines show the locations of the mean velocity profiles.

methods for generation of the fluctuations were available, this has proven to be sufficient in this case.

Simulations Simulations with three different models have been carried out on the same grid with the same boundary conditions. Besides the presumed-PDF model, the $b-\Xi$ model and the artificially thickened flame model have been applied.

Results and Discussion The LES is able to capture the qualitative features of this flow: the mixing layer between the incoming stream of unburnt mixture and the recirculating exhaust gases behind the step rolls up and creates Kelvin-Helmholtz instabilities. This is illustrated in figure 6.19. In the LES, the roll-up occurs slightly too late but the pictures generally match.

To judge the results quantitatively, profiles of mean velocity and temperature have been extracted and compared to the experimental data from [88]. The mean velocity profiles at four axial positions are shown in figure 6.20. In figure 6.21, the mean temperature profiles at four other axial positions are shown. These profiles have been averaged in time and along the homogeneous z -direction.

6. Assessment of the Model Implementation

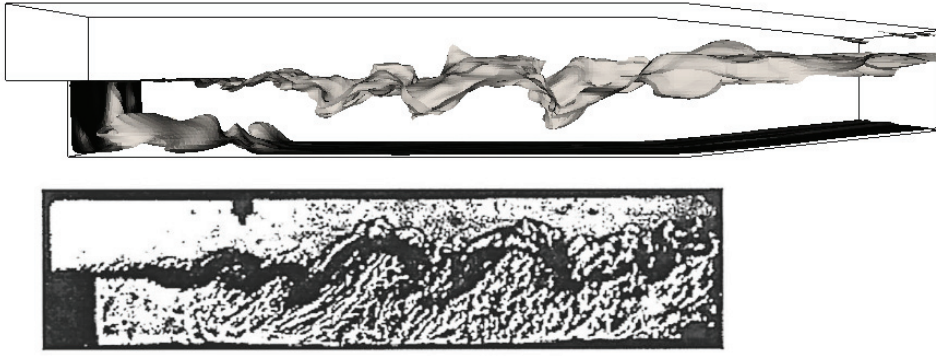


Figure 6.19.: Instantaneous flame surface in simulation of backward facing step (presumed-PDF model) compared to a Schlieren photograph (below)

To get an impression of the influence of the combustion modeling technique, also results from simulations with Weller's $b-\Xi$ model and with the artificially thickened flame model have been included in the figures.

The velocity field is good reproduced by all models except the $b-\Xi$ model which shows some noticeable deviations in the recirculation region.

The temperature field is best predicted by the presumed-PDF model although the gradient of the mean temperature across the mixing layer is a little bit too low. This is even more pronounced in the results from the artificially thickened flame model. The $b-\Xi$ model shows a qualitatively wrong result with much too high gradients in the temperature profiles. With increasing simulation time, the flame surface even developed into a perfectly smooth plane which is regarded as unphysical. Weller et al. [88] mentioned in their work, that neglecting the influence of strain on the laminar flame speed resulted in too intense heat release and suppression of the shear layer structures but using the strained flame speed did not cure this behavior in the current simulations.

6. Assessment of the Model Implementation

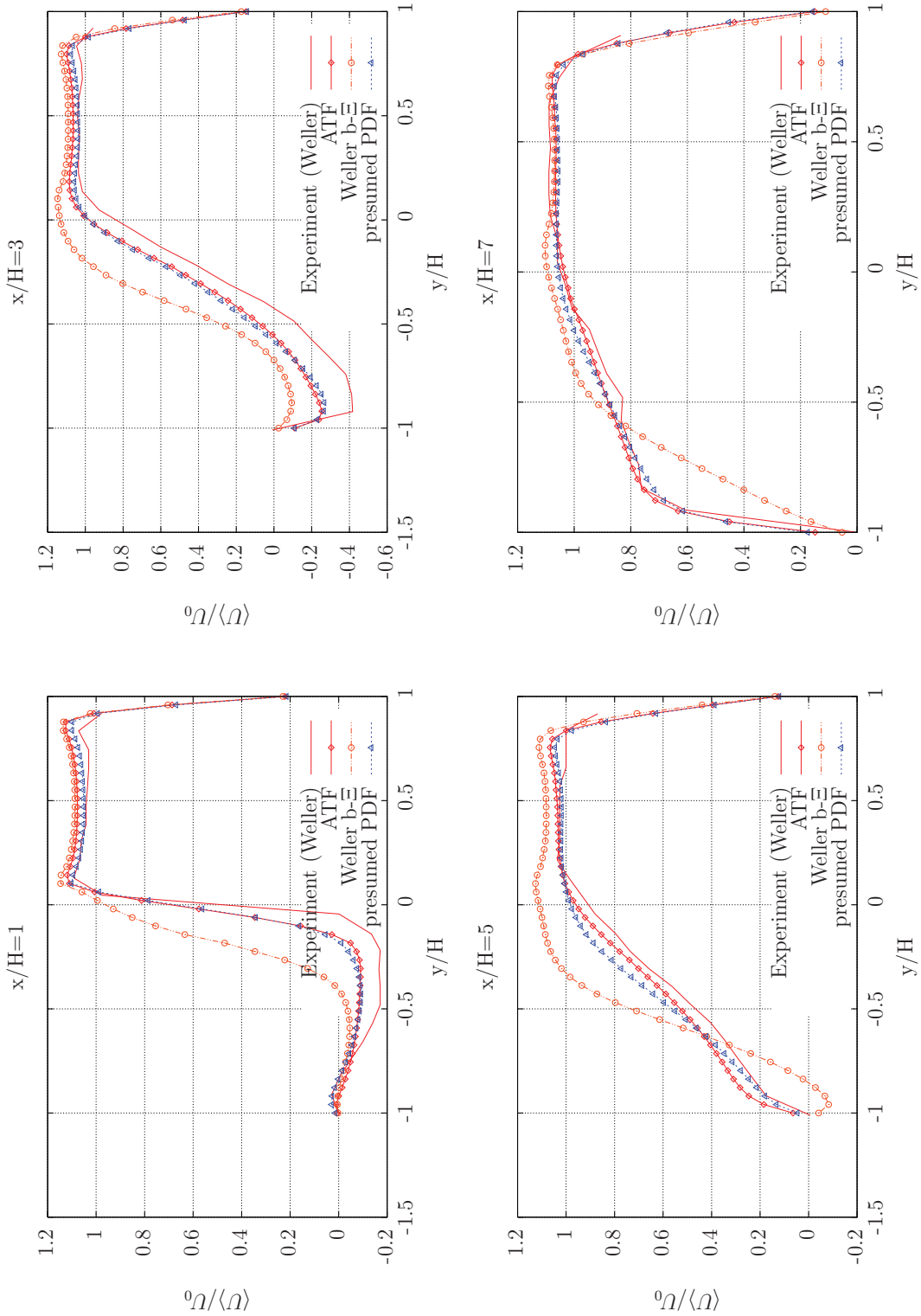


Figure 6.20.: Normalized mean velocity profiles in backward-facing step test case. Experimental data from [88]

6. Assessment of the Model Implementation

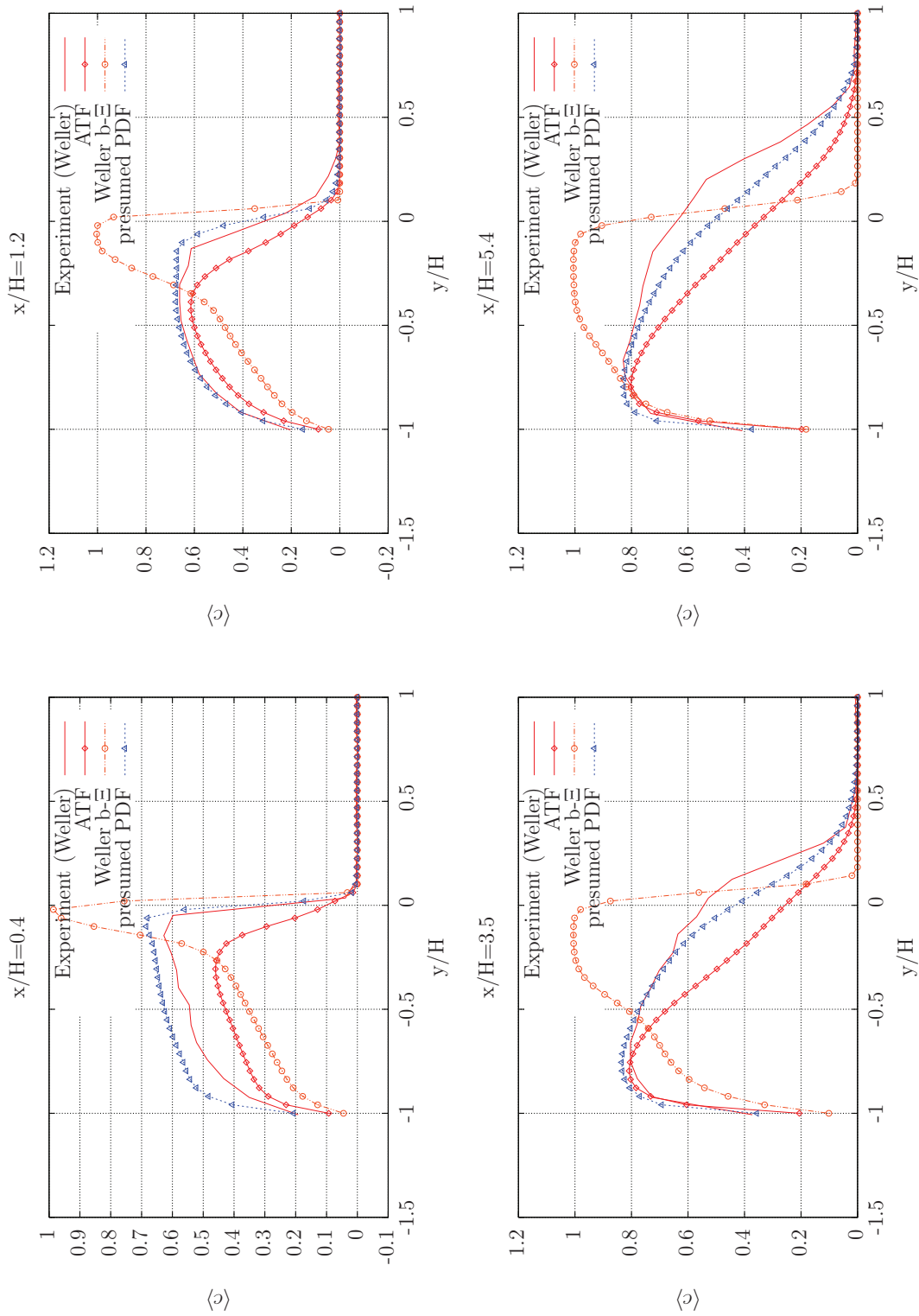


Figure 6.21.: Normalized mean temperature $c = (T - T_u)/(T_{ad} - T_u)$ profiles in backward-facing step test case. Experimental data from [88].

6.5. Bunsen Flame

The Bunsen flame is a common object for model validation and has been experimentally investigated by many researchers in different variations. This test case is included here, because it has some similar features as the CIVB case described above: the combustion is essentially premixed but entrainment of air occurs from the surrounding. Thus, a partially premixed formulation of the combustion model is required.

For the current test, the Bunsen flame of Chen et al. [16] was selected. This experiment was developed within the JOULE project at RWTH Aachen for validation of combustion models. All data are available on the website [15] of the Institute for Combustion Technology. It has been used for validation e.g. by Hoffmann [42], Herrmann [41] and Pitsch et al. [68]. From the different flame configurations that have been investigated by Chen, only the configuration F2 has been simulated. A sketch of the experimental setup is shown in figure 6.22. It consists of a central jet which is ejected by a nozzle with a diameter of $D = 12mm$. The flame is stabilized by a pilot flame that burns on a perforated plate with a diameter of $D_{coflow} = 68mm$. The burner was operated with methane as fuel and both streams had the same composition $\Phi = 1$.

From the chemical and physical time and length scales which are given in [16] it follows for the ratio of integral length scale of turbulence to the flame thickness $L/\delta_L^0 = 13.7$ and for the ratio of velocity RMS to laminar flame speed $u'/s_L^0 = 3.7$. The flame is therefore located well within the thin reaction zone regime.

Numerical Setup The computational domain was cylindrical with a diameter of $24D$ and a length of $33D$. The grid had a block-structured topology and consisted of approximately 700 000 hexahedral cells. By grading the resolution along the block edges, a LES filter width of $\sim 0.3mm$ could be achieved around the centerline. In the transition region between core jet and coflow the filter width raises to $\sim 0.7mm$ and is $\sim 1mm$ in the coflow region.

At the central jet inlet, a mean velocity profile according to the measurements was prescribed. Turbulent velocity fluctuations were superimposed and again generated by the turbulent spot method [49]. The coflow velocity was very slow compared to the central jet. A constant mean velocity of $U_{coflow} = 1.5m/s$ was prescribed. Special care was required to set up the lateral boundaries, since air entrainment was possible across

6. Assessment of the Model Implementation

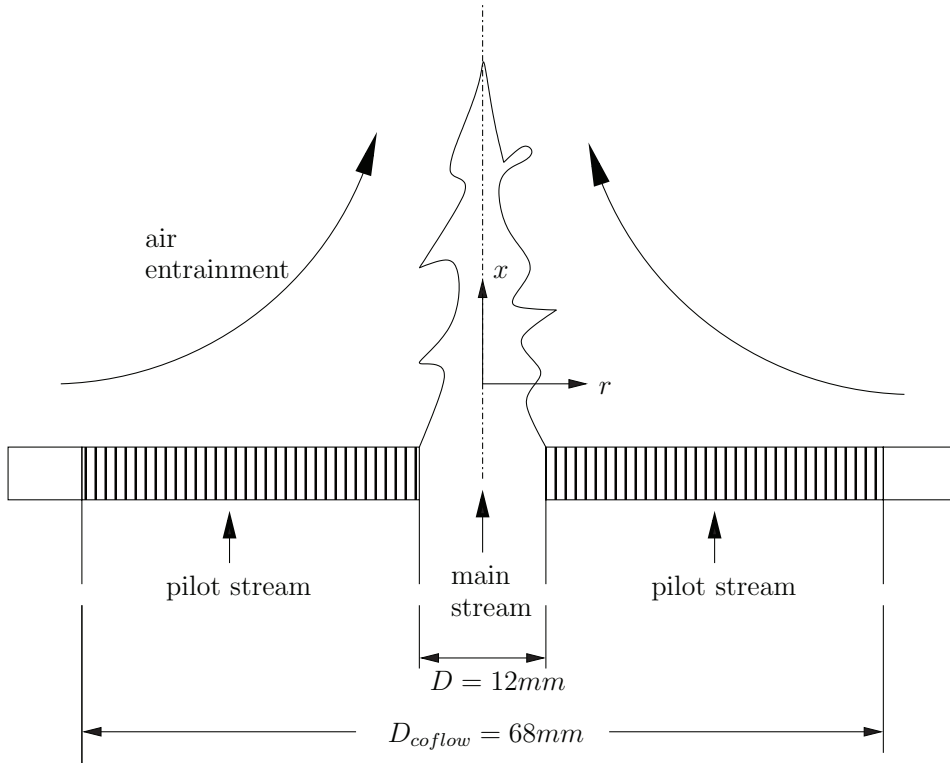


Figure 6.22.: Sketch of the Bunsen flame setup

these surfaces. This was treated by specifying the total pressure p_{tot} . When entrainment occurs, the static pressure at the boundary was calculated according to the Bernoulli equation from the total pressure and the entrainment velocity

$$p = p_{tot} - \frac{\rho}{2} u_{in}^2 \quad (6.2)$$

The entrainment of air made the combusting mixture inhomogeneous and required to include the mixture fraction as additional coordinate into the chemistry table. Unfortunately, heat losses occurred at the perforated plate of the pilot burner and reduce the enthalpy and therefore temperature of the coflow below the adiabatic flame temperature to approximately $c = 0.6$. To account for this as well would require to include the enthalpy as a coordinate into the chemistry table as well. Although the implementation would allow this, it has been currently omitted to limit the complexity of the simulation and only the mixture fraction was accounted for. By doing so, a deviation of the temperature from the measured profiles is expected. But only a limited influence on the velocity profiles is expected because the impact of combustion on the momentum equa-

6. Assessment of the Model Implementation

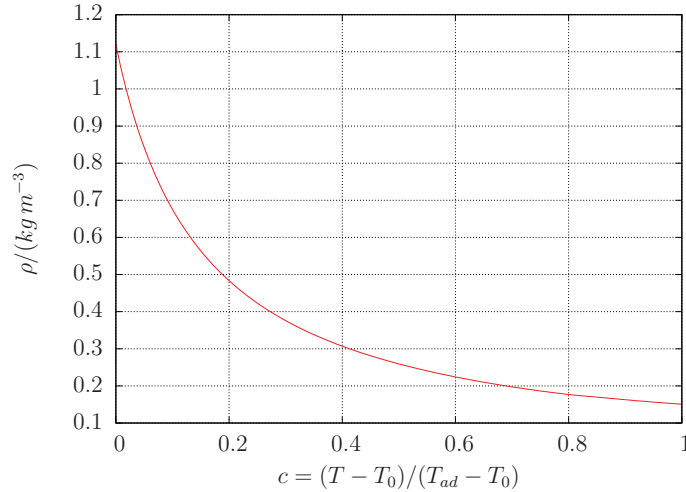


Figure 6.23.: Dependency of density from normalized temperature c for a stoichiometric mixture of CH_4 /air at $T_0 = 300K$

tion is only by changing the density. The dependency of density from the temperature is shown exemplary in figure 6.23 for a selected enthalpy and it is recognizable that the major density changes happen at lower temperatures.

Results and Discussion For validation, the time averaged streamwise velocity, the turbulent kinetic energy, the mean temperature and its RMS were available. Figure 6.24 shows contour plots of the axial velocity field in the isothermal and the reacting flow. The isothermal and reacting fields are clearly distinct because of the gas expansion due to combustion which accelerates the flow. The agreement between the numerical simulations and the measurements is good. Profiles of velocity at different heights above the nozzle are shown in figure 6.25. The experimental curves for the reacting case show a plateau near the axis around $r/D \approx 0$ which looks like problems in the measurements but is not commented in the literature. The plots also show profiles of the turbulent kinetic energy for the reacting flow case which is also in good agreement.

The flame in the Bunsen burner is conically shaped and the cone aperture angle and thus the cone length is related to the central nozzle's exit velocity v_u and the turbulent flame speed s_T :

$$\frac{s_T}{v_u} = \sin \theta \quad (6.3)$$

According to [16], the instantaneous flame height H_c/D is 10.5. It is defined as the height above the burner, where most of the fuel is consumed. After time averaging

6. Assessment of the Model Implementation

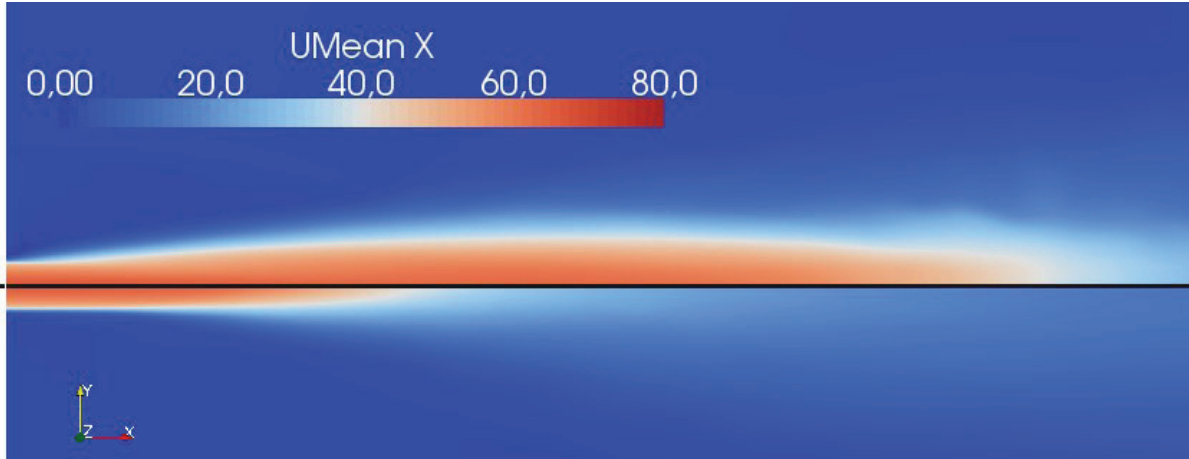


Figure 6.24.: Time averaged fields of axial velocity. The lower half shows the isothermal case, the upper half the reacting flow.

the numerical results, this height was found to be approximately $H/D = 9.5$, which is slightly too short but still in good agreement. This shows that the simulation reasonably predicts the turbulent flame speed. Figure 6.27 shows an example of the flame surface and the axial velocity field at some time instance.

Finally, plots of the mean temperature and temperature RMS are shown in figure 6.26. At the lower positions next to the nozzle, the maxima of the numerically computed temperatures are too high. This can be attributed to the assumption of an adiabatic flow which was used here. From the lowest profile at $x/D = 2.5$, it is obvious that due to the heat losses at the perforated pilot burner plate, the maximum temperature reaches only 60% of the adiabatic flame temperature. The temperature maxima are captured better further downstream because heat losses decrease and the influence of entrainment increases there.

All in all, the model seems to perform well for this partially premixed combustion case. Additionally, it was tried to apply the flame surface wrinkling, model as it is implemented in the software OpenFOAM, to this combustion test case because it is also extended for partially premixed combustion. However, this attempt was not successful because the calculation of the temperature from the enthalpy, which is done via newton's method, spuriously failed. This could be because of an inconsistent transport of enthalpy and mixture fraction. Presumably, enthalpy is transferred by numerical inaccuracies to the part of the mixture with a lower heat capacity. This leads to an exaggerated heating of this part of the mixture with unrealistically high temperatures.

6. Assessment of the Model Implementation

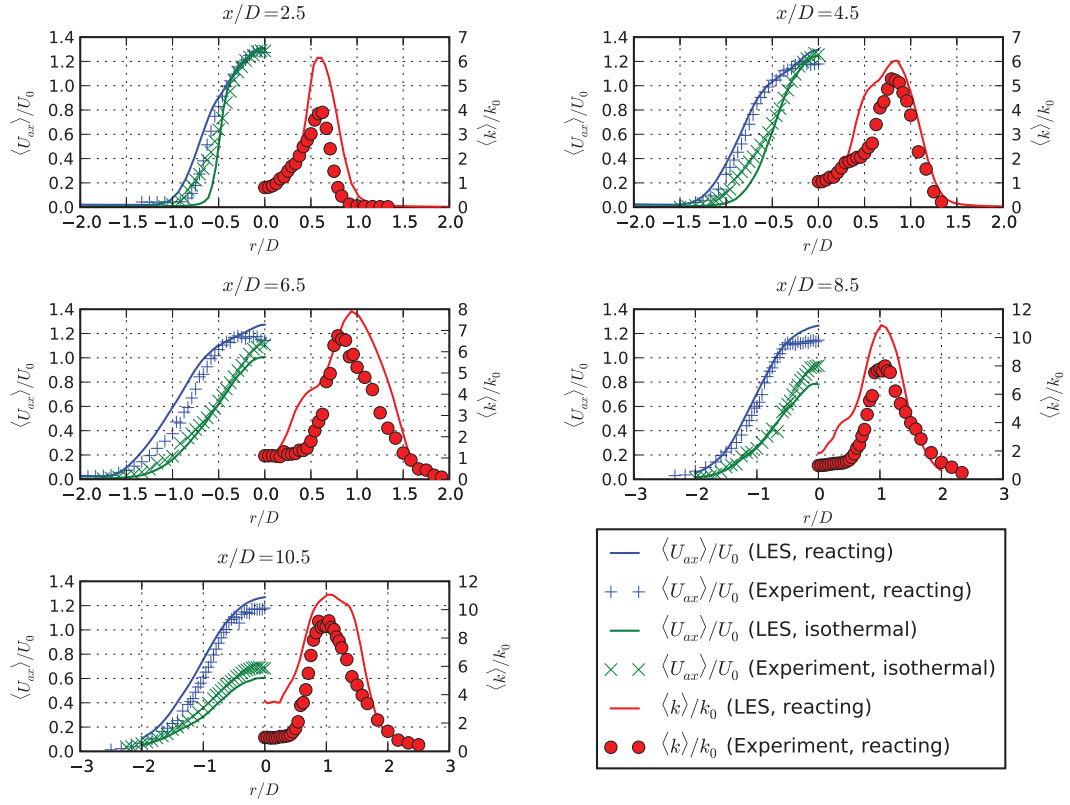


Figure 6.25.: Mean velocity profiles in Bunsen flame test case. Experimental data: [15].

6. Assessment of the Model Implementation

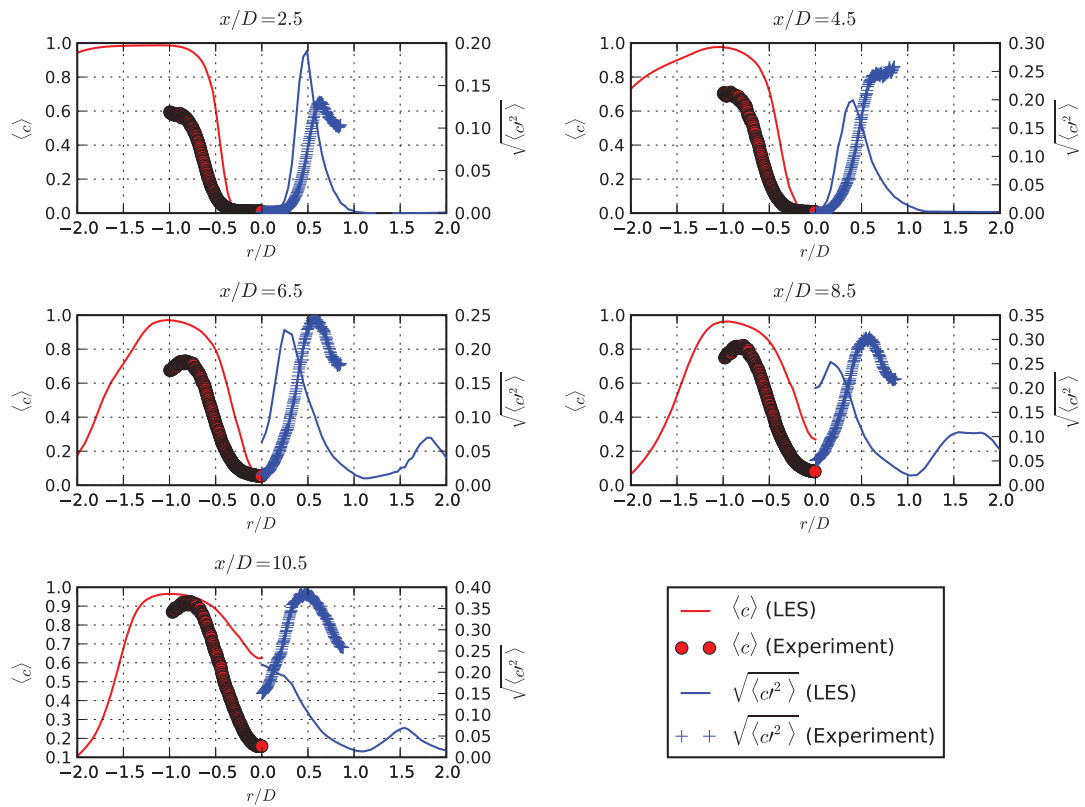


Figure 6.26.: Mean temperature profiles in Bunsen flame test case. Experimental data: [15].

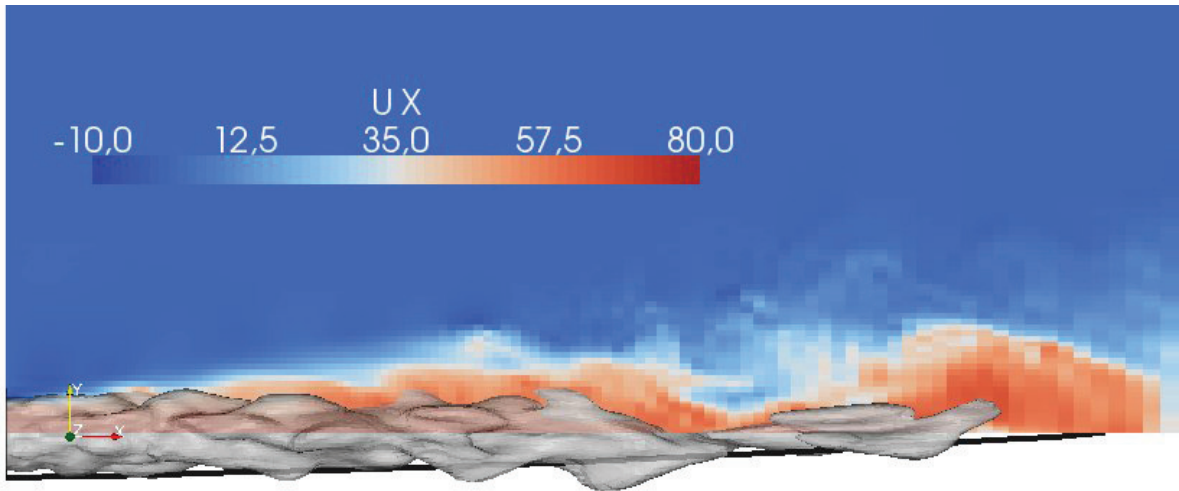


Figure 6.27.: Instantaneous flame surface. The thick black line shows the time averaged flame contour from [16]

6.6. Summary of the Model Assessment

In the presented five test cases, different features of the model implementation have been verified. Overall, the model shows good agreement in all cases, often even superior to the other models that have been used for reference.

The b- Ξ flame surface wrinkling model showed insufficient quality in the performed cases.

In the partially premixed test case, the treatment of the flow as adiabatic caused noticeable deviations between the computed and the real temperature field. This was because of the cooling of parts of the experimental setup. It is not expected to be a source of error in the following simulations of the CIVB, because this is mainly a phenomenon which happens in the core flow without being influenced by the presence of walls.

7. Combustion Induced Vortex Breakdown in Free Vortices

This chapter is devoted to the investigation of the driving physical mechanisms behind CIVB in a free straight vortex. These were examined on numerical simulations of a flame flashback event. Global characteristics of the flashback could be compared to experimental results. The experimental setup and the results will be presented in this chapter as well. Unfortunately, time resolved measurements of small scale details of the flow field were not available, so that the numerical simulation was the only source of information in this context.

7.1. Object of Investigation

A premixed flame propagation along an unconfined, straight vortex is investigated. The vortex was steady and fully turbulent and had a strong inner axial flow. This axial jet was ejected by a swirl generation device based on the “movable block” design by Leuckel [53]. The principal idea behind this design is to change the cross section areas of radial and tangential flow channels by moving a movable prismatic block between fixed blocks. This is illustrated in figure 7.1. By moving the cross hatched blocks counterclockwise, the radial channels are narrowed while the tangential channels are widened. In the maximum swirl configuration, the radial channels are completely closed. After passing the blocks, the flow is deflected into the normal direction of the sketch plane and leaves the apparatus through a nozzle.

A three-dimensional cut-away of the whole device is shown in figure 7.2(b). The nozzle exit had a diameter of $D = 4.2\text{cm}$. Similar swirler designs often employ a bluff body at the nozzle center but for the present study, a conical nozzle inset has been used instead.

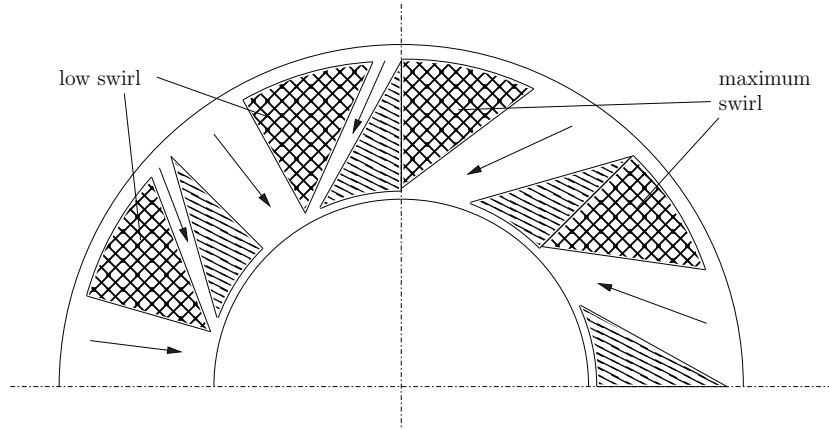


Figure 7.1.: Sketch of the movable block swirl principle. The crosshatched blocks are movable along a circular trajectory while the simply hatched blocks are fixed. Left half shows block positions for a low swirl configuration, right half illustrates the maximum swirl configuration.

Thus, the formation of a recirculation zone and a wake behind the bluff body was avoided. The axial velocities in the wake could drop below the turbulent flame speed and thus conceivably allow the flame to propagate towards the nozzle even without flame acceleration by Combustion Induced Vortex Breakdown. By avoiding the wake, a possible misinterpretation of such an event as CIVB is avoided as well.

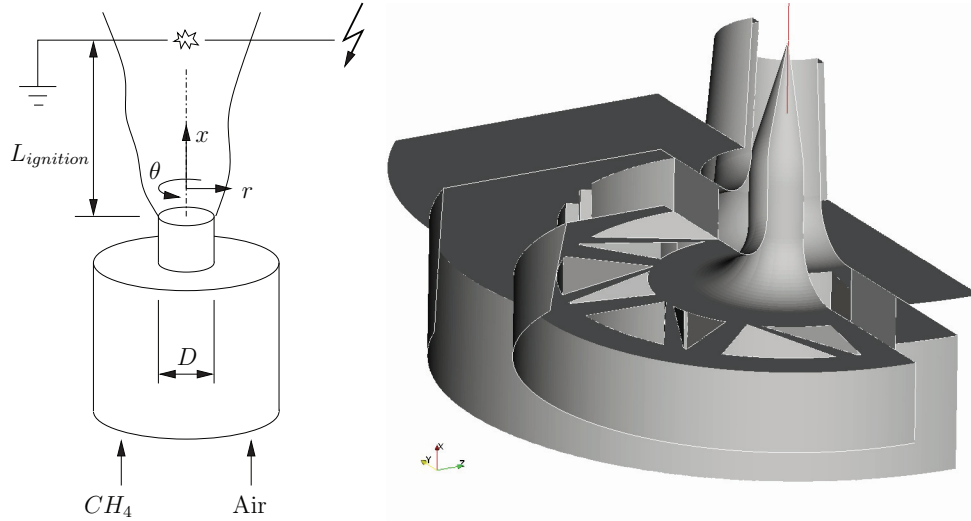
The swirl intensity is measured by the swirl number S , which is defined by

$$S = \frac{\dot{D}}{\dot{I}R_{ref}} \quad \text{with} \quad \dot{D} = \int_0^R 2\pi\rho u_{tan}u_{ax}r^2 dr \quad \dot{I} = \int_0^R 2\pi\rho u_{ax}^2 r dr \quad (7.1)$$

where R_{ref} is a reference radius and the integral is over some reference plane, which is orthogonal to the vortex axis, e.g. the nozzle exit plane of the swirl generator device. Subsequently, the nozzle radius $R_{ref} = D/2$ has been used as reference radius. The swirl number S of the applied device could be selected between $S = 0$ and $S = 2.3$.

The jet consisted of a mixture of methane and air with a selectable equivalence ratio Φ and was ejected into the ambient surrounding air.

The premixed gases was ignited at some distance $L_{ignition}$ above the swirl generator by an electric spark (see figure 7.2(a)). The flame propagation is recorded by high speed video films and also simultaneous OH-LIF/PIV measurements have been performed.



(a) Sketch of experimental setup. The vortex which was generated by the swirl generation device had a positive circumferential velocity component.

(b) Interior of the swirl generator device

Figure 7.2.: Experimental setup

In summary, the parameters of the setup were

Parameter	Value
Nozzle diameter	$D = 42\text{mm}$
Volume flux	$\dot{V} = 12 \dots 20\text{m}^3/\text{h}$
Bulk velocity	$U_{bulk} = 2.4 \dots 4.0\text{m}/\text{s}$
Reynolds number (using viscosity of air)	$Re = \frac{DU_{bulk}}{\nu} = 7073 \dots 11790$ $\nu = 1.425 \cdot 10^{-5}\text{m}^2\text{s}^{-1}$

Table 7.1.: Parameters of experimental setup for CIVB

7.2. Experimental Observations

The experimental investigation of the considered flow was not a part of the current work. The measurements were performed by Wendig [89, 90] and have been published only partially. To present a comprehensive picture of the flow, the complete measurements are reproduced in this work.

7.2.1. Isothermal Flow Characteristics

The isothermal flow fields have been measured using PIV for different values of the swirl number S and volume flux \dot{V} through the swirl generator. Especially interesting is the axial velocity because recirculation zones or vortex breakdown in the isothermal flow can convectively transport the flame which could be confused with Combustion Induced Vortex Breakdown.

Contour plots of the measured axial velocity fields are shown in table 7.2 and selected profiles of axial velocity are shown in table 7.4. It can be recognized that vortex breakdown in the isothermal flow begins to occur above a swirl number of $S > 0.49$. A strong deceleration of the flow can be observed at $S = 0.55$ and reversal of the axial velocity has occurred at $S = 0.61$.

Furthermore, the flow patterns are similar at the same swirl number for different volume fluxes. The same holds for the velocity RMS, which is shown in table 7.3.

For defining the boundary conditions in the numerical simulations below, information about the integral length scale is required. This can be estimated from the PIV data as well. The integral length is defined as the integral over the normalized autocorrelation function (see e.g. [75])

$$L_{ii} = \int_0^{\infty} R_{ii}(r) dr \quad \text{with} \quad R_{ii}(r) = \frac{\langle u_i(\vec{x}_0) u_i(\vec{x}_0 + r\vec{e}_i) \rangle}{\langle u_i(\vec{x}_0)^2 \rangle} \quad (7.2)$$

These autocorrelation functions were calculated in streamwise and lateral directions from a time series of 400 PIV snapshots. In figure 7.3, the resulting functions are shown together with the calculated integral lengths.

Reliability of the Experimental Results

A number of error sources influence the accuracy of the measurements. In principle, a distinction can be made between errors in measurement procedure itself and errors in the flow boundary conditions. The PIV measurement procedure includes the following potential sources of error:

7. Combustion Induced Vortex Breakdown in Free Vortices

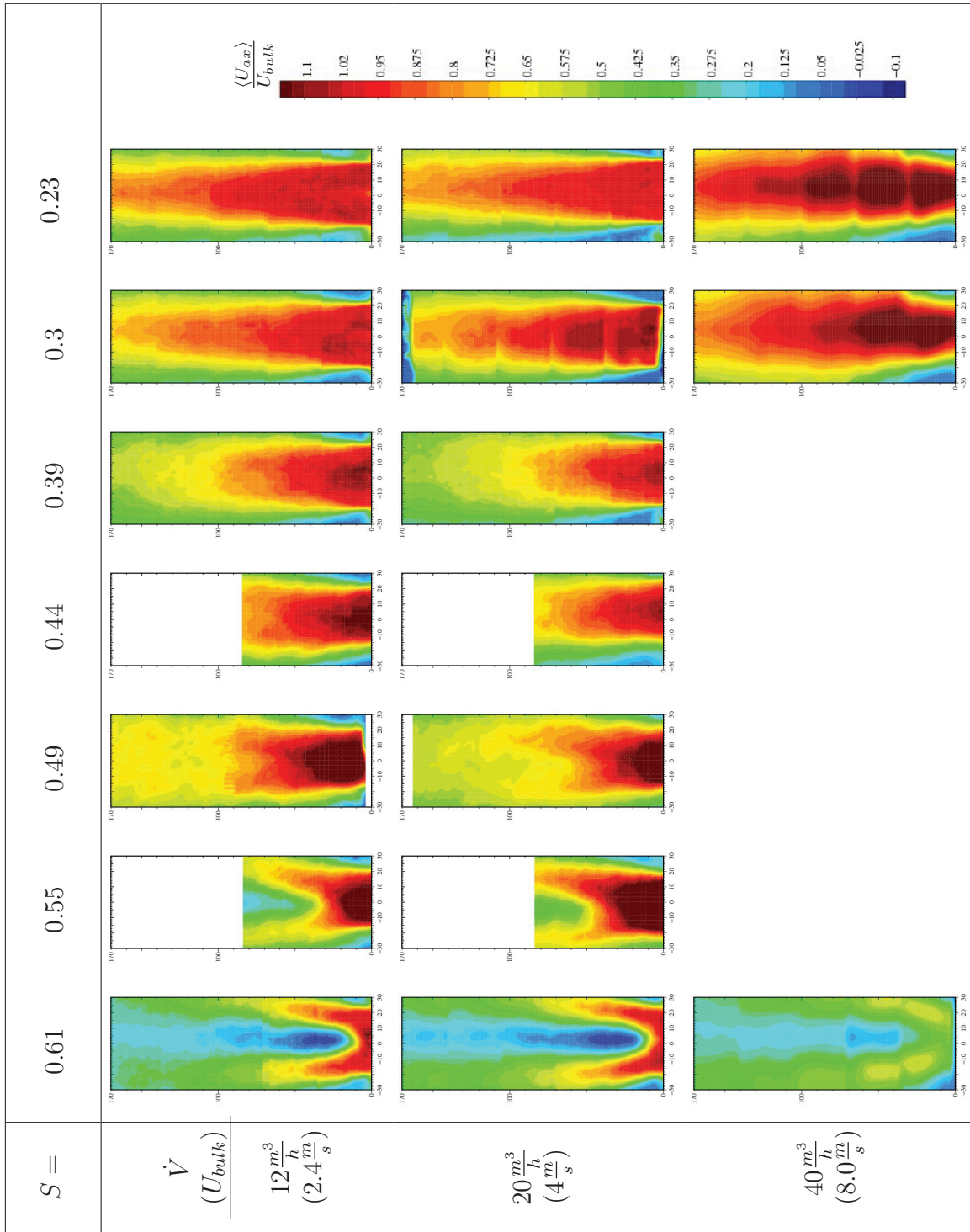


Table 7.2.: Contour plots of axial velocity in isothermal flows at different swirl intensities and volume fluxes

7. Combustion Induced Vortex Breakdown in Free Vortices

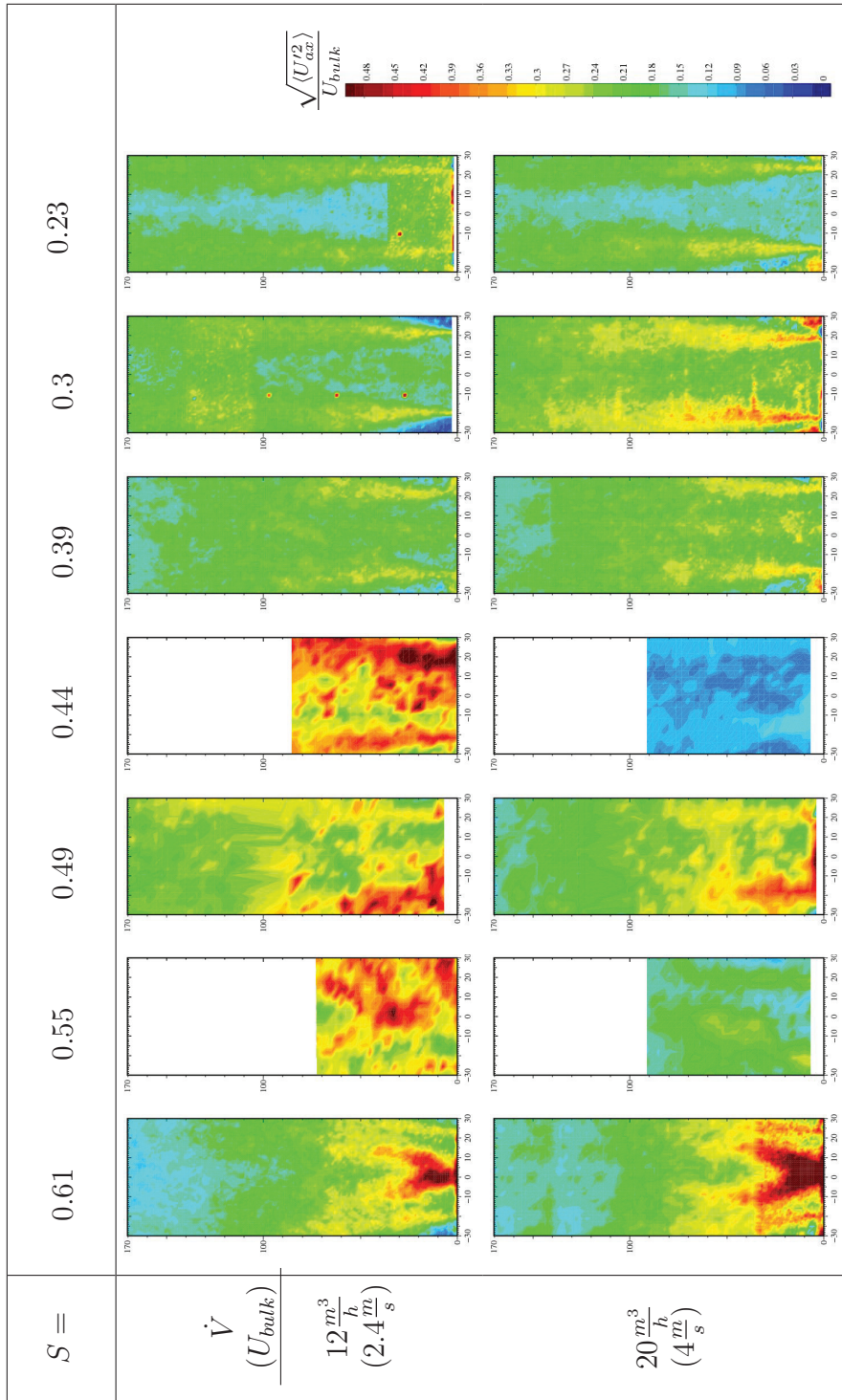


Table 7.3.: Contour plots of RMS of axial velocity in isothermal flows at different swirl intensities and volume fluxes

7. Combustion Induced Vortex Breakdown in Free Vortices

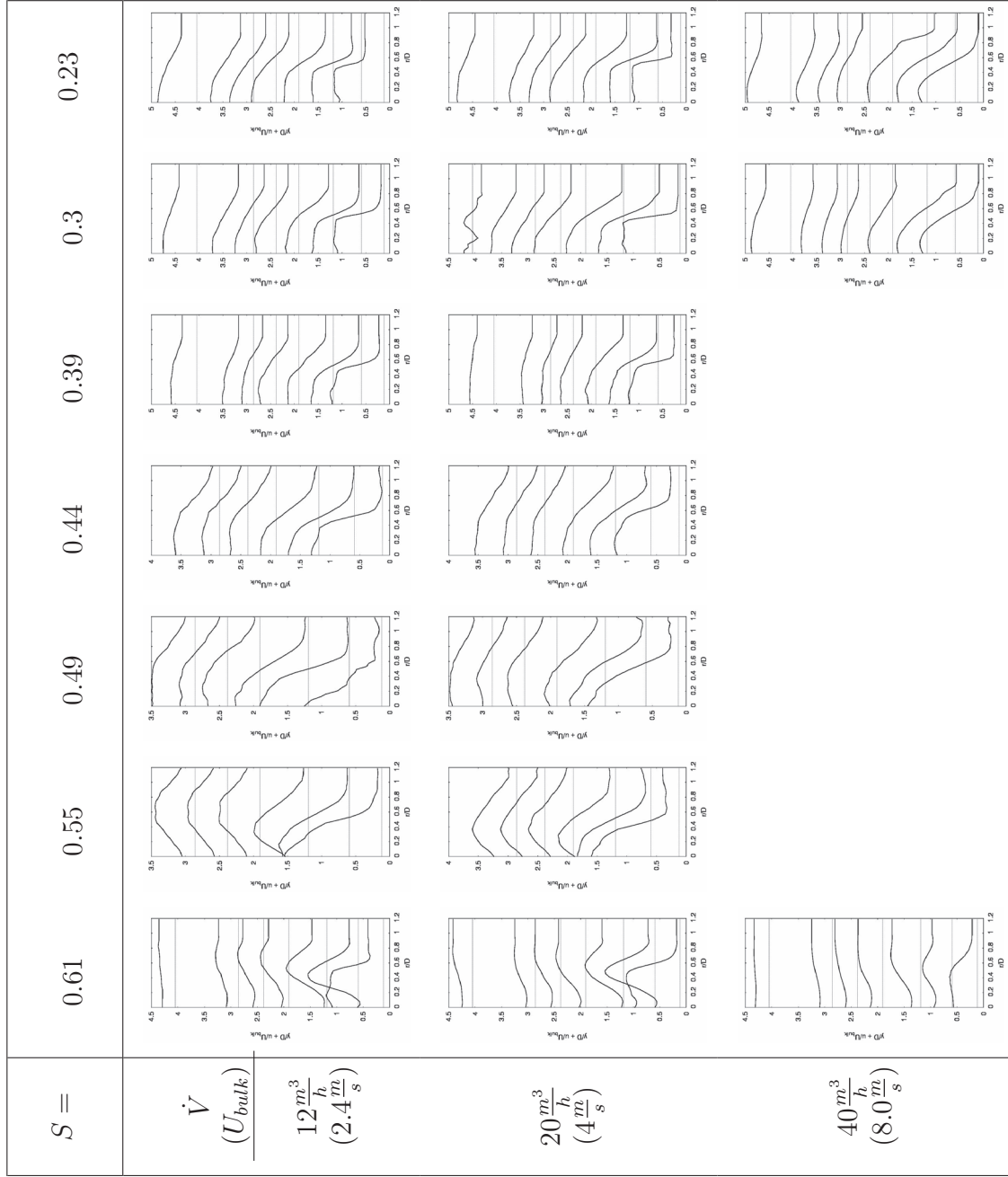


Table 7.4.: Profiles of axial velocity in isothermal flows at different swirl intensities and volume fluxes. Plotted are profiles of $y/D + \langle U_{ax} \rangle / U_{bulk}$ over r/D .

7. Combustion Induced Vortex Breakdown in Free Vortices

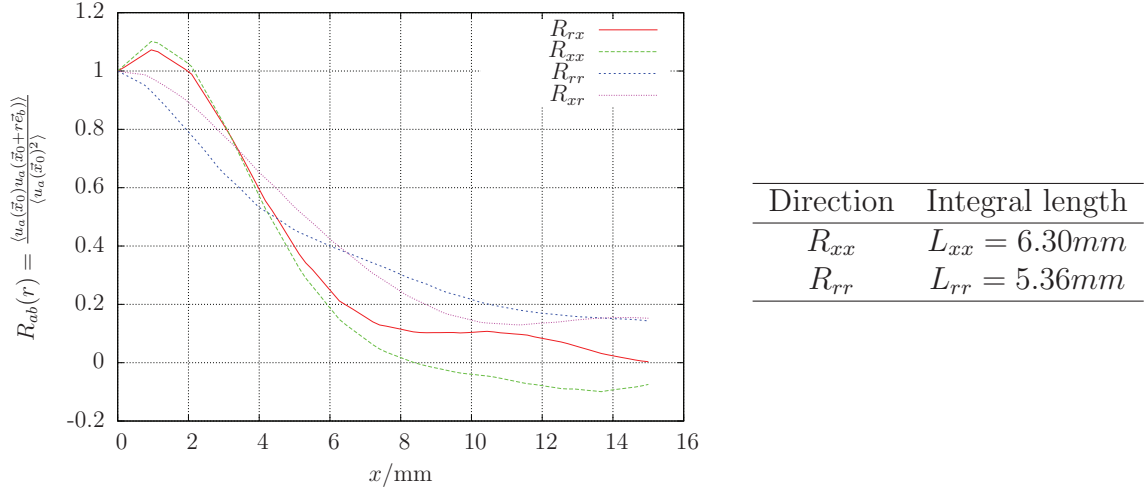


Figure 7.3.: Autocorrelation functions in isothermal velocity field. The autocorrelation function in axial direction is sampled from 5mm to 20mm above the nozzle at $r = 10mm$. The autocorrelation function in radial direction is computed from $r = 20mm$ to $r = 5mm$ at 5mm above the nozzle.

1. the time scale of the image recording camera: this is only determined by the recording hardware and most probably very accurate compared to the following points,
2. the calibration of the length scale in the recorded pictures: this was done by photographing a piece of graph paper using the PIV image recorder and setting reference points in the evaluation software,
3. the PIV analysis algorithm: the quality of the recorded raw pictures, the setting of the optics and the particle density may affect primarily the number of “outliers” and thus especially the second order statistics,
4. the position of the laser light sheet: an accidentally excentrically aligned laser light sheet may affect the comparability between experimental and simulation data.

Even larger uncertainties arise due to possible errors in the flow boundary conditions:

5. disturbance of the flow by the seeding particles: the influence on the flow by presence of the seeding particles is certainly negligible. But the particles are carried by a second gas stream which is mixed into the main stream immediately upstream of the swirler nozzle. The secondary stream was only active during PIV measurements but not while recording the flame propagation using high speed video films.

7. Combustion Induced Vortex Breakdown in Free Vortices

The velocity profile in the nozzle exit area may thus deviate from the velocity profile of the undisturbed swirler,

6. stability of the gas volume fluxes: this is the most problematic error source since no closed loop mass flow controllers had been used. The mass flows have been adjusted only occasionally during the measurement campaigns,
7. accuracy of the swirl selector: the swirl selection worked by rotating the movable blocks inside the swirl generator device. This was archived by actuating a manual leverage. The entire swirl number range of $S = 0 \dots 2.3$ was covered by an angular range of 60° . The motion of the leverage's shaft was transmitted by a reduction gearing to the movable block shaft which possesses a certain amount of backlash.

Unfortunately, none of the former error sources was quantified. But an approximate qualitative ranking could be established because of the experiences during the analysis of the experimental results:

- After consistency checks of the measured axial velocity fields, it seems that point 6 is a really striking problem. Integration of the measured axial velocity profile yielded pronounced deviations from the nominal values.
- Also point 3 seems to apply. This is supposed because of the results in table 7.3. At least the measurements for swirl number $S = 0.44 \dots 0.55$ are very noisy compared to the other measurements. This is unfortunate, because this swirl number region is of special interest. The transition from the undisturbed axial jet to isothermal vortex breakdown occurs in this range.
- Especially the repeatability of the flashback events might suffer from point 7. As will be shown later, the numerical analysis predicts a strong dependency of the flame propagation velocity from the swirl number. The error in the swirl number settings could not be quantified, since circumferential velocities had not been recorded routinely during the characterization of the isothermal flow.

7.2.2. Flame Propagation

Experiments show that flame propagation against the main flow direction and towards the swirler nozzle can happen under certain circumstances. This event will be denoted as

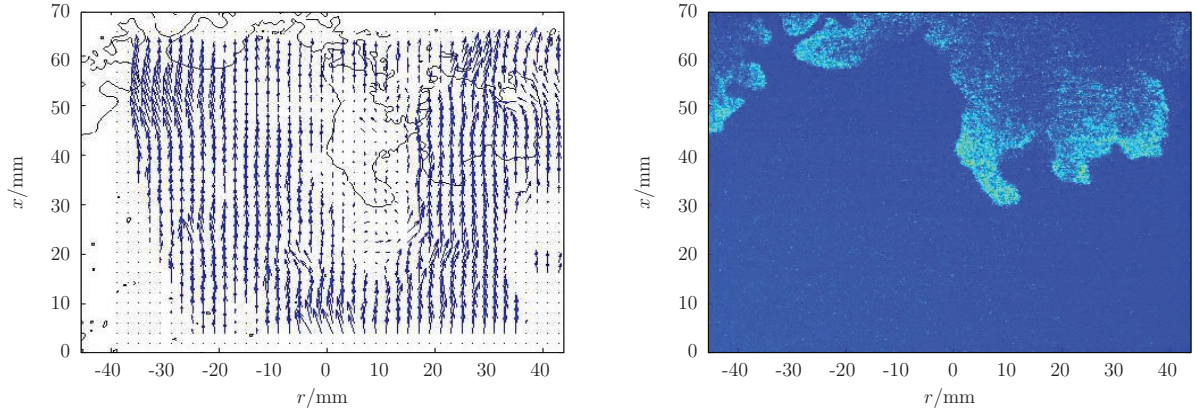


Figure 7.4.: Simultaneous PIV/LIF snapshots of propagating flame during CIVB at $\dot{V} = 12\text{m}^3/\text{h}$ and $S = 0.49$. The left image shows isocontours of OH-concentration together with velocity vectors from PIV. The right image shows the corresponding raw OH-LIF image.

“flame flashback” henceforth. Different modes of flame flashback can be distinguished. Even if no swirl is present, the flame can propagate upstream if the mixture is very rich ($\lambda < 0.8$). In this case, the propagation velocity is rather low and of the order of turbulent flame speed. High speed video films of these events indicate that the flame burns along the outer boundary of the vortical jet where the axial velocities are low. Because of the very rich mixture, fuel diffuses also into these regions and makes them rich enough to burn. No vortex dynamics and remarkable flame acceleration is involved in this case and it is of no further interest in this work.

The focus is instead on cases with a medium swirl number but without remarkable flow deceleration or even vortex breakdown in the isothermal flow. From table 7.2 it can be seen that this is the case for $S \leq 0.49$. If a flame is ignited above the swirl generator nozzle at these swirl numbers, it would be expected that it is blown downstream, because the flow velocities everywhere exceed the turbulent flame speed. This shall be illustrated by some simple estimations.

A very simple approximation for the turbulent flame speed is:

$$\frac{s_T}{s_L} = 1 + \frac{u'}{s_L} \quad (7.3)$$

From the PIV measurements in table 7.3 it is seen that the RMS and mean velocity level largely depends on the volume flux. For the two volume fluxes relevant in this

7. Combustion Induced Vortex Breakdown in Free Vortices

work, the following mean velocity and RMS levels are regarded in the ignition zone at $x = 12cm$.

Volume flux	Velocity RMS	Mean velocity
$\dot{V} = 12m^3/h$	$u' \approx 0.5m/s$	$U_x \approx 1.5m/s$
$\dot{V} = 20m^3/h$	$u' \approx 1.0m/s$	$U_x \approx 2.4m/s$

Table 7.5.: Levels of velocity mean and RMS in CIVB setup

Although table 7.3 indicates higher RMS levels for the region between $S \geq 0.44$ and $S \leq 0.55$ this is almost certainly due to the bad quality of the measurements there. At these conditions only a low number of samples were used for the statistics. The real RMS level is probably as indicated in table 7.5.

To derive an upper limit for the turbulent flame speed, the largest possible laminar flame speed will be used to evaluate (7.3). The laminar flame speed is maximum for a slightly lean mixture. For methane/air $s_{L,max}(\Phi = 1.15) = 0.42m/s$ (e.g. [36] or figure 3.2). From the above estimations, it follows that the turbulent flame speed in the current case is:

Volume flux	Turbulent flame speed
$\dot{V} = 12m^3/h$	$s_T < 0.92m/s$
$\dot{V} = 20m^3/h$	$s_T < 1.42m/s$

Table 7.6.: Estimated turbulent flame speed in CIVB setup

With the investigated setup (ignition height $2.85d_n$) flame flashbacks can be observed when $S \geq 0.39$ at slightly lean mixtures. At that conditions, the mean axial velocities still exceed the turbulent flame speed by 60% ($12m^3/h$) and 70% ($20m^3/h$). But despite this, flame propagation with a velocity $v_f \approx 0.33m/s$ towards the nozzle was observed in experiments with a stoichiometric mixture at $S = 0.39$.

7.3. LES Simulation of Flashback Event

Since only integral parameters of the flashback event could be retrieved from experiments, numerical simulations were performed to get a deeper insight into the flow physics. The following section describes the numerical model, i.e. grid and boundary

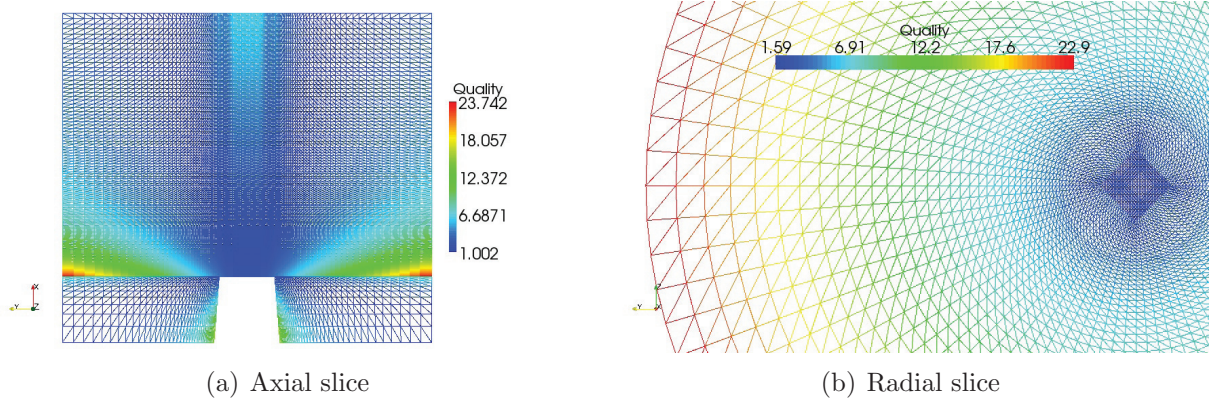


Figure 7.5.: Grid for simulation of isothermal and reacting flows. The quad elements are triangulated for visualization. The colors denote mesh quality based on edge length ratio. Best quality has value 1.

conditions, the simulations of the isothermal flow and simulations of flashback events using the presumed-PDF model.

7.3.1. Grid and Boundary Conditions

The domain for the numerical simulation of the flame flashback had a cylindrical shape with a diameter of $6.66d_n$ and length in axial direction of $4.7d_n$. The computational domain of the combustion simulations did not include the interior of the swirl generator device. Instead, the domain began at the nozzle exit plane and the velocity profile was prescribed there. The mesh was purely hexahedral with a block structured layout. The mesh contained about 600 000 cells and the cell edge length in the interesting region was about $\Delta \approx 1mm$. Slices of the grid together with a measure of the grid quality are shown in figure 7.5. The figures show a satisfactory mesh quality in the region above the nozzle which gets worse with increasing distance. A measure for the resolution of the flame front is the ratio of LES filter width to flame thickness Δ/δ_L . A plot of this ratio along the geometric centerline is shown in figure 7.6. Up to the utilized ignition point at $x = 12cm$ ($x/D = 2.85$) this ratio rises up to 6. Since the test cases from chapter 6 showed good results for this resolution it is regarded as sufficient.

Since turbulent fluctuations are partly resolved in Large Eddy Simulation, it is also required to prescribe turbulent fluctuations at the inflow boundaries. Therefore, the method of turbulent spots [49] was used. The mean velocity profiles were gained from

7. Combustion Induced Vortex Breakdown in Free Vortices

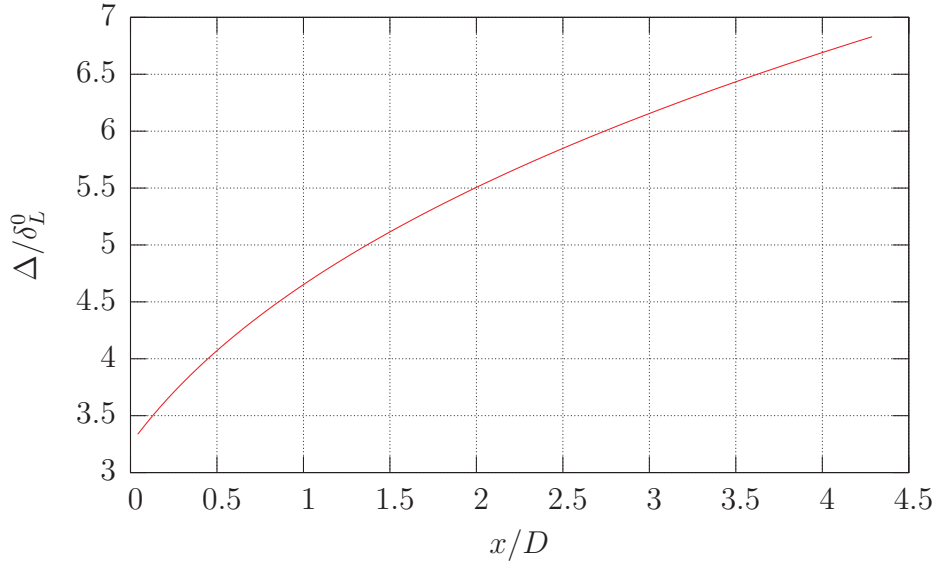


Figure 7.6.: Ratio of LES filter width to laminar flame thickness vs. distance from nozzle along centerline. The laminar flame thickness of a stoichiometric CH_4 /air flame has been used and the filter width was calculated as the cube root of a cells volume $\Delta = \sqrt[3]{V}$.

auxiliary simulations of the swirl generator device and checked against experimental measurements of the isothermal flow. For the method of turbulent spots, velocity RMS and length scales or autocorrelation functions are required as input. In this case, the RMS and length scales were also gained from experimental data.

It turned out, that it was necessary to apply non-reflecting boundary conditions for pressure at the lateral and outflow boundaries. Since the code is compressible, pressure waves appear at the ignition point during the ignition phase and propagate through the computational domain. The non-reflecting boundary condition allows them to leave the domain without influencing the flow field upstream.

The flashback simulation was started from the isothermal flow by igniting the mixture on the centerline at $2.4d_n$ above the nozzle. No attempt was made to model the ignition process in detail. The ignition was modeled by introducing artificial source terms into the progress variable transport equations, in the same way as it was already done in the combustion bomb test case in section 6.2.

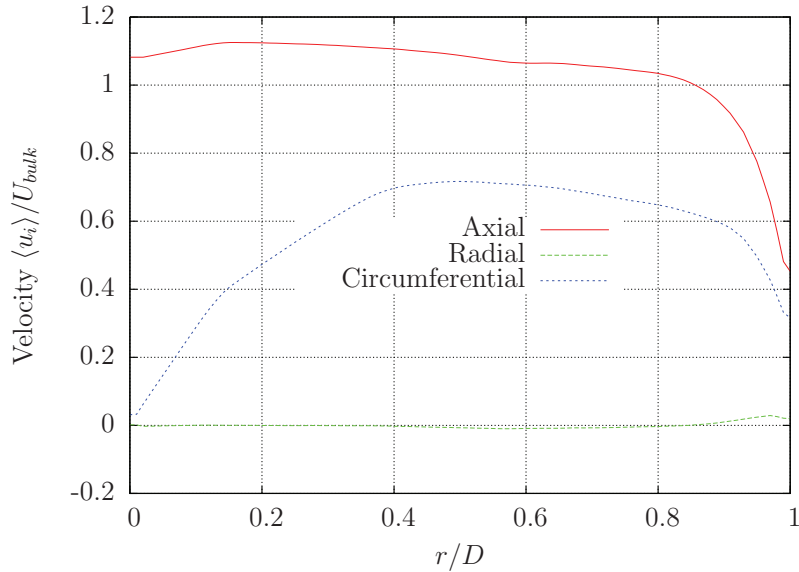


Figure 7.7.: Mean inflow velocity profiles for case $S = 0.39$, $\dot{V} = 12m^3/h$

7.3.2. Simulation of Isothermal Flow

For a successful modelling of the reacting flow during the flame flashback, it is essential that the isothermal flow is reproduced right by the numerical model described above. Therefore, Large-Eddy Simulations of the isothermal flow have been carried out at different swirl numbers and volume fluxes.

As mentioned above, the mean velocities are needed for all cases to be specified at the inlet plane. While axial and radial velocity profiles are available for all cases, the circumferential velocity profile could not be gathered from the PIV measurement campaign.

For a single case with a swirl number of $S = 0.39$ and a volume flux of $\dot{V} = 12m^3/h$, measurements with a two-component LDV were performed and yielded profiles of axial and circumferential velocity. These were compared against a steady RANS simulation and a LES of the whole swirl generation device. The RANS simulation could not reproduce the profiles properly but the LES results fitted well. Furthermore, RANS simulations at different volume fluxes indicated an approximately linear scaling of the velocity profiles with volume flux.

The profiles of the swirl generator LES are shown in figure 7.7 For all subsequent simulations, the profiles from figure 7.7 have been used. For cases with different volume fluxes

7. Combustion Induced Vortex Breakdown in Free Vortices

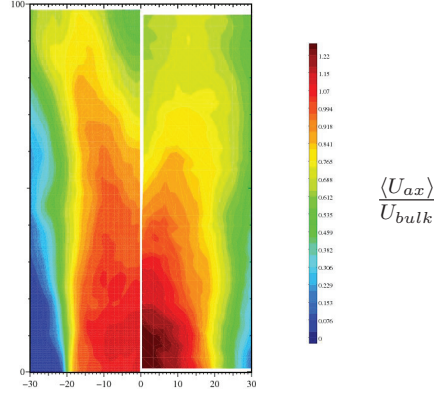


Figure 7.8.: Comparison of LES with modified boundary conditions for $S = 0.49$. Left half shows LES ($\dot{V} = 20\text{m}^3/h$), right half shows PIV.

or swirl numbers, the axial component or the circumferential and radial component were scaled by a constant factor.

The results of the isothermal LES calculations are shown in table 7.7. The agreement between LES and experimental data is generally good for medium swirl numbers $S \leq 0.39$ and also the high swirl case with vortex breakdown in the isothermal flow at $S = 0.61$ is well reproduced. However, in the intermediate case at $S = 0.49$, noticeable deviations occur. This might be because the flow pattern at these swirl number is very sensitive to the boundary conditions and the scaling of especially the circumferential velocity profile by a constant factor does not result in fully appropriate inflow conditions. The measured flow pattern for $S = 0.49$ is better reproduced by the LES, if the inlet profiles are scaled according to a swirl number of $S = 0.41$. The comparison for this case is shown in figure 7.8. These boundary conditions have been used henceforth for simulations of the cases with a swirl number of $S = 0.49$.

Since the vortex tube under consideration is unconfined, entrainment of surrounding air into the vortex occurs. Figure 7.9 shows the variation of the local air equivalence ratio along the vortex centerline in axial direction. The profiles are not very smooth because no averaging over homogeneous directions could be done and computational resources were limited during the isothermal flow study. But anyway, the trend is visible: from $x/D \approx 1.5$ on, a considerable entrainment of air occurs. It begins a little more upstream for the lower volume flux cases than for the higher volume flux cases.

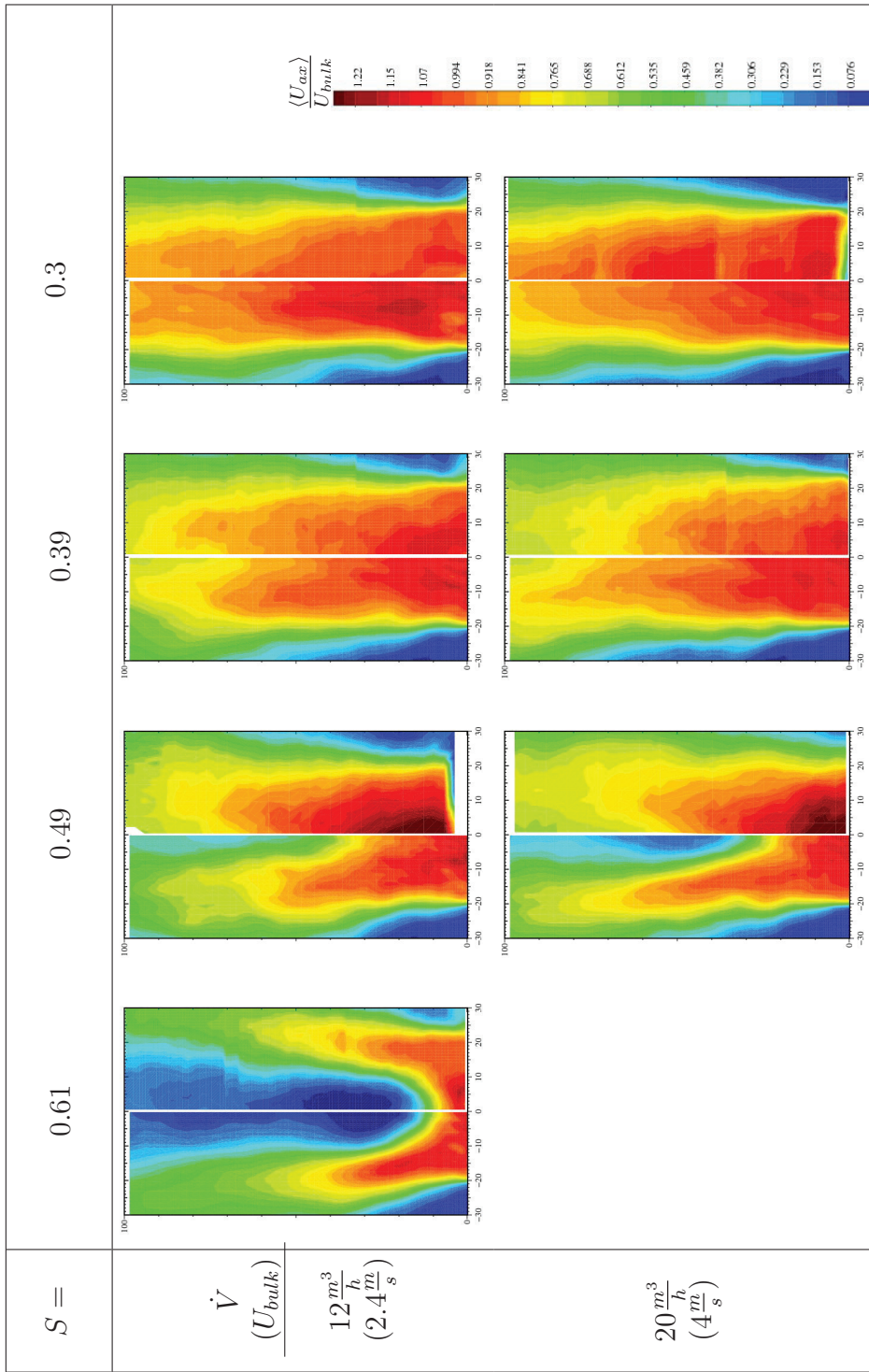


Table 7.7.: Contour plots of axial velocity in isothermal flows at different swirl intensities and volume fluxes. Left half of the contour plots shows LES, right half shows PIV.

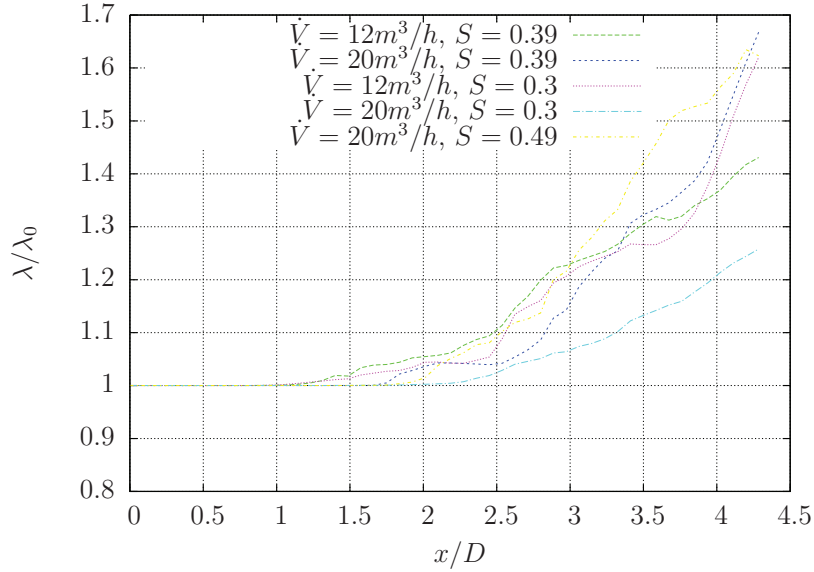


Figure 7.9.: Effect of air entrainment: local air equivalence ratio λ from LES of isothermal flow

7.3.3. Prediction of Flashback Limits

For a given swirl number, flame flashbacks occur below a critical value of the air equivalence ratio λ . The critical equivalence ratio depends on volume flux as well as on ignition height. The latter is most probably because of the varying equivalence ratio due to air entrainment (see 7.9). The limits for the equivalence ratio have not been investigated extensively in experiments but only for selected conditions.

Figure 7.10 shows the limiting curves for two different ignition heights $x/D = 2.85$ ($x = 12\text{cm}$) and $x/D = 4.28$ ($x = 18\text{cm}$) at a swirl number of $S = 0.39$. The errorbars denote the estimated experimental uncertainty in air volume flux and equivalence ratio. There is another uncertainty in the swirl number but its effect on the flashback limits cannot be expressed algebraically and is therefore not visible in figure 7.10.

A number of LES runs with different equivalence ratios have been performed to check whether the experimentally recorded limits could be reproduced by the numerical simulations. Runs, where a flashback occurred, are marked with a downward pointing hollow triangle in figure 7.10, while runs without flashback are marked by an upward pointing filled triangle.

The occurrence of flame flashbacks in the simulations matched the experimental curve

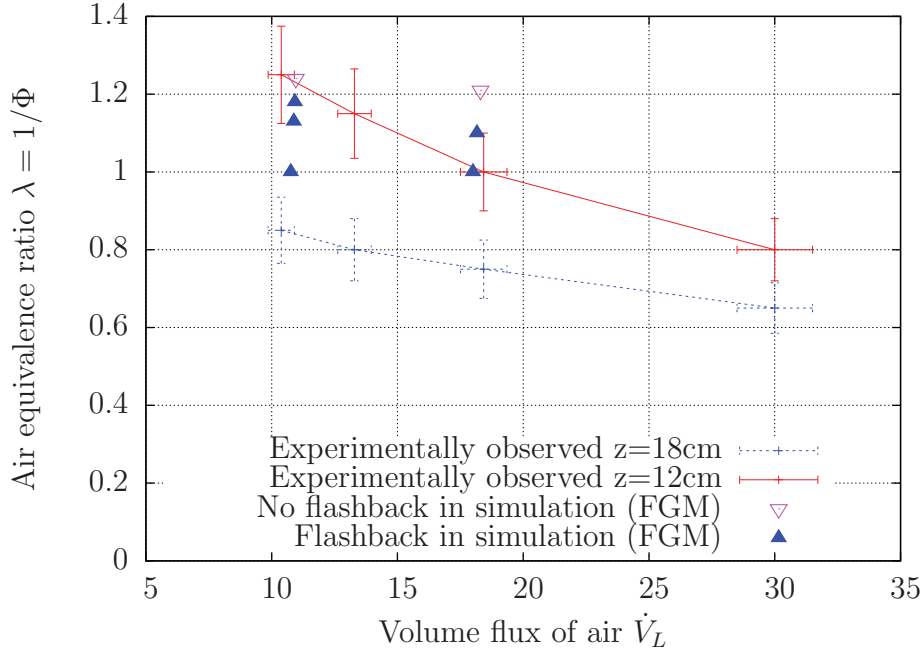


Figure 7.10.: Limiting curve for flashback occurrence in experimental apparatus for ignition heights 12cm and 18cm at swirl number $S = 0.39$. The air equivalence ratio is at the nozzle exit.

within the uncertainty bounds. For the low volume flux, the transition between stable and unstable flow occurs at the same air equivalence ratio like in the experiments. For the higher volume flux case, the simulated transition is shifted towards a leaner mixture. If this trend is extrapolated to higher volume fluxes, the simulated and experimentally observed flashback limits would disagree even more.

In the following section, it will become obvious that the flame propagation speed is overestimated by the numerical simulations. This could be interpreted as a hint at deficiencies in the numerical modeling which are responsible for the improper prediction of the flashback limits as well. However, Tangermann [79] performed simulation of the same case using a different combustion model. He obtained an even better agreement in terms of flame propagation speed but identical results for the flashback limits.

Label	Swirl S	Volume flux \dot{V}	Ignition height	Fuel
D10V12	0.39	$12m^3/h$	$12cm$	CH_4 ($\Phi = 1$)
D10V20	0.39	$20m^3/h$	$12cm$	CH_4 ($\Phi = 1$)
D9V20	0.49	$20m^3/h$	$12cm$	CH_4 ($\Phi = 1$)

Table 7.8.: Overview on performed simulations

7.3.4. Detailed Analysis of Vortex Dynamics During the Flashback Event

In this section, a detailed analysis of single flashback incidents will be attempted. Some specific configurations have been chosen therefore. An overview of the simulations under investigation is given in table 7.8. All cases have been simulated at a stoichiometric mixture because the flashback limits in figure 7.10 indicate that flashback events will then certainly occur at the selected swirl numbers. Two simulations were performed at the same swirl number with different volume fluxes and two simulations had identical volume flux with different swirl numbers.

For the evaluation of the results, at first the location of the flame tip is searched at each time step. This is done by searching the temperature jump along the geometric centerline of the apparatus. The threshold for the flame detection was $T = 1000K$. The history of the flame tip distance from the swirler nozzle vs. time for all simulations is shown in figure 7.11(c). Although the isothermal velocity field changes with increasing distance from the swirler nozzle, the propagation velocity seems to remain constant in principle. It is also remarkable that the flame propagation velocity is only weakly dependent on the volume flux but very strongly on the swirl number.

Experimental data for the flame tip locations was provided only for the two cases D9V20 and D10V12. It is shown by the blue symbols with bars in figures 7.11(a) and 7.11(b). The flame tip locations were evaluated from high speed video films. The bars show RMS in the flame tip location during the average over 30 runs each. From a linear regression analysis of the high speed film and LES data, the flame propagation speeds can be estimated and are reported in table 7.9.

Although the computed trajectory lies within the experimental fluctuation range, the simulation overestimates the flame propagation speed. But it should be kept in mind that there is also uncertainty in the experimental boundary conditions. Especially the

7. Combustion Induced Vortex Breakdown in Free Vortices

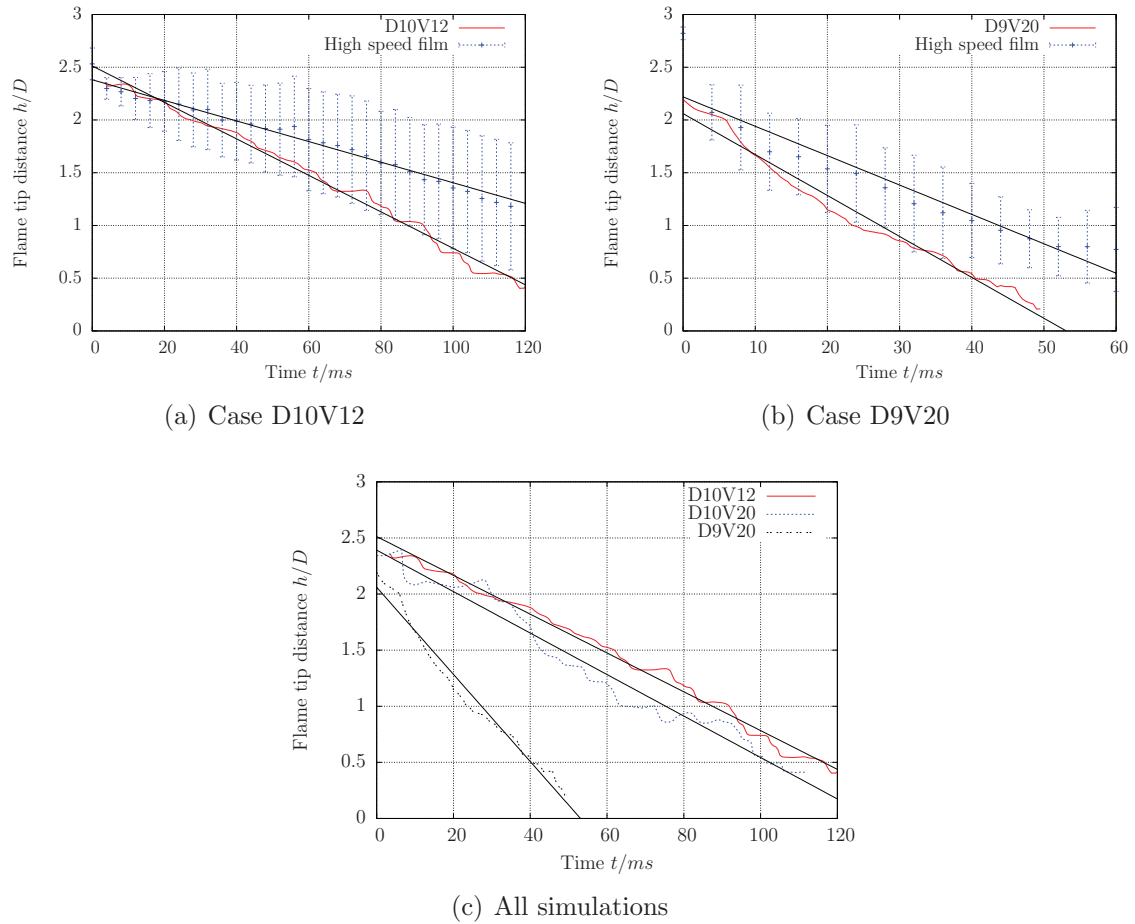


Figure 7.11.: Plots of flame tip to nozzle distance vs. time together with their linear regressions (solid black lines). Red solid lines: data from LES run, Blue symbols with error bars: average over 30 experimental runs, the bars show RMS.

7. Combustion Induced Vortex Breakdown in Free Vortices

Case	Simulated propagation speed	Propagation speed from exp.
D10V12	0.726167 <i>m/s</i>	(0.45 <i>m/s</i>)
D10V20	0.776238 <i>m/s</i>	–
D9V20	1.63006 <i>m/s</i>	(1.17 <i>m/s</i>)

Table 7.9.: Flame propagation speeds during CIVB. Propagation speeds are obtained from linear regression of flame tip to nozzle distance vs. time.

swirl number was set by a manual leverage with a coarse scale and the error in the swirl number was not quantified.

The flashback is a stochastic event and only single incidents have been simulated. Ensemble averaging over a large number of simulations for all cases would be needed to draw formally correct conclusions, each with different initial conditions. This is unfeasible because of the too large computational effort. Furthermore, larger perturbations of the flow occurred in the experiments due to disturbances in the laboratory environment which were not present in the simulations and thus averaging of the experimental runs was required to gain useful data at all. Experiences with different simulations gave rise to the assumption that the simulated flame propagation is much less fluctuating than the flame propagation in our experimental setup.

Nonetheless, it is visible from figure 7.11, that the observations reported in section 7.2 are basically reproduced in the numerical simulation.

To investigate the flow field in more detail, some kind of averaging is desired. Ensemble averaging is unfeasible but averaging in a flame tip fixed coordinate system is possible. That means, the time averaging is not done at fixed locations in space, i.e. cell centers in the space fixed computational grid, but at points that are fixed relative to the flame tip. The averaging is still done in time, so stationarity in this moving frame of reference is required. It does not strictly imply axisymmetry because no averaging over circumferential directions is included so far. Though, rotating or precessing structures would violate the assumption of stationarity. Furthermore, the velocity field and mixture properties should be homogeneous along the path of the flame for application of this averaging procedure. This is not strictly fulfilled in the current case, but the averaging is done this way nonetheless simply because not more data were available. It is therefore expected that the rendered picture is not sharp but rather blurred but still contains valuable information to get a deeper insight into physics of the process under consideration.

7. Combustion Induced Vortex Breakdown in Free Vortices

Technically, a cubical mesh, smaller than the entire domain, with a size of $4\text{cm} \times 4\text{cm} \times 4\text{cm}$ and a resolution $32 \times 32 \times 32$ cells was used for further analysis. For each time step, the center of this cube was shifted to the according flame tip location and all fields were mapped onto it. By doing so, the fields were spatially transformed into the moving flame tip fixed coordinate system and the amount of data was reduced to speed up subsequent computation of deduced quantities but time dependence was retained. All subsequent analysis were performed on this cutout. The flame tip fixed average could be computed simply as the time average over all cells of this grid.

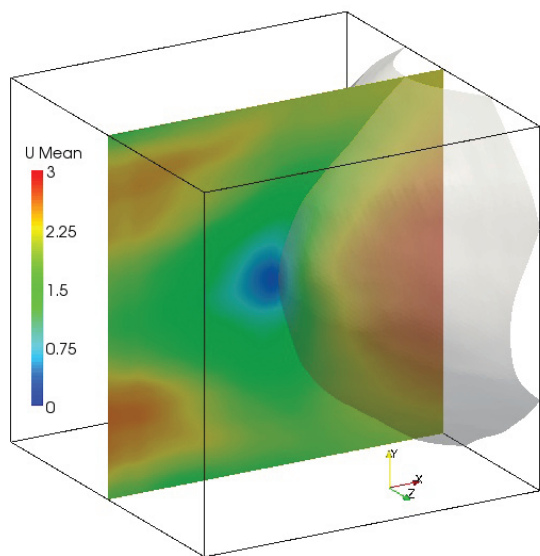
If deduced quantities were to be evaluated, like vorticity or the vorticity production terms, they have been computed from the unaveraged raw data for each time step first and the result was then averaged afterwards.

The averaged velocity field for the three cases is shown in figure 7.12. The pictures show a slice through the mean velocity field together with a slightly transparent isosurface in the averaged temperature field. The latter gives an impression of the average flame front shape. For the higher swirl case D9V20, the flame shape is slightly more conical and spiky than for the lower swirl cases D10V12 and D10V20. Furthermore, it is easily recognized that there exists a spot in front of the flame tip, where the axial velocity is strongly decelerated. This deceleration is stronger and the extent of the low velocity region is larger in the high swirl case D9V20 than in the other two cases. It seems obvious, that the velocity in this region allows the flame to propagate against the main flow or even causes a convection of the reacting gases towards the swirler nozzle.

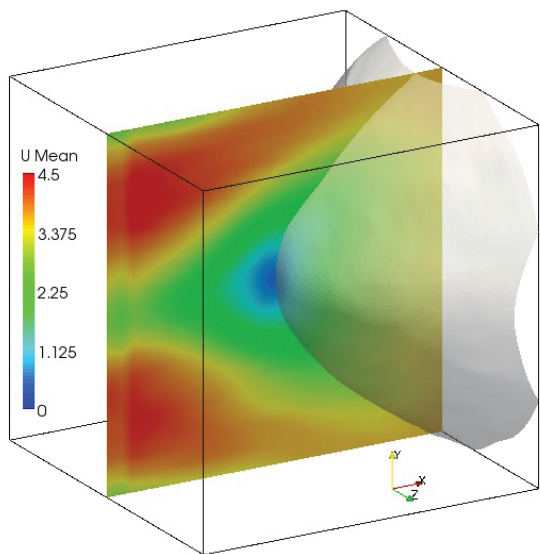
Since this spot is not present in the isothermal case, it must have been caused by the presence of the flame. As already argued in section 1.1, this is a typical feature of vortex breakdown and vortex breakdown is connected to the creation of negative circumferential vorticity, i.e. a spiraling of the vortex lines. Figure 7.13 shows the vortex lines for the three investigated cases. In all cases, the vortex lines are initially almost parallel or at least weakly spiraled but then spiral up significantly as they reach the flame front. In the D9V20 case the spiraling starts a little bit more ahead of the flame front and is stronger than in the D10V12 and D10V20 case.

As already mentioned in section 1.1, there is no common conception of whether the circumferential vorticity is created by radial expansion of the stream surfaces or a baroclinic mechanism. To learn more about the role of the different vorticity production mechanisms, the three production terms have been computed from simulation data.

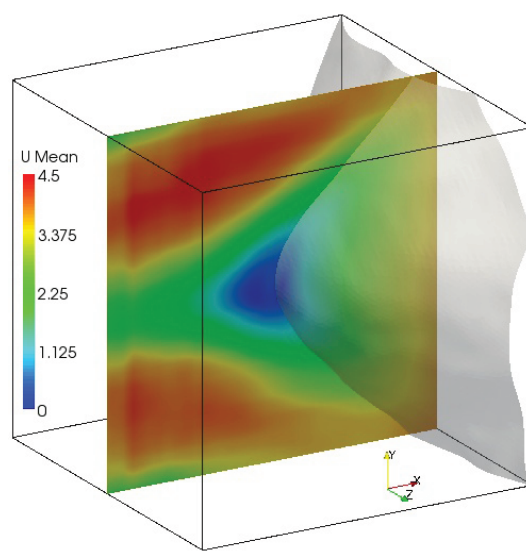
7. Combustion Induced Vortex Breakdown in Free Vortices



(a) D10V12



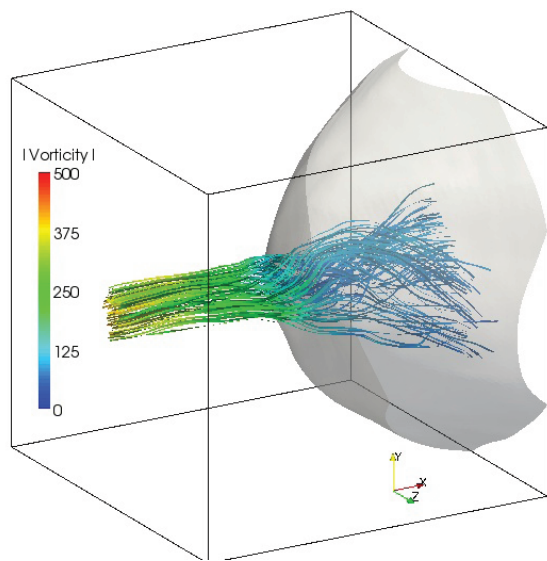
(b) D10V20



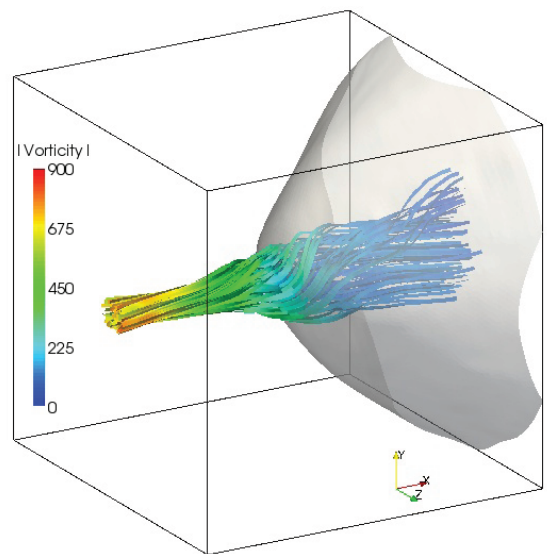
(c) D9V20

Figure 7.12.: Axial velocity field averaged in flame tip fixed coordinate system. Transparent surface: isosurface of averaged temperature $T = 1000K$.

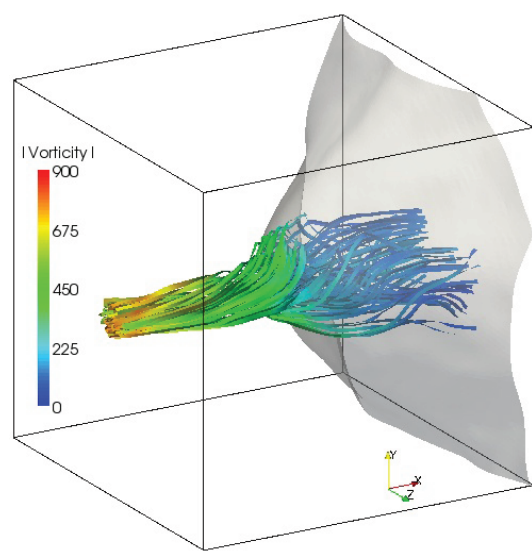
7. Combustion Induced Vortex Breakdown in Free Vortices



(a) D10V12



(b) D10V20



(c) D9V20

Figure 7.13.: Spiraling of vorticity lines at the flame front. Transparent surface: isosurface of averaged temperature $T = 1000K$.

7. Combustion Induced Vortex Breakdown in Free Vortices

Figure 7.14 show the probability density functions of the circumferential components of the production terms (see figure 7.2(a) for coordinate system conventions). What is remarkable is that all PDF's are slightly skewed towards production of negative circumferential vorticity, i.e. negative production terms appear more often than positive. The baroclinic production term has a high peak near zero and it is therefore most probable to find small values of baroclinic production.

For the low swirl cases D10V12 and D10V20, the shape of the PDF of the baroclinic term is narrower than for the high swirl case D9V20.

What is not visible from figure 7.14 is that at very large positive and negative values of the vorticity production, there is still a small but nonzero probability for the baroclinic production mechanism. This is probably attributed to a small number of very strong incidents like strong turbulent vortices interacting with the flame front. It remains unclear at this stage, whether this is also physically sound or merely a numerical issue.

The vorticity does not act locally but induces a velocity in the whole domain according to Biot-Savart's law:

$$\vec{u}_{ind}(\vec{x}) = \frac{1}{4\pi} \int_{(V)} \frac{\vec{\omega}(\vec{x} - \vec{r}, t) \times (\vec{x} - \vec{r})}{|\vec{x} - \vec{r}|^3} dV \quad (7.4)$$

where \vec{x} determines the point where the velocity is calculated and \vec{r} is the radius vector of the elementary vortex. Differentiating (7.4) with respect to time and taking equation (1.1) into account we obtain the induced accelerations caused by the three different physical mechanisms:

$$\begin{aligned} \frac{d\vec{u}_{ind}}{dt} = & \frac{1}{4\pi} \int_{(V)} \frac{[-\vec{\omega}(\nabla \cdot \vec{u})] \times \vec{r}^*}{|\vec{r}^*|^3} dV \\ & + \frac{1}{4\pi} \int_{(V)} \frac{\left[\frac{1}{\rho^2} \nabla \rho \times \nabla p \right] \times \vec{r}^*}{|\vec{r}^*|^3} dV + \frac{1}{4\pi} \int_{(V)} \frac{[(\vec{\omega} \cdot \nabla) \vec{u}] \times \vec{r}^*}{|\vec{r}^*|^3} dV \quad (7.5) \end{aligned}$$

with $\vec{r}^* = \vec{x} - \vec{r}$.

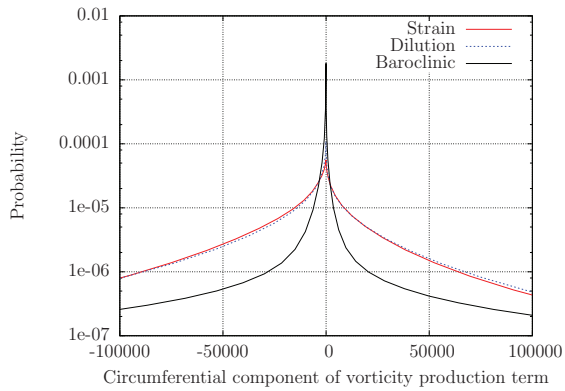
Each component of the induced acceleration is now evaluated at a number of points along the vortex axis. The numerical computation of the Biot-Savart integrals is carried

out using the method described in [12]. The result of integrating (7.5) is the axial distribution of the induced accelerations caused by the three different vorticity production mechanisms. The integration has again been done for the raw data of each time instant in the flame tip fixed coordinate system and the instantaneous axial profiles have been averaged in time afterwards. Thus, only quasi-steadiness of the induced accelerations was presumed and no kind of axisymmetry of the vorticity or its production terms.

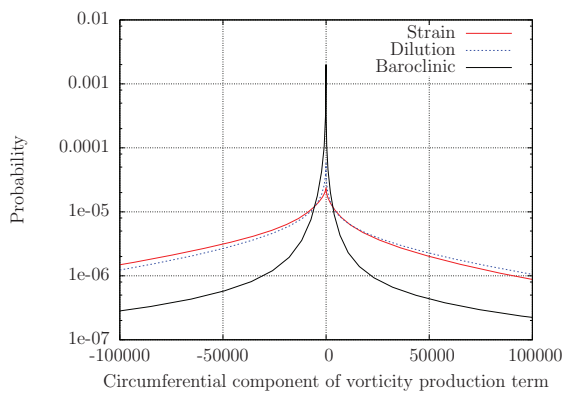
The result of integrating (7.5) is the axial distribution of the induced accelerations caused by the three different vorticity production mechanisms. This is shown in figure 7.15 for the three cases. The bars in the figures show the RMS fluctuations of the induced accelerations. It is noticeable that the baroclinic source term shows very large fluctuations in both cases. The largest fluctuations appear around the flame tip, where the density gradient has the largest values. These large fluctuations certainly arise from interactions of the pressure gradient in turbulent vortices with the flame front, which is characterized by a strong density gradient.

For better readability and easier comparison, the data from the three plots in figure 7.15 is compiled into a single plot in figure 7.16 without the RMS bars. For all cases, the net acceleration is negative ahead of the flame tip. In the low volume flux case D10V12, the net acceleration gets negative at $\Delta x/D = -0.35$ but remains only little below zero while the net acceleration gets clearly negative upstream of the flame tip for the other two cases. This means, that velocities against the main flow direction are induced and the flow is decelerated. As is apparent from figure 7.16 this is caused solely by the strain term, i.e. the widening of the stream surfaces due to the deflection of the streamlines. The volume expansion term counteracts the flame flashback as well as the baroclinic term does in the mean.

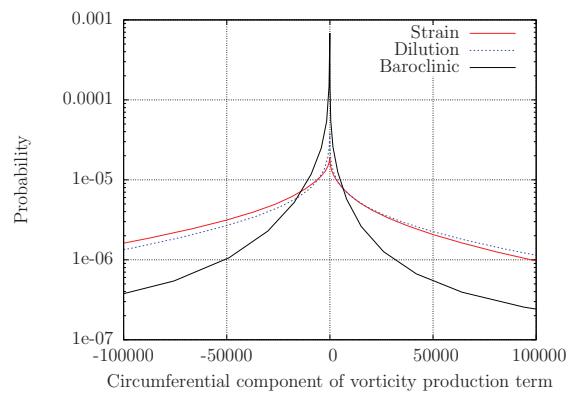
7. Combustion Induced Vortex Breakdown in Free Vortices



(a) D10V12



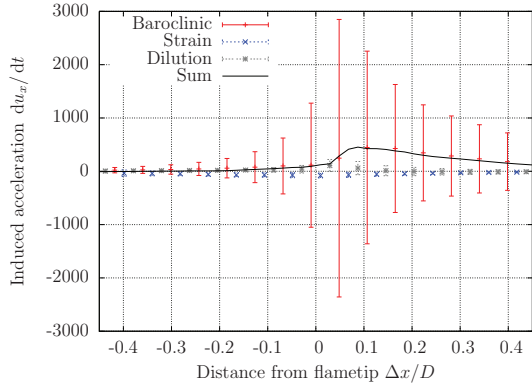
(b) D10V20



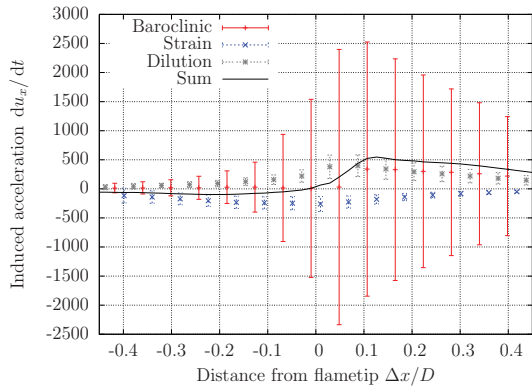
(c) D9V20

Figure 7.14.: Probability density functions of the circumferential components of the three different vorticity production terms.

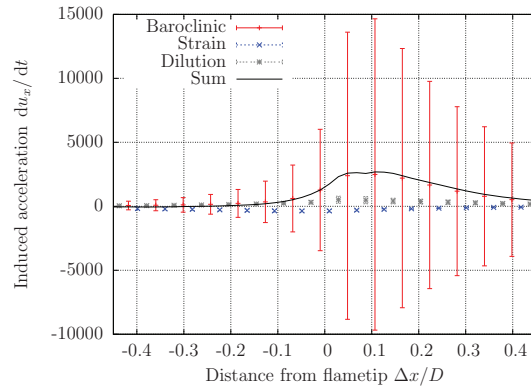
7. Combustion Induced Vortex Breakdown in Free Vortices



(a) D10V12



(b) D10V20



(c) D9V20

Figure 7.15.: Accelerations induced along the vortex centerline by the three different vorticity production terms, averaged in flame tip fixed coordinate system. Fresh gas is on the left, burnt gas on the right. The bars show RMS. Graphs of mean values without bars are shown in figure 7.16.

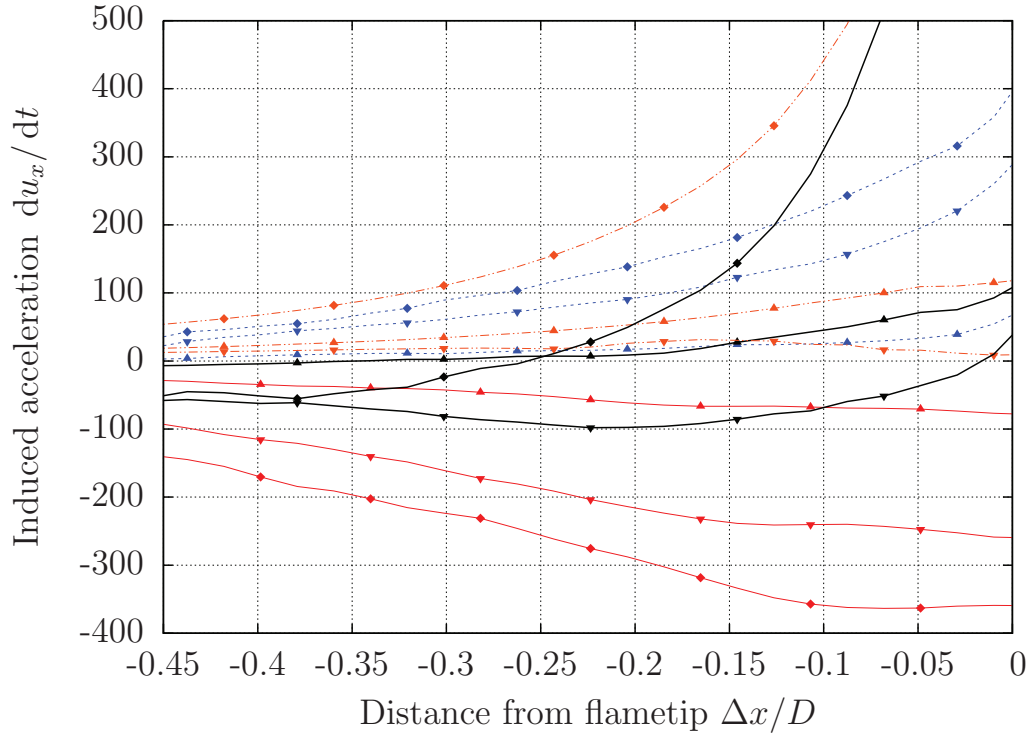


Figure 7.16.: Averaged accelerations induced along the vortex centerline by the three different vorticity production terms, averaged in flame tip fixed coordinate system. Data for all cases is shown in one plot without RMS bars. Only the induced accelerations upstream of the flame tip are shown. Symbols denote different cases: D10V12 (\blacktriangle), D10V20 (\blacktriangledown), D9V20 (\blacklozenge). Different line types denote different vorticity production terms: red solid line: strain, blue dotted line: dilution, orange dash-dotted line: baroclinic, thick black solid line: sum of all accelerations

8. Summary and Conclusion

The aim of the current work is a numerical study of Combustion Induced Vortex Breakdown (CIVB) in an unconfined, straight, turbulent vortex.

In the first part, the available numerical combustion models have been assessed. A presumed-PDF combustion model based on ILDM chemistry has been implemented in the open source PDE framework OpenFOAM. It was tested on five different test cases along with two other combustion models, that were available. The results have been compared and the presumed-PDF model showed the best accuracy in most cases.

In the second part, the CIVB was investigated. The vortex was formed by a swirling jet of premixed methane/air and ejected into the ambient surrounding air by a movable block swirl generation device. The vortex was steady, unconfined, fully turbulent and had a strong inner axial velocity. The jet was ignited by an electrical spark and the flame propagation speeds have been measured using high speed video films.

At first, the experimental observations were reviewed and the occurrence of flame flashback were substantiated and the conditions for its appearance have been characterized. The isothermal flow has been measured by the PIV method and it was shown that no recirculation zones are present in the flow. This indicates that the negative velocities within the jet causing the flame flashback are determined by combustion process rather than by hydrodynamic isothermal effects related to the swirling jet destroy.

The phenomenon was simulated numerically for three selected cases using LES. Detailed analysis shows that Combustion Induced Vortex Breakdown causes the flame flashbacks. It is thus an important result of this work that the presence of the CIVB phenomenon was confirmed for the case of fully turbulent free straight vortex with an inner axial flow. At least for the higher swirl cases, it was also shown that widening of the stream surfaces caused by the deflection of the flow by the flame causes a back flow region around the flame tip that sucks the reaction zone upstream.

Bibliography

- [1] Hydrodynamics laboratory, ecole polytechnique. http://www.ladhyx.polytechnique.fr/activities/rapportx1998_en.html.
- [2] D. E. Abbott and S. J. Kline. Experimental investigations of subsonic turbulent flow over single and double backward-facing steps. *ASME Journal of Basic Engineering*, 84:317–325, 1962.
- [3] K. C. Altimira. *Numerical Simulation of Non-premixed Laminar and Turbulent Flames by means of Flamelet Modelling Approaches*. PhD thesis, Universitat Politècnica de Catalunya, 2005.
- [4] W. T. Ashurst. Flame propagation along a vortex: the baroclinic push. *Combustion Science and Technology*, 112:175–185, 1996.
- [5] M. Besson, P. Bruel, J. L. Champion, and B. Deshaies. Inert and combusting flows developing over a plane symmetric expansion. In *37th AIAA Aerospace Sciences Meeting and Exhibit*, 1999.
- [6] M. Boger, D. Veynante, H. Boughanem, and A. Trouve. Direct numerical simulation analysis of flame surface density concept for large eddy simulation of turbulent premixed combustion. *Symposium (International) on Combustion*, 27(1):917–925, 1998.
- [7] G. L. Brown and J. M. Lopez. Axisymmetric vortex breakdown part 2. physical mechanisms. *Journal of Fluid Mechanics*, 221:553–576, 1990.
- [8] B. Burgeth. Numerical evaluation of integrals involving the β -PDF. *Proceedings in Applied Mathematics and Mechanics*, 1(1):466–467, 2002.
- [9] V. Bykov and U. Maas. Reduction of reacting flow models by the REDIM method. In *21st ICDEERS - July 23-27, 2007 - Poitiers*.

Bibliography

- [10] V. Bykov and U. Maas. The extension of the ILDM concept to reaction–diffusion manifolds. *Combustion Theory and Modelling*, 11(6):839–862, 2007.
- [11] A. Büki, T. Perger, T. Turányi, and U. Maas. Repro-modelling based generation of intrinsic low-dimensional manifolds. *Journal of Mathematical Chemistry*, 31(4):345–362, 2002.
- [12] M. Carley. Evaluation of biot-savart integrals on tetrahedral meshes. *SIAM Journal on Scientific Computing*, 2007.
- [13] N. Chakraborty and M. Klein. A priori direct numerical simulation assessment of algebraic flame surface density models for turbulent premixed flames in the context of large eddy simulation. *Physics of Fluids*, 20(8):085–108, 2008.
- [14] M. W. Chase. *NIST - JANAF Thermochemical Tables*. Journal of Physical and Chemical Reference Data, fourth edition, 1998.
- [15] Y.-C. Chen, N. Peters, G. A. Schneemann, N. Wruck, U. Renz, and M. S. Mansour. An experimental data set for turbulent premixed flames. <http://www.itv.rwth-aachen.de/index.php?id=84&L=0>,.
- [16] Y.-C. Chen, N. Peters, G. A. Schneemann, N. Wruck, U. Renz, and S. Mansour. The detailed flame structure of highly stretched turbulent premixed methane-air flames. *Combustion and Flame*, 107:223–244, 1996.
- [17] J. Chomiak. Dissipation fluctuations and the structure and propagation of turbulent flames in premixed gases at high reynolds numbers. In *Sixteenth Symposium (International) on Combustion*, 1977.
- [18] F. C. Christo, A. R. Masri, and E. M. Nebot. Artificial neural network implementation of chemistry with pdf simulation of H_2/CO_2 flames. *Combustion and Flame*, 106(4):406–427.
- [19] A. W. Cook and J. J. Riley. A subgrid model for equilibrium chemistry in turbulent flows. *Physics of Fluids*, 6(8):2868–2870, 1994.
- [20] P. Domingo and L. Vervisch. Dns of partially premixed flame propagating in a turbulent rotating flow. In *Proceedings of the Combustion Institute*, volume 31, pages 1657–1664, 2007.

Bibliography

- [21] P. Domingo, L. Vervisch, S. Payet, and R. Hauguel. DNS of a premixed turbulent v flame and LES of a ducted flame using a FSD-PDF subgrid scale closure with FPI-tabulated chemistry. *Combustion and Flame*, 143:566–586, 2005.
- [22] C. Dopazo. *Turbulent Reacting Flows*, chapter Recent developments in PDF methods, pages 375–474. Academic Press, 1994.
- [23] C. Duwig and C. Fureby. Large eddy simulation of unsteady lean stratified premixed combustion. *Combustion and Flame*, 151:85–103, 2007.
- [24] M. Frenklach, T. Bowman, G. Smith, and B. Gardiner. Homepage of GRI-MECH reaction mechanism. http://www.me.berkeley.edu/gri_mech.
- [25] J. Fritz. *Flammenrückschlag durch verbrennungsinduziertes Wirbelaufplatzen*. PhD thesis, Technical University of Munich, 2003.
- [26] J. Fritz, M. Kröner, and T. Sattelmayer. Flashback in a swirl burner with cylindrical premixing zone. *Journal of Engineering for Gas Turbines and Power*, 126(2):276–283, 2004.
- [27] M. Galassi, J. Davies, J. Theiler, B. Gough, G. Jungman, M. Booth, and F. Rossi. *GNU Scientific Library – Reference Manual*. The GSL Team, 2007.
- [28] A. R. Ganji and R. F. Sawyer. Experimental study of the flowfield of a two-dimensional premixed turbulent flame. *AIAA Journal*, 18:817, 1980.
- [29] F. Gao and E. E. O’Brien. A large eddy simulation scheme for turbulent reacting flows. *Physics of Fluids A*, 5:1282–1284, 1993.
- [30] P. Gerlinger. *Numerische Verbrennungssimulation*. Springer, 2005.
- [31] M. Germano, U. Piomelli, P. Moin, and W. H. Cabot. A dynamic subgrid-scale eddy viscosity model. *Physics of Fluids A: Fluid Dynamics*, 3(7):1760–1765, 1991.
- [32] O. Gicquel, N. Darabiha, and D. Thévenin. Laminar premixed hydrogen/air counterflow flame simulations using flame prolongation of ildm with differential diffusion. *Symposium (International) on Combustion*, 28:1901–1908, 2000.
- [33] S. S. Girimaji. Assumed β -pdf model for turbulent mixing: Validation and extension to multiple scalar mixing. *Combustion Science and Technology*, 78(4):177–196, 1991.
- [34] I. Glassmann. *Combustion*. Academic Press, third edition, 1996.

Bibliography

- [35] D. G. Goodwin. *Cantera Users Guide*. Division of Engineering and Applied Science, California Institute of Technology, Pasadena, CA, November 2001.
- [36] R. Günther. *Verbrennungen und Feuerungen*. Springer, 1984.
- [37] T. Hahn. Cuba – a library for multidimensional numerical integration. *Computer Physics Communications*, 168(2):78–95, 2005.
- [38] T. Hasegawa, S. Michikami, T. Nomura, D. Gotoh, and T. Sato. Flame development along a straight vortex. *Combustion and Flame*, 129:294–304, 2002.
- [39] T. Hasegawa and K. Nishikado. Effect of density ratio on flame propagation along a vortex tube. In *Twenty-Sixth Symposium (International) on Combustion*, pages 291–297, 1996.
- [40] E. Hawkes and R. Cant. A flame surface density approach to large-eddy simulation of premixed turbulent combustion. *Proceedings of the Combustion Institute*, 28:51–58, 2000.
- [41] M. Herrmann. *Numerical Simulation of Premixed Turbulent Combustion Based on a Level Set Flamelet Model*. PhD thesis, RWTH Aachen, 2001.
- [42] A. Hoffmann. *Modellierung Turbulenter Vormischverbrennung*. PhD thesis, Universität Karlsruhe, 2004.
- [43] S. Ishizuka, T. Murakami, T. Hamasaki, K. Koumura, and R. Hasegawa. Flame speed in combustible vortex rings. *Combustion and Flame*, 113:542–553, 1998.
- [44] F. A. Jaber and S. James. A dynamic similarity model for large eddy simulation of turbulent combustion. *Physics of Fluids*, 10(7):1775–1777, 1998.
- [45] C. Jiménez, F. Ducros, B. Cuenot, and B. Bédard. Subgrid scale variance and dissipation of a scalar field in large eddy simulations. *Physics of Fluids*, 13(6):1748–1754, 2001.
- [46] F. Juretic. *Error Analysis in Finite Volume CFD*. PhD thesis, Imperial College London, 2004.
- [47] F. Kiesewetter. *Modellierung des verbrennungsinduzierten Wirbelaufplatzens in Vormischbrennern*. PhD thesis, Technical University of Munich, 2005.

Bibliography

- [48] M. Konle, F. Kiesewetter, and T. Sattelmayer. Simultaneous high repetition rate PIV–LIF-measurements of CIVB driven flashback. *Experiments in Fluids*, 44:529–538, 2008.
- [49] N. Kornev and E. Hassel. Synthesis of homogeneous anisotropic divergence free turbulent fields with prescribed second-order statistics by vortex dipoles. *Physics of Fluids*, 19(5), 2007.
- [50] M. Kröner. *Einfluss lokaler Löschvorgänge auf den Flammenrückschlag durch verbrennungsinduziertes Wirbelaufplatzen*. PhD thesis, Technical University of Munich, 2003.
- [51] A. Kurenkov and M. Oberlack. Modelling turbulent premixed combustion using the level set approach for reynolds averaged models. *Flow, Turbulence and Combustion*, 74:387–407, 2005.
- [52] D. Lentint. Assessment of the stretched laminar flamelet approach for nonpremixed turbulent combustion. *Combustion Science and Technology*, 100:95–122, 1994.
- [53] W. Leuckel. Swirl intensities, swirl types and energy losses of different swirl generating devices. In *IFRF Ijmuiden, Doc Nr. G 02/a/16*.
- [54] T. Lim. <http://serve.me.nus.edu.sg/limtt>.
- [55] F. Liu, H. Guo, G. J. Smallwood, O. L. Gülder, and M. D. Matovic. A robust and accurate algorithm of the β -PDF integration and its application to turbulent methane-air diffusion combustion in a gas turbine combustor simulator. *International Journal of Thermal Sciences*, 41:763–772, 2002.
- [56] J. M. Lopez. Axisymmetric vortex breakdown part 1. confined swirling flow. *Journal of Fluid Mechanics*, 221:533–552, 1990.
- [57] U. Maas. Efficient calculation of intrinsic low-dimensional manifolds for the simplification of chemical kinetics. *Computing and Visualization in Science*, 1(2):69–81, 1998.
- [58] U. Maas and S. B. Pope. Simplifying chemical kinetics: Intrinsic low-dimensional manifolds in composition space. *Combustion and Flame*, 88:239–264, 1992.
- [59] P. D. McCormack, K. Scheller, G. Mueller, and R. Tisher. Flame propagation in a vortex core. *Combustion and Flame*, 19:297–303, 1972.

Bibliography

- [60] J. Nafe and U. Maas. A general algorithm for improving ILDMs. *Combustion Theory and Modelling*, 6(4):697–709, 2002.
- [61] A. Nauert, P. Petersson, M. Linne, and A. Dreizler. Experimental analysis of flashback in lean premixed swirling flames: conditions close to flashback. *Experiments in Fluids*, 43(1):89–100, 2007.
- [62] D. R. Noble, Q. Zhang, A. Shareef, J. Tootle, A. Meyers, and T. Lieuwen. Syngas mixture composition effects upon flashback and blowout. *Proceedings of ASME Turbo Expo, Barcelona, Spain*, 2006.
- [63] I. K. Nwagwe, H. G. Weller, G. R. Tabor, A. D. Gosman, M. Lawes, C. G. W. Sheppard, and R. Wooley. Measurements and large eddy simulations of turbulent premixed flame kernel growth. In *Proceedings of the Combustion Institute*, volume 28, pages 59–65. The Combustion Institute, 2000.
- [64] OpenCFD Limited. *OpenFOAM Programmers Guide*. <http://foam.sourceforge.net/doc/Guides-a4/ProgrammersGuide.pdf>.
- [65] OpenCFD Limited. *OpenFOAM User Guide*. <http://foam.sourceforge.net/doc/Guides-a4/UserGuide.pdf>.
- [66] N. Peters. *Turbulent Combustion*. Cambridge University Press, 2000.
- [67] C. Pierce. *Progress-variable approach for large-eddy simulation of turbulent combustion*. PhD thesis, Stanford University, June 2001.
- [68] H. Pitsch and L. Duchamp de Lageneste. Large-eddy simulation of premixed turbulent combustion using a level-set approach. In *Proceedings of the Combustion Institute*, volume 29, pages 2001–2008, 2002.
- [69] R. W. Pitz and J. W. Daily. Combustion in a turbulent mixing layer formed at a rearward-facing step. *AIAA Journal*, 21:1565, 1983.
- [70] T. Poinsot and D. Veynante. *Theoretical and Numerical Combustion*. R.T. Edwards, Inc., 2005.
- [71] S. Pope. PDF methods for turbulent reacting flows. *Progress in Energy and Combustion Science*, 19:119–192, 1985.

Bibliography

- [72] S. Pope. Computation of turbulent combustion: Progress and challenges. *Symposium (International) on Combustion*, 23:591–612, 1990.
- [73] S. Pope. Computationally efficient implementation of combustion chemistry using in situ adaptive tabulation. *Combustion Theory and Modelling*, 1:41–63, 1997.
- [74] S. Pope and U. Maas. Simplifying chemical kinetics: Trajectory-generated low-dimensional manifolds. Technical Report FDA 93–11, Cornell, 1993.
- [75] S. B. Pope. *Turbulent Flows*. Cambridge University Press, 2000.
- [76] P. Sagaut. *Large Eddy Simulation for Incompressible Flows*. Springer, 2006.
- [77] Y. Sakai and S. Ishizuka. The phenomenon of flame propagation in a rotating tube. In *Twenty-Sixth Symposium (International) on Combustion*, pages 847–853, 1996.
- [78] D. Schmidt. *Modellierung reaktiver Strömungen unter Verwendung automatisch reduzierter Reaktionsmechanismen*. PhD thesis, Ruprecht-Karls-Universität Heidelberg, 9.7.1996.
- [79] E. Tangermann and M. Pfitzner. Large-eddy simulation of combustion-induced vortex breakdown in an unconfined vortex. In *22nd ICDERS*, Minsk 2009.
- [80] A. Trouvé and T. Poinso. The evolution equation for the flame surface density in turbulent premixed combustion. *Journal of Fluid Mechanics*, 278:1–31, 1994.
- [81] T. Turányi. Parameterization of reaction mechanisms using orthonormal polynomials. *Computers & Chemistry*, 18(1):45–54, 1994.
- [82] A. Umemura and K. Tomita. Rapid flame propagation in a vortex tube in perspective of vortex breakdown phenomena. *Combustion and Flame*, 125:820–838, 2001.
- [83] J. van Oijen. *Flamelet-Generated Manifolds: Development and Application to Premixed Laminar Flames*. PhD thesis, Technical University Eindhoven, 2002.
- [84] J. A. van Oijen, F. A. Lammers, and L. P. H. de Goey. Modeling of complex premixed burner systems by using flamelet-generated manifolds. *Combustion And Flame*, 127:2124–2134, 2001.
- [85] J. Warnatz, U. Maas, and R. W. Dibble. *Combustion*. Springer, 2006.

Bibliography

- [86] H. Weller, G. Tabor, H. Jasak, and C. Fureby. A tensorial approach to computational continuum mechanics using object orientated techniques. *Computers in Physics*, 12(6):620 – 631, 1998.
- [87] H. G. Weller. The development of a new flame area combustion model using conditional averaging. Technical report, Imperial College of Science Technology and Medicine, 1993.
- [88] H. G. Weller, G. Tabor, A. D. Gosman, and C. Fureby. Application of a flame-wrinkling LES combustion model to a turbulent mixing layer. In *Twenty-Seventh Symposium (International) on Combustion*, pages 899–907. The Combustion Institute, 1998.
- [89] D. Wendig, E. Hassel, and N. Kornev. Untersuchungen an einem Verbrennungsprüfstand mit hilfe der PIV-Messtechnik. In *Lasermethoden in der Strömungsmesstechnik*, 2006.
- [90] D. Wendig, E. Hassel, and N. Kornev. Untersuchungen zum Flammrückschlag in drallerzeugenden Vormischbrennern. In *Lasermethoden in der Strömungsmesstechnik*, 2007.
- [91] F. A. Williams et al. Homepage of San Diego reaction mechanism, University of California, San Diego. <http://maeweb.ucsd.edu/~combustion/cermech>.
- [92] S. Yun, M. F. Lightstone, and M. J. Thomson. An evaluation of beta PDF integration using the density-weighted PDF and the un-weighted PDF. *International Journal of Thermal Sciences*, 44:421–428, 2005.

Selbständigkeitserklärung

Hiermit versichere ich, die vorliegende Dissertation eigenständig und ausschließlich unter Verwendung der angegebenen Hilfsmittel, angefertigt zu haben. Alle öffentlichen Quellen sind als solche kenntlich gemacht. Die vorliegende Arbeit ist in dieser oder anderer Form zuvor nicht als Prüfungsarbeit zur Begutachtung vorgelegt worden.

Rostock,

Hannes Kröger

Wissenschaftlicher Lebenslauf

Dipl.-Ing. Hannes Kröger
geb. 28.08.1979 in Rostock

- 1999-2001 Studium Maschinenbau
an der Universität Rostock (Vordiplom)
- 2001-2005 Studium Verkehrswesen
(Vertiefungsrichtung Luft- und Raumfahrttechnik)
an der Technischen Universität Berlin
- 2004 Studienarbeit
Thema "Anpassung von Materialparametern mittels der
Evolutionstrategie und verschiedenen FEM-Analysen
für eine Nickelbasislegierung bei hohen Dehnraten"
- 2005 Diplomarbeit
Thema "Implementierung und Validierung von
wirbelbasierenden und dynamischen gemischten
Feinstrukturmodellen für die Large-Eddy-Simulation"
- 2005-2008 Wissenschaftlicher Mitarbeiter
am Lehrstuhl für Technische Thermodynamik
Mitarbeit am DFG-Projekt
"Flammenbeschleunigung in Wirbelröhren
durch Verbrennungsinduziertes Wirbelaufplatzen"

Rostock,

Hannes Kröger